UNIVERSITÀ DEGLI STUDI DI MILANO-BICOCCA
Facoltà di Scienze Matematiche, Fisiche e Naturali
Ph.D. School in Material Science
XXIV cycle

Theoretical models of heterogeneous catalysts based on cerium oxide

Ph.D Thesis of
Gloria PREDA
056904
Thesis presented for the degree of Doctor Europeaus

Supervisor: Prof. Gianfranco PACCHIONI
Coordinator: Prof. Gian Paolo BRIVIO

January 2012

Contents

Chapter I

Introduction

1.1 Cerium oxide

Ceria, in many cases in combination with other oxides, with supported metals, or with dopants, is one of the most important industrial and environmental catalysts. It is considered a prototype of reducible oxides, because it can very easily loose and adsorb oxygen, a property which is at the basis of its usage in many catalytic reactions. Thus, it is attracting an increasing interest also from a fundamental point of view. In fact, the nature of reduced CeO_2 and of oxygen vacancies in the bulk or on the surface have been subject to several studies.

Cerium dioxide exhibits a fluorite type structure, with a face-centred cubic unit cell (f.c.c.) with space group F*m3m*, (a = 0.541 nm),[1] and a band gap of almost 6 eV. In this structure, each cerium cation is surrounded by eight equivalent nearest-neighbor oxygens at the corners of a cube. Each anions is tetrahedrally coordinated by four Ce^{4+} (Figure 1.1).

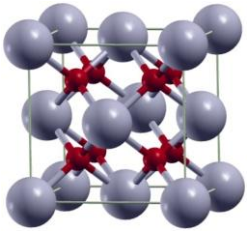

Figure 1.1: Ceria bulk 1x1

This structure can be actually imagined as a *ccp* array of cerium cations with oxygens occupying all the tetrahedral holes.[1]

1.2 Synthesis

Processes like synthesis and preparation affects some properties of ceria-based materials such as particle size, formed phase, surface area, catalytic activity and oxygen storage capacity. Therefore, many studies are available in literature about synthesis, preparation and modification, aiming to develop ceria-based materials with high catalytic activity, oxygen storage capacity, and thermal durability.[1]
Several techniques are available in order to obtain ceria-based materials:[1]

- Solid to solid synthesis: ceramic methods are convenient to obtain solid materials, in particular polycrystalline powders.[1] Mechanical milling is also a simple and effective method to have powders with small crystallite size (few nanometers) and a high concentration of lattice defects. The presence of structural defects in the mixed oxides increases the oxygen storage capacity.[2,3,4,5,6]
- Liquid to solid synthesis: they are useful to obtain solid compounds that contain the different cations in an ideal atomic dispersion. Several techniques are available to synthesize different products. Precursor methos are used to obtain for example nanosize or porous ceria particle by low-temperature pyrolysis of amorphous citrate.[7] Precipitation and co-precipitation methods are used to prepare crystalline or amorphous ceria-based fine particles; ceria preparation is

carried out by calcinations of the hydroxide or oxalate gel precipitated using the reaction of aqueous solution of inorganic cerium salts or oxalic acid.[8,9,10] Hydrothermal and solvothermal synthesis are useful to obtain single crystals or fine powders with nanosized to submicron particles.[11] Sol-gel method, an important technique suited for the synthesis and preparation of ultrafine oxide materials, allows the preparation of particles of CeO_2[12] or ceria solid solutions. Surfactant-assisted method is used to obtain mesoporous ceria and ceria-zirconia powders.[1] Emulsion and micro-emulsion method are suitable methods to prepare size-controlled and morphology-controlled fine particles, ceria and ceria-zirconia mixed oxides can be synthesized like this.[13,14,15] Modified flux method has been used to prepare fine particles of $Ce_{1-x}Pr_xO_2$ solid solutions.[16] With electrochemical methods nanocrystalline cerium (IV) oxide powders with an average particle size of 10-14 nm have been obtained.[17,18] Spray pyrolysis allows the synthesis of well-crystallized ceria nanoparticles at low temperature.[19] Finally, impregnation method has been used to prepare ceria powders doped with various cations and ceria-based oxides deposited on other oxides such as silica and alumina.[20,21,22]

- Gas to solid synthesis: gas-condensation or sputtering are very useful to prepare thin films or nanostructured ceria particles[23], while the chemical vapour deposition (CVD) method is usually used to obtained a thin film material, but nanostructured ceria particles and ceria-yttria have also been synthesized by some arrangements of the apparatus[24].

1.3 Ceria in Diesel particulate soot abatement

An aspect which has been investigated in detailed studies is the role of transition metal particles on the activity of CeO_2 in oxidation processes, water-gas shift, soot combustion in Diesel antiparticulate filters, etc.[25,26].

In particular with this respect, ceria-based catalysts are receiving an increasing interest due to their unique properties for application in automotive car exhausts treatment. Three-way catalysts (TWC) used in gasoline-powered engines are designed to eliminate hydrocarbons, CO, and NO_x. Most of TWC formulations combine CeO_2-based materials with nanoparticles of noble metals. However, during the last years, diesel-powered engines have greatly increased their diffusion, in fact nowadays about 60% of all commercial vans use diesel engines, and the abatement of the exhausts poses a series of problems to meet legislation requirements[27]. The most used technology to reduce them is based on filtering systems consisting of a trap that collects the particulate (Figure 1.2), which is mainly made up of carbon soot.

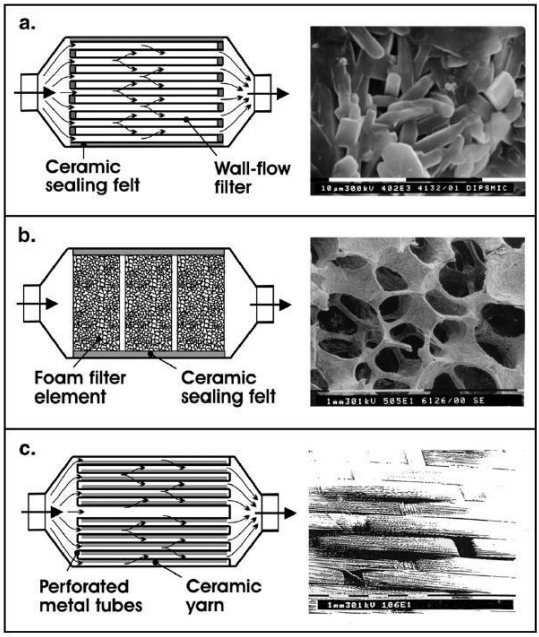

Figure 1.2: Sketch and SEM pictures of the major trap types.[27]

Once the particulate has been collected, it must be burnt off in order to regenerate the filter, that is usually a ceramic wall-flow monolith. Diesel particulate spontaneously burns in air at temperatures of about 500-600 °C, temperatures that are not reached in typical diesel vehicles. If an excess of soot is collected on the filter, the gas exhaust can not diffuse and pressure and temperature can increase considerably, eventually resulting in the melting of the filter. Thus, a key technological issue is reducing the combustion temperature of the soot. Usually, one of the methods adopted is the use of a ceria-based catalyst added as a filter coating, since several reports show that ceria-based oxides have excellent activity for soot oxidation also at relatively low temperatures[27].

Two effects play a very important role in the formulation of the catalyst. The first is the intensity of the contact between carbon soot and catalyst. In principle, it is possible to have a “loose” or a “tight” contact (Figure 1.3), where the last one leads to much better performances[28,29].

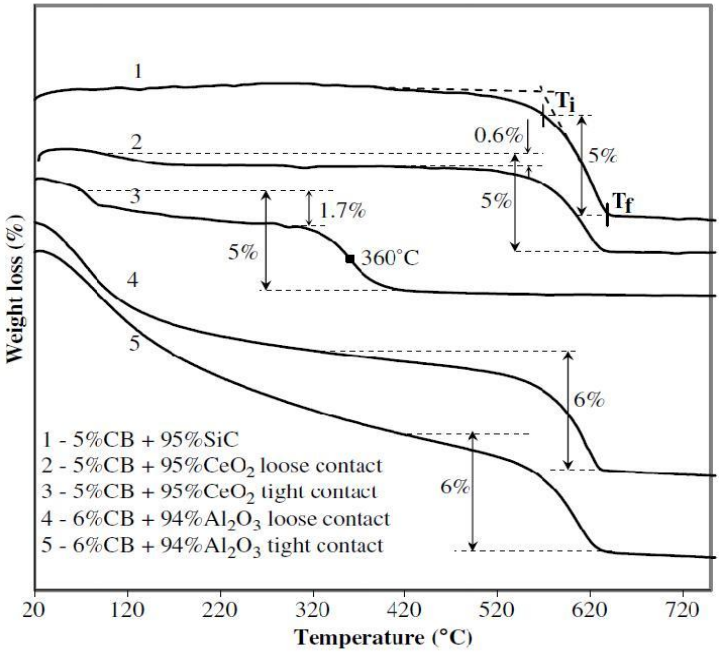

Figure 1.3: TG curves of carbon black combustion in the presence of Al_2O_3 and CeO_2.[28]

The level of contact is thus an essential parameter to evaluate the efficiency of a modified catalyst in soot combustion. The second aspect is that several studies show better performances of the catalyst when ceria is mixed with other oxides or doped with transition metal or lanthanide atoms (Figure 1.4).[30,31,32,33,34,35]

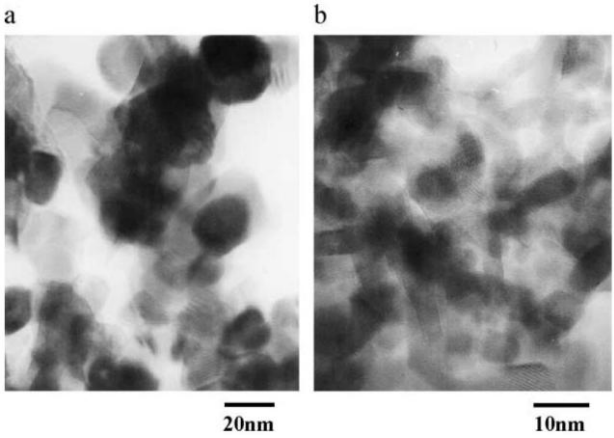

Figure 1.4: TEM images of $Sm_{0.2}Ce_{0.8}O_{1.9}$ primary particles of (a) nanosize round shape particles and (b) nanosize elongated particles.[36]

The role of these dopants can be of different type. For example, it has been suggested that La^{3+} ions are able to stabilize ceria particles with larger surface area and to raise the sintering temperature of the particles[33]. Since ceria is an oxygen storage catalyst, it is also possible that these dopants increase the mobility of oxygen species, or make the redox mechanisms associated to the oxygen release/adsorption easier (Figure 1.5).[37]

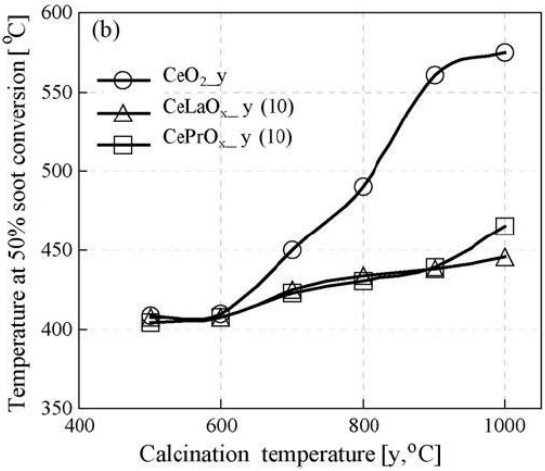

Figure 1.5: Temperature (Tx%) at 'x%' soot conversion over catalysts prepared by different calcination temperatures.[33]

Considering the mechanism, it is generally assumed that the soot oxidation proceeds via the Mars-van Krevelen one,[38] where the carbon particles are oxidized by oxygens coming from the lattice, with subsequent formation of oxygen vacancies and consequent reduction of CeO_2 (Ce^{4+}) to CeO_{2-x} (Ce^{3+}) (Figure 1.6).[31,32]

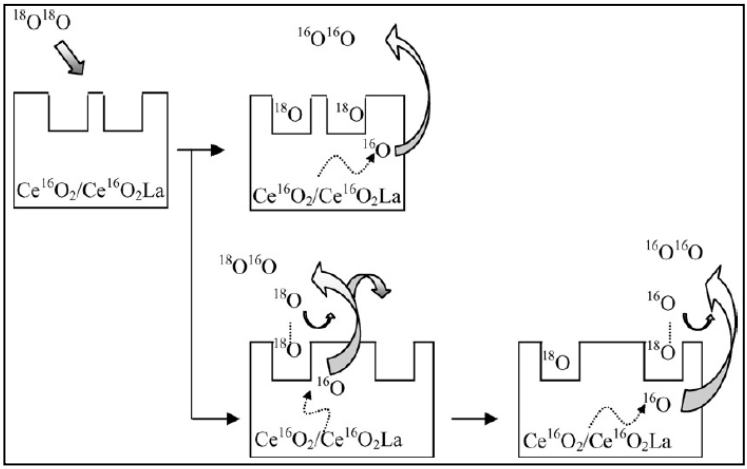

Figure 1.6: Interaction of $^{18}O^{18}O$ with CeO_2 and CeO_2La.[32]

Soot oxidation experiments performed in the presence of $^{18}O_2$ have shown that the gas-phase labeled oxygen replaces lattice oxygen creating new highly active nonlabelled oxygen species[32]. In this process, the role of a transition metal, like for example Pt, is probably facilitating the dissociation of the oxygen molecules that come from the gas-phase. This lowers the energy demand for a crucial step in the whole catalytic cycle.

1.4 Peroxo and superoxo formation

From what has just been said, one can state that a detailed microscopic view of the mechanism of the oxidative process is still missing. However, some achievements have been established in literature, such as the formation of paramagnetic O_2^- superoxo species shown by EPR[30,39,40] (Figure 1.7) or the detection of diamagnetic O_2^{2-} peroxo species by Raman spectroscopy (Figure

1.8),[41,42,43,44] that appear when reduced CeO_{2-x} samples are exposed to oxygen.

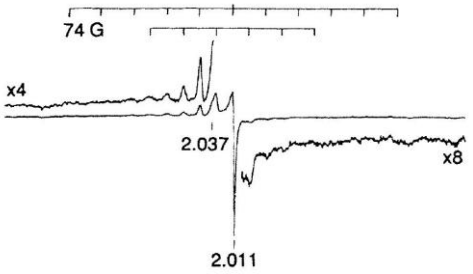

Figure 1.7: EPR spectrum of CeO_2 outgassed at 473 K and with ^{17}O-enriched O_2 subsequently adsorbed at 298 K[39]

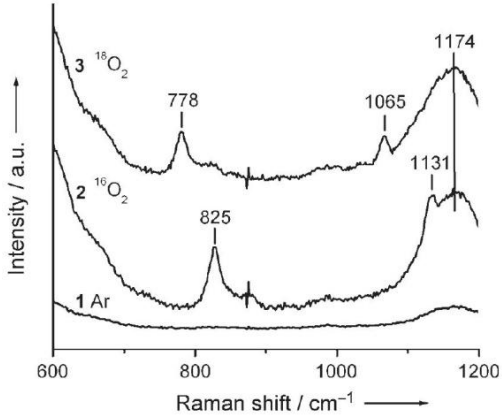

Figure 1.8: Typical RAMAN spectra of CeO_2 sample treated with H_2 before 298 K exposure to 1) Ar, 2) 10% $^{16}O_2$, and 3) 10% $^{18}O_2$ atmosphere.[43]

It has been suggested that these are the precursor surface species which start the soot oxidation. Nevertheless, other mechanisms, like

the involvement of lattice oxygen or of oxygen species which form directly at the soot/catalyst interface[37] have been proposed. Then, investigating how can this species form becomes necessary. An oxygen vacancy is associated with the formation of two Ce^{3+} $(4f)^1$ ions and so it could behave as a two-electron donor center. The O_2 molecule interacts strongly with the O vacancy, where the molecule is adsorbed with one O atom filling the vacancy and the other pointing out from the surface (see Sec. 5.3.2).[45] So, O_2 adsorption at an oxygen vacancy removes the defect resulting in the formation of a surface peroxo group O_2^{2-}, that is diamagnetic and can be detected by IR or Raman spectroscopy. In fact typical bands in the 830-870 cm^{-1} region arise when peroxo groups are present.[41,43] This reaction mechanism has been proven theoretically in a number of studies.[43,45,46] As said before, superoxo O_2^- species have also been reported as the result of interaction of molecular oxygen with reduced ceria samples. Here the fingerprint of the formation of the superoxo species are the characteristic EPR signal,[39] and a typical Raman band around 1130 cm^{-1}.[41,43] However, it has been proven that O_2^- species do not form by interaction with a two electron donor such as the O vacancy, so another sort of interaction must be present. In a recent study, Conesa has shown that superoxo O_2^- species form when O_2 interacts directly with a "single electron" oxygen vacancy.[47] In this model however a tetravalent Ce^{4+} ion has been replaced by a trivalent La^{3+} ion, thus leaving only one Ce^{3+} cation associated to an O vacancy. In this case only one electron can be transferred to the adsorbed oxygen molecule, and just a superoxo, and not a peroxo, can be generated. A thing that is not clear is how "single electron" oxygen vacancies can be formed on a real ceria surface. A possibility is that, due to the electron mobility, in some cases just one electron remains in the proximity of the vacancy so that only a single electron transfer can occur. This hypothesis

however contrasts with another observation. If electron mobility is high, O_2^- species should in principle form by O_2 adsorption on regular sites of a reduced CeO_{2-x} surface followed by an electron transfer from one electron in a Ce^{3+} $4f^1$ state to the π_g* MOs of the adsorbed oxygen molecule. This is indeed the typical process occurring on other reduced oxides like TiO_2 where O_2 adsorbed on the non-defective surface acts as an electron scavenger which traps electrons from the reduced Ti^{3+} ions of the bulk.[48,49] Nevertheless, according to our DFT calculations (see Sec. 5.3.2) this process does not occur on reduced CeO_2 probably because in ceria the 4f levels are deeper in energy then the O_2 π_g* levels.

A possibility not considered before in theoretical models is that O_2^- species could form by direct interaction of O_2 with low-coordinated Ce^{3+} ions (edges, steps, dislocations, etc.). Recent studies have shown that Ce^{3+} cations can be more easily found at low coordinated sites of CeO_{2-x} reduced particles[50,51] and that Ce^{3+} ions form also on stoichiometric stepped surfaces where also in this case they tend to occupy the less coordinated sites.[52] So, in this case the process of interest is the reaction $Ce^{3+}{}_{LC} + O_2 \rightarrow Ce^{4+}{}_{LC} + O_2^-$, where LC is the low-coordinated site. In this model O vacancies are not directly involved, but just exposed Ce cations.

The role of these undercoordinated sites in promoting the activation of molecular oxygen by formation of superoxo radicals has been studied in this Ph.D. thesis (see Chapter 6). By means of DFT calculations on small and nanometer size ceria nanoparticles it has been shown that superoxo species actually form by interaction of O_2 with exposed Ce cations. Despite the large number of theoretical studies dedicated to CeO_2, CeO_{2-x}, and Ce_2O_3 surfaces in recent years[51,52,53,54,55,56,57] this problem has not been explicitly studied before. For example, Huang and Fabris[45] have considered the properties of an O_2^- radical adsorbed above a Ce^{4+} ion but one

extra electron was added to the system leaving the origin of the formation of superoxo species unanswered, Choi et al.[43] have found that a special conformation of O_2^- can exist when O_2 is adsorbed on an O vacancy but this structure is about 3 eV less stable than the peroxo species, showing that this is the only structure which forms in these conditions.

1.5 Ag/CeO_2 interfaces

Considering the possible role of transition metals with this respect, we studied the behavior of silver, amongst all, in activating oxygen molecules and reducing ceria. In fact in literature is known that the addition of Ag to nanocrystalline CeO_2 leads to an efficient catalyst for CO and hydrocarbon oxidation[58]; Machida et al.[59] have reported that loading the ceria catalyst with Ag metal leads to an improved catalytic activity and a lower temperature in soot combustion (Figure 1.9).

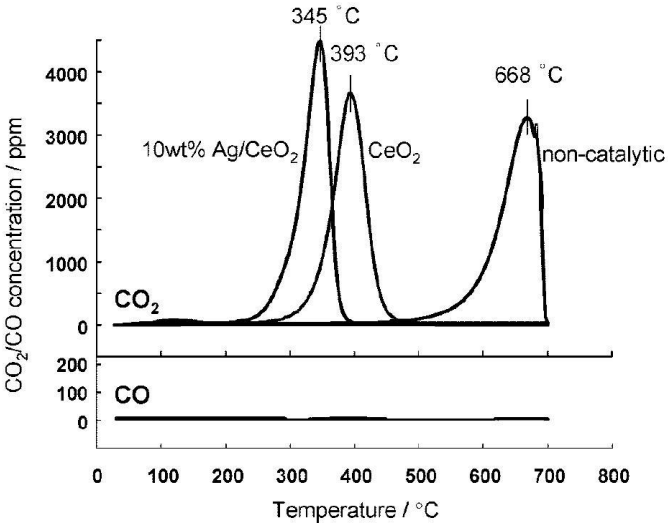

Figure 1.9: Effect of Ag loading on soot combustion profiles of CeO_2. Soot/CeO_2 tight-contact mixtures with weight ratio of 1/20.

In their experiments, CeO_2 has been mixed with various amounts of Ag, from a few percent to about 20% in weight. The combustion temperature is thus reduced from about 390 °C to about 340 °C for 10% Ag content. This better performance has been tentatively explained stating that metallic silver can promote the formation of superoxo species[60,61]. In fact, the EPR signal associated to this species increases slightly when metallic silver is added to ceria. In another study Aneggi et al.[62] have shown that Ag/CeO_2 samples, obtained by impregnation of CeO_2 with an aqueous solution of $AgNO_3$ followed by calcinations, contain Ag crystallites separated from the ceria particles by an Ag_2O phase (Figure 1.10).

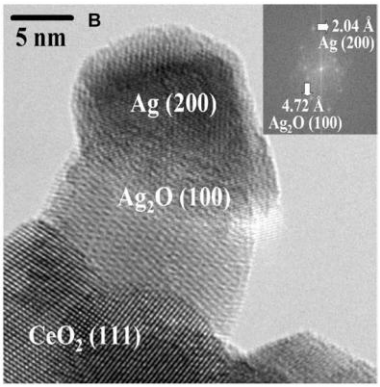

Figure 1.10: Formation of metallic Ag separated by Ag_2O from CeO_2 (TEM).

Other authors have reported that ceria is able to keep silver in a positive oxidation state[63]. Moreover, the possible role of silver-ceria boundaries in solid oxides fuel cells has been theoretically studied in details by Wang et al.[64]. From a more fundamental side, Ag adsorption on CeO_2 well defined surfaces has been studied with sophisticated surface science techniques[65,66,67]. In this Ph.D. thesis we modeled Ag atoms, Ag_5 and Ag_{10} clusters adsorbed on CeO_2(111) regular and defective surfaces in order to investigate the redox effects on the system due to this interaction (see Chapter 7). Subsequently, we also considered silver mono and bi-layers on the same CeO_2(111) surfaces, to see if the same effects are still present for extended silver coverages (see Chapter 7). From our results we found that the situation is very complex, but a clear tendence of reducing ceria by silver is present, both in the case of adsorbed nanoparticles and bigger coveraging structures. In this work we also made oxygen molecule interact with Ag atoms and Ag_5 clusters adsorbed on ceria to investigate whether they are more easily activated by the presence of the metal (see Chapter 5). Our

calculations resulted either in non-activation of the oxygen, or in formation of a peroxo species, depending on the different position of the O_2 with respect to the silver atom or nanoparticle and the ceria surface.

1.6 Theoretical treatment of CeO_2

From a technical point of view, the theoretical treatment of reduced CeO_2 presents several problems and difficulties. These methodological problems are added to the intrinsic complexity of the function of the catalyst, thus making the entire problem extremely challenging from a theoretical point of view. One of the problems connected to the use of electronic structure methods for the description of reduced ceria is that standard density functional theory (DFT) (see Sec. 2.3) fails in describing the localized nature of the Ce 4f states[54,68,69]. This can be partly removed by using hybrid functionals[55,70] or the so called DFT+U approach (see Sec. 2.4).[43,68,71] Other problems in the treatment of CeO_2 arise from the fact that the change in oxidation state of the Ce ion from +4 to +3 results in a change of lattice parameter which is not treated exactly at all levels of theory.[72] Recently, it has been suggested that the DFT approach in the local density approximation (LDA) (see Sec. 2.3) is better suited to describe the geometrical structure of the material, while the more advanced generalized gradient approximation (GGA) (see Sec. 2.3) should be used in order to obtain more reliable energy differences[72]. A combined use of LDA for geometry and GGA for energy has thus been proposed,[72] and is adopted here.

1.7 Model system: MgO surfaces

In this work, beside the study of the catalytic activity of functionalized ceria surfaces, we modeled the regular and defective surfaces and the low-coordinated sites of MgO with embedded cluster model calculations (see Sec. 2.5). This was done in order to study a system simpler than ceria, that could act as a model for metal adsorption, reduction of adsorbates and formation of superoxo species (see Chapter 4). In fact, comparing theoretical results with experimental ones is much easier for MgO surfaces, because experimental data are often clearer and more abundant, and the theoretical model used to evaluate the observable properties of interest can thus be validated. Beyond this, studying both a reducible and a non-reducible oxide allows to have a wider view of the problem and to go further into the understanding. However, MgO is not taken just as a model, but it shows very interesting catalytic properties (See Part I).[73,74]

Magnesium oxide is a basic, ionic and isolating oxide with an energy gap of about 7.6 eV.[75] It crystallizes in a cubic face-centred lattice (fcc) where the distance between two nearest-neighbors is 2.104 Å. Thanks to its simple structure and the low atomic weight of its components, it has attracted great interest both in surface chemistry and in computational chemistry. Moreover, Mg^{2+} and O^{2-} carry just *s* and *p* electrons. This make the ab-initio theoretical study much simpler than in the case of transition metals.

Experimentally, magnesium oxide can be obtained as single crystals and thin films or powders.[76,77] A MgO single crystal cut in ultra high vacuum (UHV) conditions generates a 001 surface with a very low amount of defects. A technique to produce ultra-thin films involves the deposition of Mg vapours in UHV on a metal substrate in presence of a moderate O_2 partial pressure. The better metal

surfaces are molybdenum and silver, because they show the same symmetry and a lattice parameter similar to the one of magnesium oxide. These characteristics let the oxide grow in an epitaxial way.
MgO powders are made up of cubic microcrystals with an edge length between 30 nm and 1 μm.[78] They are produced by direct combustion of Mg in air and they are characterized by a high crystallographic perfection. The facets of the microcrystals are well defined and expose the 100, 010 and 001 cristallographic planes. When MgO is produced with this technique, it is usually called smoke, and the specific surface area of the sample is about some m^2g^{-1} (Figure 1.11).

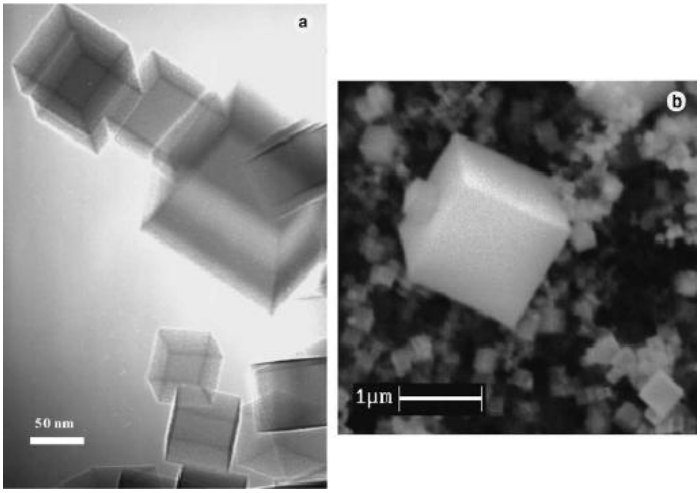

Figure 1.11: Images obtained with HRTEM (a) and SEM (b) of smoke MgO cubic crystals showing a high regularity. Samples obtained by Mg combustion.[78]

Several techniques can be used in order to obtain samples with higher surface area (200-500 m^2g^{-1}), such as:

- $Mg(OH)_2$ decomposition (Figures 1.12 and 1.13) in vacuum at 530 K.[79] This technique generates layers of compenetrated cubes with nanometric dimensions, that show the presence of many morphological defects, such as edges, corners and reverse corners[78,80,81,82] thanks to the tiny dimensions and the vicinity of the cubes.
- With sol-gel techniques, gel hydroxides are obtained from metoxides. These hydroxides are then dehydrated under vacuum.[80] Using this method samples with a very high surface area can be produced.
- Chemical vapour deposition[81] allows the formation of films or nanoparticles with a very high level of purity and controlled morphology.[83]

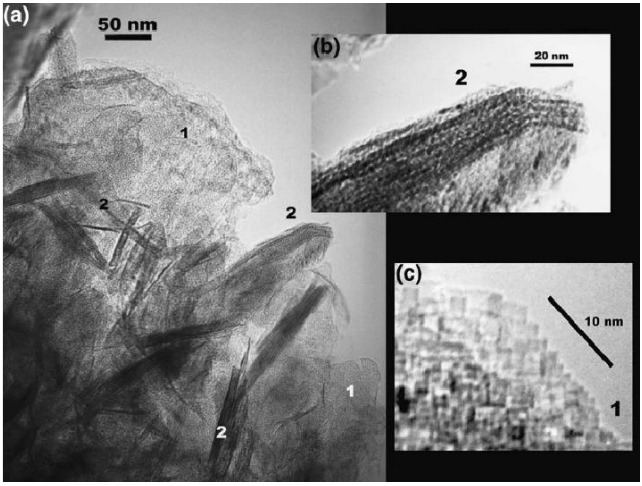

Figure 1.12: Images obtained with TEM of $Mg(OH)_2$. In (a) it is possible to see the structure with perpendicular and parallel orientation with respect to the electronic beam. In (b) the structure is visible. The layers are due to the partial decomposition in MgO and H_2O. In (c) the formation of compenetrated cubes is detected.[77]

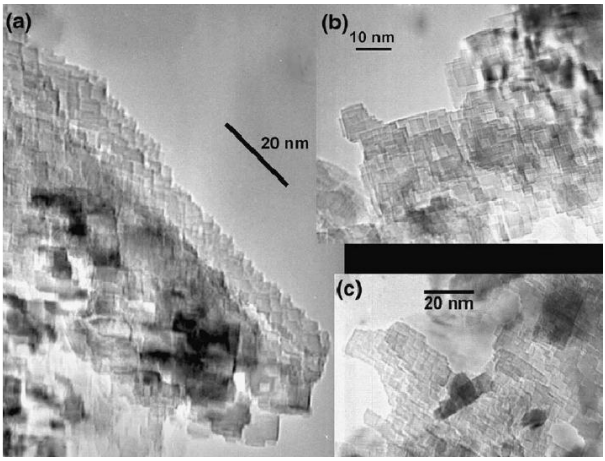

Figure 1.13: Images obtained with TEM of MgO prepared by decomposition of $Mg(OH)_2$ activated by staying two hours under vacuum at 1073 K. The edges of the compenetrated cubes is enhanced after thermal treatment. They can reach about 10 nm.[77]

Many properties of inorganic materials and surfaces are controlled not just by geometric and electronic factors, but also by structural defects.[78,84] In chemistry the importance of defects is due to the evidence that they considerably determine phenomena like corrosion and catalysis for some oxides.

Considering MgO, enough defects can completely modify the chemical behavior of the surface, for example towards the adsorption of metal clusters or of CO.[85] Indeed, the adsorption properties of CO[77,79,86] can be used to understand the reactivity of the important class of defect called undercoordinated defects (Figure 1.14)

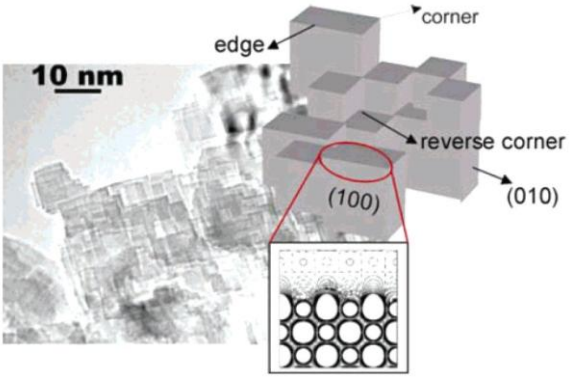

Figure 1.14: High-resolution transmission electron microscopy (HR-TEM) micrography of a high-surface-area polycrystalline MgO sample. The shape of the compenetrated cubes of the crystals is linked to the presence of defects, such as edges, steps, corners and reverse corners. In the inset, the electrostatic potential in the xy plane through the edge is shown.[87]

The MgO(100) surface, that shows just pentacoordinated ions, is not reactive towards carbon monoxide, that is very weakly bound to the cationic sites. In fact, with a binding energy of 0.13 eV,[85,88,89] it is bound just at very low temperatures. On MgO ultra-thin films,[90,91] CO is bound on undercoordinated Mg^{2+} cations on corner or edge sites with binding energies of 0.2-0.4 eV,[92,93] and a direct correlation between the bond strength of CO-Mg and the vibrational stretching frequency of the C-O bond, that is shifted towards higher values because of the field-dipole interaction is observed.[94,95,96] In fact superficial undercoordinated anions of MgO shows a highly basic behavior,[97] due to a decrease of the Madelung potential (U_{Mad}) in exposed sites of an ionic surface.[98] The O^{2-} anion is unstable in gas phase, dissociating in $O^{-} + e^{-}$, but in ionic oxides exists because it is stabilized by U_{Mad}. The Madelung potential decreases when the coordination number decreases, so it is maximum for the exacoordinated sites of the bulk materials and

minimum for the tricoordinated corner sites of the surface. A descreased value of the Madelung potential enhances the energy of the full 2p levels of O^{2-}, thus increasing its basic character.[98] In fact, this destabilization enhances the tendency to donate electrons of the site towards species that can accept electron density.

In conclusion, the very complex reactivity of the oxygen anions belonging to different sites on MgO surface is a clear example of the importance of morphology in determining the properties of oxide surfaces. Thus, it is possible to state that when the reactivity of an oxide is described, specifying the shape (single crystal, polycrystalline, amorphous, thin film, etc.) and morphology is necessary.

1.8 Activation of CO_2 and O_2 on alkali metals precovered MgO surfaces

The interaction of alkali metal atoms such as Na and K with the surface of insulating oxides[99,100,101] and their subsequent reactivity towards gas-phase molecules[102] is very interesting because these systems represent well defined models of activation of adsorbed molecules by effect of an electron transfer. In this context, the study of these systems is a good model that can provide useful information when the reactivity of O_2 on ceria and Ag precovered ceria surfaces is considered. In particular, the calculated EPR (Electron Paramagnetic Resonance) properties regarding the O_2^- species formed at Na/MgO surfaces can be compared with very well resolved experimental results (see Chapter 4). This comparison is very useful in order to validate the theoretical approach used to compute the properties of superoxide formed at ceria surfaces. In this

case, in fact, the experimental EPR results available in literature[39] are not well resolved.

Alkali metal atoms can be stabilized at the surface of alkaline earth metal oxides, such as MgO, as isolated atoms. These atoms are bound to morphological defects, in particular cationic edges, reverse edges, reverse corners, etc. (see Sec. 1.7) and their valence electron is strongly polarized by the interaction with the substrate.[99] This bonding mechanism implies that no charge transfer occurs from the metal to the surface, and the alkali atoms remain essentially neutral.[101] Still, the interaction with the surface considerably lowers the ionization potential of the deposited alkali atoms compared to the free atoms, an effect which is expected to favour the electron transfer to adsorbed molecular species. Such an electron transfer occurs in the case of K atoms deposited on MgO towards the CO_2 molecule leading to surface stabilized CO_2^- radical anions, see Chapter 3.[102]

CO_2 activation, in fact, is an essential step in the use of this molecule in carbon chemistry. Due to the high stability of the molecule, only the interaction with solid supports or transition metal ions leads to activated forms of CO_2 which can then evolve in other carbon-based compounds.[103] Examples of activation of CO_2 have been reported as a consequence of the coordination of the molecule to transition metal complexes[104] or by interaction with solid surfaces.[105,106,107] One of the possible steps in the activation of the molecule is the formation of CO_2^- radical anions. Since in CO_2^- one electron is added to the antibonding π orbitals of CO_2, the molecule bends and the C-O bond is elongated. In this respect, the study of systems where stable CO_2^- radicals are formed are of both practical and theoretical interest.

Formation of CO_2^- has been reported under special conditions. When a Ne:CO_2 sample was codeposited at approximately 5 K with a beam

of neon atoms that had been excited in a microwave discharge, formation of the CO_2^- radical anion has been observed and a corresponding IR frequency at 1658 cm^{-1} has been assigned to CO_2^-.[108] CO_2^- was observed with electron paramagnetic resonance (EPR) in alkali halides by γ-irradiation of sodium formate.[109] When CO_2 is condensed with alkali metal vapor $M^+CO_2^-$ complexes form, usually stabilized in a rare-gas matrix. In particular, experiments have been reported on Li-CO_2,[110,111] Na-CO_2,[112,113] and K-CO_2.[113,114] EPR measurements clearly show the occurrence of a charge transfer and the formation of $M^+CO_2^-$ complexes.

The other systems where CO_2 can form CO_2^- are oxide surfaces. In general, CO_2 reacts with the oxide anions (mainly at the low-coordinated sites) to form surface carbonates. However, in the presence of excess electrons, resulting for instance from the deposition of alkali metals on transition metal oxides like TiO_2 or Cr_2O_3, formation of stable CO_2^- species has been reported.[106,107,115,116,117] Recently, the nature of surface stabilized CO_2^- species has been observed on electron-rich MgO surfaces.[107] In this case, excess electrons are generated by interaction of MgO powders with H_2 followed by UV irradiation or directly by splitting of atomic hydrogen into protons and trapped electrons, forming $(H^+)(e^-)$ centers.[118,119,120,121,122] CO_2 interacts with these centers and forms stable CO_2^- complexes which have been fully characterized experimentally and theoretically.[107,123]

Beside the activation of CO_2, the activation of O_2 is more important in the context of this study. As said before, molecular oxygen, in addition to the usual $^3\Sigma_g^-$ paramagnetic ground state, exhibits a variety of activated forms, among which superoxide O_2^- and peroxide O_2^{2-} states are particularly relevant in a number of

phenomena including catalytic oxidation, for example of carbon soot, as well as biochemical processes.[124,125,126]

The chemistry of oxygen species at solid surfaces has attracted the attention of several research groups over the years due to its relevance in various fields of modern science such as heterogeneous catalysis, material science, electrochemistry and corrosion. The bonding of molecular oxygen to metal atoms involving the formation of O_2^- ions is thus particularly important as it represents the initial stage of the long trek which leads to the incorporation of oxygen into oxide lattices.

The superoxide anion has a $^2\Pi_g$ ground state and is readily detected by EPR spectroscopy when subjected to asymmetric electrostatic fields. In particular, the EPR technique has singularly advanced our understanding on the nature of the paramagnetic oxygen intermediates.[127,128] The surface adsorbed superoxide anion is usually identified on the basis of its g tensor, which is a very sensitive parameter of the electrostatic field of the adsorption site, however only few examples are present in the literature where the superhyperfine interaction with the adsorption site is detected.[128,129] In Chapter 4 we show by means of theoretical calculations and EPR experiments that Na^+/O_2^- complexes are formed at the surface of MgO by interaction of gas-phase O_2 with deposited Na atoms.

1.9 BIBLIOGRAPHY

[1] A. Trovarelli, *Catalysis by Ceria and Related Materials*, Imperial College Press (**2002**).
[2] F. Zamar, A. Trovarelli, C. de Leitenburg, G. Dolcetti, *Stud. Surf. Sci. Catal*., 101 (**1996**) 1283.
[3] C. de Leitenburg, A. Trovarelli, F. Zamar, S. Maschio, G. Dolcetti, J. Llorca, *J. Chem. Soc. Chem. Commun*. (**1995**) 2181.
[4] A. Trovarelli, F. Zamar, J. Llorca, C. de Leitenburg, G. Dolcetti, T. Kiss, *J. Catal*. 169 (**1997**) 490.
[5] A. Suda, T. Kandori, N. Terao, Y. Ukyo, H. Sobukawa, M. Sugiura, *J. Mater. Sci. Lett*. 17 (**1998**) 89.
[6] S. Enzo, F. Delogu, R. Frattini, A. Primavera, A. Trovarelli, *J. Mater. Res*. 15 (**2000**) 1538.
[7] B. R. Powell, R. L. Bloink, C. C. Eickel, *J. Am. Ceram. Soc*. 71 (**1988**) C104.
[8] C. de Leitenburg, A. Trovarelli, J. Kaspar, *J. Catal.* 166 (**1997**) 98.
[9] N. Audebrand, J.-P. Auffredic, D. Louer, *Chem. Mater*. 12 (**2000**) 1791.
[10] S. Nakane, T. Tachi, M. Yoshinaka, K. Hirota, O. Yamaguchi, *J. Am. Ceram. Soc.* 80 (**1999**) 3221.
[11] M. Yoshimura, S. Somiya, *Mater. Chem. Phys*. 61 (**1999**) 1.
[12] F. Imoto, T. Nanataki, S. Kaneko, *Ceram. Trans*. 1 (**1988**) 204.
[13] T. Masui, K. Fujiwara, K. Machida, G. Adachi, T. Sakata, H. Mori, *Chem. Mater*. 9 (**1997**) 2197.
[14] T. Masui, K. Fujiwara, Y. Peng, T. Sakata, K. Machida, H. Mori, G. Adachi, *J. Alloys Compds*. 269 (**1998**) 116.
[15] M. Fernándenz-García, A. Martínez-Aria, A. Iglesias-Jues, C. Belver, A. B. Hungrfa, J. C. Conesa, J. Soria, *J. Catal*. 194 (**2000**) 385.
[16] F. Bondioli, A. B. Corradi, T. Manfredini, *Chem. Mater*. 12 (**2000**) 324.
[17] J. A. Switzer, *Am. Ceram. Soc. Bull*. 66 (**1987**) 1521.
[18] Y. Zhou, R. J. Phillips, J. A. Switzer, J. *Am. Ceram. Soc*. 78 (**1995**) 981.
[19] T. V. Mani, H. K. Varma, A. D. Damodaran, K. G. K. Warrier, *Ceram. Int.* 19 (**1993**) 125.
[20] A. Bensalem, F. Bozon-Verduraz, M. Delamar, G. Bugli, *Appl. Catal. A* 121 (**1995**) 81.
[21] T. Miki, T. Ogawa, M. Haneda, N. Kakuta, A. Ueno, S. Tateishi, S. Matsuura, M. Sato, *J. Phys. Chem*. 94 (**1990**) 6464.

[22] M. H. Yao, R. J. Baird, F. W. Kunz, T. E. Hoost, *J. Catal*. 166 (**1997**) 67.
[23] N. Guillou, L. C. Nistor, H. Fuess, H. Hahn, *Nanostr. Mater*. 8 (**1997**) 545.
[24] W. Bui, K. L. Choy, N. H. J. Stelzer, J. Scoonman, *Solid State Ionic*s 116 (**1999**) 225.
[25] G. Avgouropoulos, M. Manzoli, F. Boccuzzi, T. Tabakova, J. Papavasiliou, T. Ioannides, V. Idakiev, *J. Catal.* 256 (**2008**) 237.
[26] A. J. Dyakonov, C. A. Little, *Appl. Catal. B: Environ.* 67 (**2006**) 52.
[27] D. Fino, V. Specchia, *Powder Technol.* 180 (**2008**) 64.
[28] E. Saab, E. Abi-Aad, M. N. Bokova, E. A. Zhilinskaya, A. Aboukais, *Carbon* 45 (**2007**) 561.
[29] M. Issa, C. Petit, A. Brillare, J.-F. Brilhac, *Fuel* 87 (**2008**) 740.
[30] A. Aboukais, E. A. Zhilinskaya, J.-F. Lamonier, I. N. Filiminaov, *Colloids Surf. A: Physicochem. Eng. Aspects* 260 (**2005**) 199.
[31] A. Bueno-Lopez, K. Krishna, B. van der Linden, G. Mul, J. A. Moulijn, M. Makkee, *Catal. Today* 121 (**2007**) 237.
[32] A. Bueno-Lopez, K. Krishna, M. Makkee, J. A. Moulijn, *J. Catal.* 230 (**2005**) 237.
[33] K. Krishna, A. Bueno-Lopez, M. Makkee, J. A. Moulijn, *Appl. Catal. B: Environ.* 75 (**2007**) 210.
[34] E. Aneggi, C. de Leitenburg, G. Dolcetti, A. Trovatelli, *Catal. Today* 114 (**2006**) 40.
[35] J. Liu, Z. Zhao, J. Wang, C. Xu, A. Duan, G. Jiang, Q. Yang, *Appl. Catal. B: Environ.* 84 (**2008**) 185.
[36] T. Mori, Y. Wang, J. Drennan, G. Auchterlonie, J.-G. Li, T. Ikegami, *Solid State Ionics* 175 (2004) 641.
[37] K. Krishna, A. Bueno-Lopez, M. Makkee, J. A. Moulijn, *Appl. Catal. B: Environ.* 75 (**2007**) 189.
[38] P. Mars, D.W. van Krevelen, Chem. Eng. Sci. 3 (**1954**) 41.
[39] J. Soria, A. Martinez-Arias, J. Conesa, *J. Chem. Soc. Faraday Trans.* 91 (**1995**) 1669.
[40] A. Martinez-Arias, J. Conesa, J. Soria, *Res. Chem. Intermed.* 33 (**2007**) 775.
[41] Li, C.; Domen, K.; Maruya, K.; Onischi, T. *J. Catal.* (**1990**), *123*, 436.
[42] V. V. Pushkarev, V. I. Kovalchuk, J. L. d'Itri, *J. Phys. Chem. B* 108 (**2004**) 5341.

[43] Y. M. Choi, H. Abernathy, H.-T. Chen, M. C. Lin, M. Liu, *Chem. Phys. Chem.* 7 (**2006**) 1957.
[44] J. Guzman, S. Carrettin, A. Corma, *J. Am. Chem. Soc.* 127 (**2005**) 3286.
[45] Huang, M.; Fabris, S.; *Phys. Rev. B* (**2007)**, *75*, 081404(R).
[46] Chen, H.-T.; Chang, J.G.; Chen, H.L.; Lu, S.-P. *J. Comput. Chem.* (**2009)**, *30*, 2433.
[47] Conesa, J. C. *Catal. Today* (**2009)**, *143*, 315.
[48] Linsebigler, A. L.; Lu, G.; Yates, J. T. *Chem. Rev.* (**1995)**, *95*, 735.
[49] Berger, T.; Sterrer, M.; Diwald, O.; Knözinger, E.; Panayotov, D.; Thompson, T. L.; Yates, J. T. *J. Phys. Chem. B* (**2005)**, *109*, 6061.
[50] Migani, A.; Vayssilov, G. N.; Bromley, S. T.; Illas, F.; Neyman, K. M. *Chem. Commun.* (**2010)**, *46*, 5936.
[51] C. Loschen, A. Migani, S. T. Bromley, F. Illas, K. M. Neyman, *Phys. Chem. Chem. Phys.* 10 (**2008**) 5730.
[52] M. M. Branda, C. Loschen, K. Neyman, F. Illas, *J. Phys. Chem. C* 112 (**2008**) 17643.
[53] N. V. Skorodumova, S. I. Simak, B. I. Lundqvist, I. A. Abrikosov, B. Johansson, *Phys. Rev. Lett.* 16 (**2002**) 166601.
[54] M. Nolan, S. Grigoleit, D. C. Sayle, S. C. Parker, G. W. Watson, *Surf. Sci*. 576 (**2005**) 217.
[55] P. J. Hay, R. L. Martin, J. Uddin, G. E. Scuseria, *J. Chem. Phys*. 125 (**2006**) 034712.
[56] D. Mei, N. Aaron Deskins, M. Dupuis, Q. Ge, *J. Phys. Chem. C* 111 (**2007**) 10514.
[57] M. B. Watkins, A. S. Forster, A. L. Shluger, *J. Phys. Chem. C* 111 (**2009**) 15337.
[58] P. Bera, K. C. Patil, M. S. Hedge, *Phys. Chem. Chem. Phys.* 2, 3715 (**2000**).
[59] M. Machida, Y. Murata, K. Kishikawa, D. Zhang, K. Ikeue, *Chem. Mater*. 20 (**2008**) 4489.
[60] D. A. Outka, J. Stöhr, W. Jark, P. Stevens, J. Solomon, E. J. Madix, *Phys. Rev. B* 35 (**1987**) 4119.
[61] P. A. Gravil, D. M. Bird, J. A. White, *Phys. Rev. Lett.* 77 (**1996**) 3933.
[62] E. Aneggi, J. Llorca, C. de Leitenburg, G. Dolcetti, A. Trovatelli, *Appl. Catal. B: Environ*. 91 (**2009**) 489.
[63] L. L. Murriel, R. T. Carlin, *J. Catal.* 159 (**1996**) 479.
[64] J. H. Wang, M.L. Liu, M. C. Lin, *Solid State Ionics* 177, 939 (**2006**).

[65] J. A. Farmer, C. T. Campbell, *Science* 329, 933 (**2010**).
[66] J. A. Farmer, J. H. Baricuatro, C. T. Campbell, *J. Phys. Chem. C* 114, 17166 (**2010**).
[67] D. Kong, G. Wang, Y. Pan, S. Hu, J. Hou, H. Pan, C. T. Campbell, J. Zhu, *J. Phys. Chem. C* 40 (**2011**).
[68] F. Esch, S. Fabris, L. Zhou, T. Montini, C. Africh, P. Fornasiero, G. Pomelli, R. Rosei, *Science* 309 (**2005**) 752.
[69] S. Fabris, G. Vicario, G. Calducci, S. de Gironcoli, S. Baroni, *J. Phys. Chem. B* 109 (**2005**) 22860.
[70] J. L. F. Da Silva, M. V. Ganduglia-Pirovano, J. Sauer, *Phys. Rev. B* 75 (**2007**) 045121.
[71] C. Loschen, J. Carrasco, K. M. Neyman, F. Illas, *Phys. Rev. B* 75 (**2007**) 035115.
[72] M. M. Branda, N. J. Castellani, R. Grau-Crespo, N. H. de Leeuw, N. C. Hernandez, J. F. Sanz, K. M. Neyman, F. Illas, *J. Chem. Phys*. 131 (**2009**) 094702.
[73] S. Altieri, L. H. Tjeng, G. A. Sawatzky, *Phys. Rev. B* 61 (**2008**) 16948.
[74] L. Savio, E. Celasco, L. Vattuone, M. Rocca, *J. Chem. Phys*. 119 (**2003**) 12053.
[75] D. M. Roessler, D. R. Huffman, *Handbook of Optical Constants of Solids II*, E. D. Palik Academic Press, (New York 1998).
[76] M. Sterrer, T. Risse, H.-J. Freund, *Appl. Cat. A: Gen*. 307 (**2006**) 58.
[77] G. Spoto, E. N. Gribov, G. Ricchiardi, A. Damin, D. Scarano, S. Bordiga, C. Lamberti, A. Zecchina, *Progr. Surf. Sci*. 76 (**2004**) 71.
[78] D. Scarano, S. Bertarione, F. Cesano, G. Spoto, A. Zecchina, *Surf. Sci*. 570 (**2004**) 155.
[79] A. Zecchina, D. Scarano, S. Bordiga, G. Ricchiardi, G. Spoto, F. Geobaldo, *Catal. Today* 27 (**1996**) 403.
[80] J. R. Schlup, S. Utamapanya, K. J. Klabunde, *Chem. Matt*. 3 (**1991**) 175.
[81] S. Singh, E. Knözinger, K. H. Jacob, *Surf. Sci*. 290 (**1993**) 175.
[82] D. M. Murphy et al. *J. Chem. Phys. B* 103 (**1999**)1944.
[83] J. A. Gates, L. L. Kesmodel, *Surf. Sci*. 124 (**1983**) 68.
[84] A. M. Stoneham, *Theory of defects in solids*. Oxford University Press, Oxford (1975).
[85] R. Wichtendhal et al. *Surf. Sci*. 423 (**1999**) 90.
[86] G. Pacchioni, *Surf. Rev. and Lett*. 7 (**2000**) 277.

[87] M. Chiesa, M. C. Paganini, E. Giamello, D. M. Murphy, C. Di Valentin, G. Pacchioni, *Acc. Chem. Res*. 39 (**2006**) 861.
[88] M. Kawamura, S. Furuyama, H. Fuijii, T. Morimoto, *J. Phys. Chem*. 82 (**1978**) 1028.
[89] G. Spoto et al. *Surf. Sci*. 540 (**2003**) L605.
[90] S. A. Chambers, *Surf. Sci. Rep*. 39 (**2000**) 105.
[91] J. W. He et al. *Surf. Sci*. 261 (**1992**) 164.
[92] P. S. Bagus, G. Pacchioni, T. Minerva, *Surf. Sci*. 275 (**1992**) 450.
[93] S. Cosuccia et al. *Spectrochim. Acta A* 49 (**1993**) 1289.
[94] S. Bagus, G. Pacchioni, G. Cogliandro *Int. J. Quant. Chem*. 42 (**1992**) 1115.
[95] G. Magnaccia, V. Bolis, G. Carrato, C. Mortera *Thermochim. Acta* 312 (**1998**) 63.
[96] A. Zecchina et al. *Adv. Catal*. 46 (**2001**) 265.
[97] A. J. Tench, M. M. Che *J. Adv. Catal*. 31 (**1982**) 78.
[98] G. Pacchioni, F. Illas, J. M. Ricart *J. Am. Chem. Soc*. 116 (**1994**) 10152.
[99] M. Chiesa, E. Giamello, C. Di Valentin, G. Pacchioni, Z. Sojka, S. Van Doorslaer, *J. Am. Chem. Soc.*, 127 (**2005**) 16935.
[100] M. Chiesa, F. Napoli, E. Giamello, *J. Phys. Chem. C*, 111 (**2007**) 548**.**
[101] E. Finazzi, C. Di Valentin, G. Pacchioni, M. Chiesa, E. Giamello, H. J. Gao, J. C. Lian, T. Risse, H-J. Freund, *Chem. Eur. Journal*,14 (**2008**) 4404**.**
[102] G. Preda, G. Pacchioni, M. Chiesa, E. Giamello *Phys. Chem. Chem. Phys.*, 37 (***2009***) 8156.
[103] H. Arakawa, M. Aresta, J. N. Armor, M. A. Barteau, E. J. Beckman, A. T. Bell, J. E. Bercaw, C. Creutz, E. Dinjus, D. A. Dixon, K. Domen, D. L. DuBois, J. Eckert, E. Fujita, D. H. Gibson, W. A. Goddard, D. W. Goodman, J. Keller, G. J. Kubas, H. H. Kung, J. E. Lyons, L. E. Manzer, T. J. Marks, K. Morokuma, K. M. Nicholas, R. Periana, L. Que, J. Rostrup-Nielson, W. M. H. Sachtler, L. D. Schmidt, A. Sen, G. A. Somorjai, P. C. Stair, B. R. Stults, and W. Tumas, *Chem. Rev.* 101 (**2001**) 953.
[104] H. Huber, D. McIntosh, G. A. Ozin, *Inorg. Chem.* 16 (**1978**) 975.
[105] H. J. Freund, M. W. Roberts, *Surf. Sci. Rep*. 25 (**1996**) 225.
[106] J. H. Lunsford, J. P. Jayne, *J. Phys. Chem.* 69 (**1965**) 2182.
[107] M. Chiesa, E. Giamello, *Chem. Eur. J.* 13 (**2007**) 1261.
[108] M. E. Jacox, W. E. Thompson, *J. Chem. Phys.* 91 (**1989**) 1410.
[109] D. W. Ovenall, D. H. Whiffen, *Proc. Chem. Soc.* (**1960**) 420.

[110] R. Köppe, P. H. Kasai, *J. Phys. Chem.* 98 (**1994**) 11331.
[111] Z. H. Kafafi, R. H. Hange, W. E. Billups, and J. L. Margrave, *J. Am. Chem. Soc.* 105 (**1983**) 3886.
[112] B. Mile, *Angew. Chem.* 80 (**1968**) 519; *Angew. Chem. Int. Ed. Eng.* 7 (**1968**) 507.
[113] Z. H. Kafafi, R. H. Hauge, E. Billups, J. L. Margrave, *Inorg. Chem.* 23 (**1984**) 177.
[114] J. E. Bennett, S. C. Graham, B. Mile, B. *Spectrochim. Acta Part A* 29 (**1973**) 375.
[115] P. Meriaudeau, J. C. Vedrine, Y. Ben Taarit, C. J. Naccache, *J. Chem. Soc. Faraday Trans. I,* 2 (**1975**) 736.
[116] J. Nerlov, S. V. Christensen, S. Weichel, E. H. Pedersen, P. J. Møller, P. J.; *Surf. Sci.* 371 (**1997**) 321.
[117] O. Seiferth, K. Wolter, H. Kuhlenbeck, H. J. Freund, *Surf. Sci.* 505 (**2002**) 215.
[118] D. Ricci, C. Di Valentin, G. Pacchioni, P. V. Sushko, A. L. Shluger, E., *J. Am. Chem. Soc*. 125 (**2003**) 738.
[119] M. Chiesa, M. C. Paganini, E. Giamello, C. Di Valentin, G. Pacchioni, *Angew. Chem. Int. Ed*. 42 (**2003**) 1759.
[120] M. Chiesa, M. C. Paganini, E. Giamello, C. Di Valentin, G. Pacchioni, *ChemPhysChem*, 7 (**2006**) 728.
[121] M. Chiesa, M. C. Paganini, G. Spoto, E. Giamello, C. Di Valentin, A. Del Vitto, G. Pacchioni, *J. Phys. Chem. B*, 109 (**2005**) 7314.
[122] D. R. Smith, A. J. Tench, *Chem. Commun*. (**1968**) 1113.
[123] G. Preda, G. Pacchioni, M. Chiesa, E. Giamello, *J. Phys. Chem. C*, 112 (**2008**) 19568.
[124] M. Anpo, M. Che, B. Fubini, E. Garrone, E. Giamello, M. C. Paganini, *Topics Catal*, 8 (**1999**) 189.
[125] R. Davydov, J.D. Satterlee, H. Fujii, A. Sauer-Masarwa, D.H. Busch, B.M. Hoffman, *J. Am. Chem. Soc*., 125 (**2003**) 16340.
[126] G. Henrici-Olivè, S. Olivè, *Angew. Chem. Int. Ed.*, 13 (**1974**) 29.
[127] Z. Sojka, *Cat.Rev.Sci.Eng.*, 37 (**1995**) 461.
[128] M. Che, A. J. Tench, *Adv. Catal.*, 31 (**1982**) 77.
[129] M. Chiesa, M. C. Paganini, E. Giamello, D. M. Murphy, *J. Phys. Chem. B*, 105 (**2001**) 10457.

Chapter 2

Computational methods

In this work, several methods were used to calculate the properties of different systems. Hartree-Fock, UMP2 and CCSD were used in Chapter 3 to model MCO_2 complexes. DFT/B3LYP was used to simulate both MgO surface in cluster model calculations (Chapter 3 and 4) and the cluster Ce_2O_3 in Chapter 6. For periodic calculations of ceria surfaces, both the LDA+U and GGA+U approach were used in Part II.

2.1 Hartree-Fock method

Calculation of the observables of a polyelectronic system with quantum-mechanical methods requires the solution of the Schrödinger equation. An exact solution is possible just for monoelectronic systems, while for polyelectronic ones only approximated solutions can be achieved. Thus, it is necessary to introduce some approximations, the first of which is the so-called adiabatic approximation.[1]

In the adiabatic Born-Oppenheimer approximation, the electronic component is considered independent on the one of the nuclei, due to the huge difference between their masses, and so, between the dynamic properties of the particles. From this statement comes a parametric dependence of the electronic part on the nuclear one, that lets express the eigenfunction of the whole system as a product of the eigenfunctions (Eq. 2.1), and the complexive Hamiltonian as a sum of the Hamiltonians of the two groups of particles, Eq. 2.2.

$$\Psi(r_i, R_n) = \psi(r_i, R_n) \cdot \chi(R_n) \qquad \textbf{Eq 2.1}$$

$$H = H_{e^-} + H_{ion} \qquad \textbf{Eq 2.2}$$

The electronic energy and eigenfunction are thus obtained resolving a time independent Schrödinger equation in which the terms deriving from the nuclear component have been neglected, Eq. 2.3.

$$H_{e^-}\psi(r_i, R_n) = \varepsilon_{e^-}\psi(r_i, R_n) \forall R_n$$

$$H_e = \sum_{i=1}^{N}\left(-\frac{\hbar^2}{2m}\nabla^2 - Ze^2\sum_R \frac{1}{|r_i - R|}\right) + \frac{1}{2}\sum_{i\neq j}\frac{e^2}{|r_i - r_g|}$$

Eq 2.3

Because of the parametric dependence of the electronic eigenfunction from the nuclear coordinates a reiteration of the calculation for each configuration of interest is necessary.

The terms of Eq. 2.3 are the kinetic energy of the electrons, the nuclear attraction and the interelectronic interaction. The analytic resolution of the equation is impossible because of the presence of the interelectronic potential energy. The first attempt to resolve the electronic interaction problem, proposed by Hartree,[2] considers all the electrons in the mean field approximation. When the Schrödinger equation is put into the potential energy generated by the charge distribution it is possible to obtain a set of one-electron equations, named Hartree equations (Eq 2.4).

$$\left[-\frac{\hbar^2}{2m}\nabla^2 - \sum_R \frac{Ze^2}{|r_i - R|} + e^2 \sum_j \int dr' \frac{|\psi_j(r')|^2}{|r - r'|} \right] \psi_i(r) = \varepsilon_i \psi_i(r)$$

Eq. 2.4

This model presents two fundamental limitations. First of all, the mean field approximation fails in considering the effects due to the interelectronic interaction, such as the exchange interaction. Moreover, based on the variational principle, the Hartree equations are the best approximation to the wavefunction of a system made up of *N* non-interacting electrons, that can thus be expressed as a simple product of *N* single-particle wavefunctions, not compatible with the Pauli exclusion principle, which needs the antisymmetrization of the wavefunction.

The Hartree-Fock model is the most simple generalization of the Hartree model that takes into account this requirement. To this respect the wavefunction is then written as a Slater determinant, made up of *n* rows, the number of the electron, and *n* columns, the number of the spin-orbitals.

The application of the variational principle leads in this case to a generalization of the Hartree equations that includes also the exchange term, which comes from the exclusion principle, that takes into account the correction needed by the electronic interaction in the Hartree model. One of the main characteristics of this mean field approach is the problem of autoconsistency due to the interdependence between the potential (Hartree term with the exchange interaction) and the wavefunction, that can be solved through an iterative calculation. In fact, the Schrödinger equation is solved chosing a starting potential, the obtained wavefunctions are thus used to calculate the resulting one, and then a new equation is solved. This procedure, called self-consistent field (SCF), is repeated

until the calculation reaches the convergence, which means that the potential differs from the previous less than a tolerance established a priori. However, the Hartree-Fock method shows a great lack because it does not consider the istantaneous electrostatic interactions between electrons, nor takes into account the quantum-mechanical effects on the electronic distribution, by the fact that the effective potential on the considered electron given by the nuclei and by the other *N-1* electrons is taken just in the mean field approximation.

The exact non relativistic energy of the ground state in the environment of the Born-Oppenheimer approximation can be obtained expressing the exact wavefunctions of the ground and excited states as linear combinations of all the possible *N*-electrons Slater determinants deriving from a complete system of spin-orbitals. This procedure is called Configuration Interaction, CI.[3,4] The energy difference between the so-calculated energy and the Hartree-Fock limit is called Correlation Energy (see following Section).

Considering the approximation regarding the explicit analytic expression of the spatial part of the monoelectronic functions, the Hartree-Fock orbitals are expanded as a linear combination of functions, called basis function or basis set. In general, the basis functions are atomic functions (atomic orbitals), and each molecular orbital, MO, is expressed as a linear combination of *M* atomic functions (LCAO, Linear Combination of Atomic Orbitals). The most obvious choice for the basis functions to use in the expansion of the molecular orbitals are the atomic orbitals centred in the nucleus of each atom, if the building model of a molecule starting from the atoms that compose it is chosen. For each atom, all the shells in which there is at least one occupied atomic orbital are considered. When the basis set is made up of just one basis function for each considered atomic orbital, it is called minimum basis set. The general

analytic form of the basis functions used in molecular calculations comes form the AO obtained by the exact solution of the Schrödinger equation for the hydrogen atom. The ones obtained for the hydrogen atom are used as angular functions, while two different sorts of radial functions are used, STO (Slater Type Orbital) or GTO (Gaussian Type Orbital). The STOs show a right behavior in the limits r = 0 and r = ∞, but for calculations GTO are preferred, so in order to reproduce the same trend of a STO orbital, a linear combination of *k* GTO is necessary.

2.2 MP2 and CCSD(T)

In the Hartree-Fock method the HF equation is an approximation of the Schrödinger equation, that claims that the wavefunction can be represented by a single Slater determinant. Moreover, each electron interacts with a mean charge distribution generated by the other *N-1* electrons. In this approximation the HF method completely ignores the contribution to energy due to the correlation energy, in fact the movement of the electrons is correlated, as the Coulomb law states. Thus, the definition of correlation energy comes from the difference between the non-relativistic exact energy of the system and the Hartree-Fock energy obtained for a complete set of basis functions. To calculate the exact wavefunction (Φ_e), it can be expressed as a linear combination of a complete set of *N*-electronic basis functions. Thus, a set of Slater determinants forms a set of basis functions for the expansion of Φ_e, that can be exactly expanded if the set is endless. To obtain a set of Slater determinants, it must be considered that from the HF solution comes a number of molecular orbitals *M* which is the same number of the basis functions used during the calculation. In the *N*-electronic

situation *N/2* orbitals will be occupied and *M-N/2* will be virtual. The *N/2* occupied orbitals are used to have the Ψ_{HF} Slater determinant. The other determinants can be generated by substitution of the occupied molecular orbitals in Ψ_{HF} with virtual orbitals. It is important to say that the Slater determinants of the expansion must have the same spin (S_Z e S^2) and spatial symmetry. To calculate the expansion coefficients two theories are available, the variational and the perturbational theory.

In the variational one the coefficients are determined through a minimization of the total energy, diagonalizing the matrix of the Hamiltonian operator in the Slater determinants basis. This method is called Configuration Interaction (CI). In the CISD (CI Singles and Doubles) the determinants that have a double excitation are the ones which contribute more in the CI expansion, which means that it is possible to demonstrate that the correlation energy is determined just by the coefficients of the determinants with double excitation. However this does not mean that considering just these is enough to have the exact CI description of the fundamental state, in fact the coefficients are calculated considering the other interactions too.

In the perturbation theory the HF determinant is treated as a zero-order solution and the repulsion term $1/r_{ij}$ is put as a perturbation of the Fock operator. The first order energy is the E_{HF}, the second order one depends on the doubly excited determinants and so on. This method is called Møller-Plesset (MPn) method. In MP2 the energy correction is of the second order and there are just doubly excited determinants, in MP4 the calculation of the fourth order energy considers also the triply and quadruply excited determinants.

While the perturbational methods consider all the sorts of correction of the considered wavefunction for a chosen order of the perturbation, the Coupled-Cluster (CC) method considers all the correction of a certain type till an infinite order. This is an extremely

accurate and size-consistent method, but with a huge computational cost. The CCSD method involves the calculation of matrix elements between singly and triply excited determinants and between doubly and quadruply excited determinants.

2.3 Density Functional Theory

The Density Functional Theory (DFT) is a quantum mechanical theory to investigate the electronic structure, mainly the ground state, of many-body systems. In this theory the total electron energy of the system can be expressed as a functional of the ground state electron density ρ(r). The electron density, as a wavefunction, brings all the informations regarding the system, but with the advantage to be a physical observable and to be mathematically much simpler. The formal proof of the univocal dependence of the ground state electronic properties on the electron density was given by the Hohenberg and Kohn theorems[5] at the beginning of the ’60. The first of the two theorems says that the ground state properties of a many-electron system are uniquely determined by an electron density that depends on only three special coordinates. This simplifies the many-body problem from three spatial coordinates for each of the *N* atoms constituting the system to just three spatial coordinates.

The second Hohenberg-Kohn theorem defines an energy functional for the system and proves that the correct ground state electron density minimizes this energy functional. In the context of Kohn-Sham DFT,[6] the intractable many-body problem of interacting electrons in a static external potential is reduced to a tractable problem of non-interacting electrons moving in an effective potential. Non-interacting systems are easier to solve because the

wavefunction can be represented as a Slater determinant of orbitals. The effective potential includes the exchange and correlation interactions, in fact it involves the external potential and the effects of the Coulomb interaction between the electrons.

The main drawback of DFT is that the exact form of the functional for exchange and correlation is known for the free electron gas only. However, approximations allow the calculation of certain physical quantities quite accurately. In physics the most widely used approximation is the local density approximation (LDA), where it is assumed that the electron density can be treated as a uniform electron gas (jellium). The exchange and correlation term can be exactly calculated for the electron gas, so this is a very powerful approximation. Thus, this is exact just for an ideal metal, but it gives good results for those systems in which the electron density is more or less homogeneous. Nevertheless this approximation has a limited validity because near the nuclei the charge density undergoes rapid and big variations. Generalized gradient approximation (GGA) is still local but also takes into account the gradient of the density at the same coordinate. With this more sophisticated approximation, very good results for molecular geometries and ground-state energies have been achieved.

Some exchange and correlation functionals of this sort, like the Perdew-Wang's (PW) or the Becke's ones, are calculated as a correction added to the LDA functional, while the Lee, Yang and Parr's (LYP) functional completely reformulates the classical auto-interaction energy for a monoelectronic system, optimizing four parameters for the helium atom.

Becke also proposed a hybrid functional based on the optimization of three parameters *a,b* and *c* (B3 functional) in which the DFT contribution to the exchange functional is calculated at the LDA level, which the Becke's correction dependent on the gradient

is added to. When the correlation functional is the LYP one, the whole hybrid functional is called B3LYP: [7,8]

$$E_{xc}^{B3LYP} = (1-a)E_x^{LDA} + aE_x^{HF} + b\Delta E_x^B + (1-c)E_c^{LDA} + cE_c^{LYP}$$

Eq 2.5

Indeed, including a component of the exact exchange energy calculated from the Hartree-Fock theory can relieve the difficulties in expressing the exchange part of the energy. In B3LYP the contribution is 20% HF and 80% DFT.

In this work three different functionals have been used. The B3LYP hybrid functional has been employed as implemented in the embedded cluster methods, used in MgO modeling (see Part I). For the plane waves calculations, used to calculate ceria surfaces in Part II, LDA and GGA functional PW91 were used.

2.4 DFT+U

A pure density functional theory approach, both in the local density approximation (LDA), and in the more sophisticated generalized gradient approximation (GGA) is not able to properly describe materials with a half-filled *d* or *f* shells. In fact for example wide gap antiferromagnetic insulators transition metal oxides, such as FeO, CoO or MnO are predicted to be small-gap semiconductors or even metals. The Kohn-Sham equations have a mean-field character and the strong correlation effects, that are extremely important for this kind of materials, are poorly described.

In the ’90, Anisimov and coworkers[9,10] proposed an efficient method to describe the correlated materials. This approach is called DFT+U, where the classical DFT approach is combined with a

multiorbital mean-field Hubbard model, that includes the on-site Coulomb interaction in the Hamiltonian. The main advantage of this technique is the possibility to have a good decription of both electron-electron interactions and the chemical bonding, although it remains a mean-field method.[11]
In our calculations of CeO_2 we used the DFT+U as implemented in the VASP code (see Sec. 2.6). Within the framenwork of the Dudarev approach,[12] the DFT+U spin polarized functional can be written as in Eq. 2.6.

$$E_{DFT+U} = E_{DFT} + \frac{U-J}{2}\sum_{m,\sigma}\left(n_{m,\sigma} - n_{m,\sigma}^2\right) \qquad \textbf{Eq. 2.6}$$

In Eq 2.6, *n* are the electrons yielding the quantum number *m* and the spin σ, J is the parameter that represents the screened exchange energy and U is defined as follows (Eq. 2.7).

$$U = E\left(d^{n+1}\right) + E\left(d^{n+1}\right) - 2E\left(d^{n}\right) \qquad \textbf{Eq. 2.7}$$

This equation describes the energy increase for placing an extra electron on a particular site.[13] Thus, the new parameter that enters into the calculations is the $U_{eff} = U - J$. J is an approximation to the Stoner exchange paramenter, and can be fixed to ~1 eV, while U depends on the spatial extension of the wavefunction and on the screening.
Considering the VASP implementation, U_{eff} is an empirical parameter and the value has to be determined investigating its dependency on the variable of interest.

For our simulations of cerium oxide we used U_{eff} = 5 eV for LDA+U calculations and U_{eff} = 3 and 4 eV for GGA+U calculations. These values are applied to the Ce 4*f* orbitals and are reported in

literature.[14] In this cited work the impact of this parameter on several structural and electronic observables of ceria has been investigated in a systematic way, and it was found that the optimal value of U_{eff} is considerably dependent on the property under examination. However, a well balanced choice of U_{eff} is proposed to be at 5 – 6 eV for the LDA+U calculations and at 2 – 3 eV for the GGA+U ones. In particular LDA+U with U_{eff} = 5 eV was used in our work to calculate structural and magnetic parameter, while a GGA+U single point calculation on the optimized geometry gave the energetic values. Considering GGA+U calculations, we chose at first U_{eff} = 3 eV, but then we shifted to 4 eV because it helps the convergency of the calculations, giving at the same time good energetic results.

2.5 Embedded cluster model calculations

Localized phenomena, as for example the adsorption of molecule or the presence of point defects can be modeled with the cluster approach in an infinite diluition regime. This model, called cluster model, consists of cutting a portion of the considered material out of the ideal infinite crystal, in order to take into account the minimum amount of atoms required to describe the property of interest. The main problem that can arise using this procedure with ionic oxides is the description of the long-range electrostatic potential, the Madelung potential, which is a crucial characteristic of ionic lattices, such as MgO.

The usual approach to reproduce the Madelung potential is generating a finite array of point charges (PCs) located in lattice positions, whose values in the case of a strongly ionic materials are the nominal charges of the ions. The main drawback of this model is

the non-physical polarization that the anions at boundaries of the quantum-mechanical cluster experience, which is due to the presence of nearby positive point charges. This artificial effect can be fixed by replacing the positive point charges at the interface with the quantum-mechanical cluster with effective core potentials (ECPs). ECPs simulate the exchange repulsion preventing non-physical polarizations.[15]

The embedding model with point charges does not take into account the long-range polarization due to the presence of a defect or an adsorbate, especially when it is charged or polarized.

In this work (Part I) the method developed by Sushko and Shluger[16,17] was used. In this model a quantum-mechanical cluster is immersed in a finite lattice of polarizable ions described as shell models (Figure 2.1), called region I. In such an approach polarizable ions are described as made up of two point charges, a positive one for the core, and a negative one for the shell, coupled by an harmonic potential. The displacement of the shell with respect to the core simulates the polarization of a classical ion in the presence of an electric field (Figure 2.1).

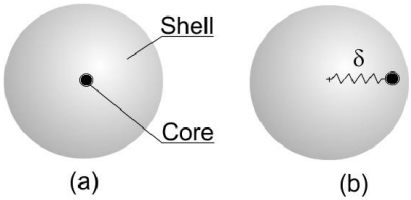

Figure 2.1: Schematic representation of the classical model (shell model) used to describe a polarizable ion. It is made up of two point charges, the core and the shell. The two charges are linked by a spring, and when they are immersed in an electric field they depart till an equilibrium distance δ (b).

The obtained lattice is then immersed in another finite lattice, with much bigger dimensions, made up of just point charges, called region II. This second lattice is needed to give the external electrostatic long range potential to region I and to the quantum-mechanical cluster (Figure 2.2).

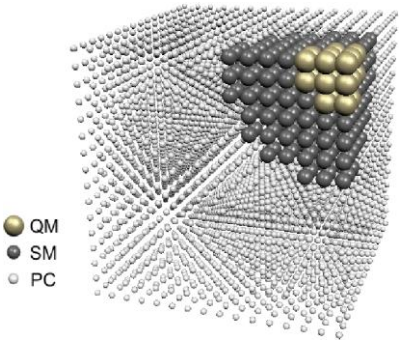

Figure 2.2: Scheme of the embedding model for a corner site of a cubic oxide like MgO. The quantum mechanical cluster (QM) is surrounded in the finite lattice (region I) of polarizable ions described with the shell model. This region is then immersed in a bigger lattice of point charges (PC) that gives the region II.

The total energy of the system is therefore the sum of the following contributions:

- Energy of the quantum-mechanical cluster, in presence of the external field due to charges and dipoles of the embedding scheme;
- Coulomb interaction energy between charges of the classical regions (core and shells);
- Short range interaction between shell model ions;
- Harmonic potential energy between every core and the corresponding shell;

- Short range Coulomb interaction between QM atoms and the ions of the embedding.

It can thus be written in the following way (Eq. 2.8):[17]

$$E_{TOT} = \langle \psi | H_0 + V_{emb} | \psi \rangle + \tfrac{1}{2} \sum_{i,j \in emb} \frac{q_i q_j}{R_{i,j}} + \tfrac{1}{2} \sum_{i,j \in emb} W_{i,j} + \tfrac{1}{2} \sum_{i \in emb} k_i \delta_i^2 + \sum_{i \in QM} \sum_{j \in emb} W_{i,j}$$

Eq. 2.8

The optimization algorithm developed for this model allows the simoultaneous optimization of the coordinates of the quantum mechanical part and the classical (region I) parts.

Most of the electron density is localized around atoms and along the bonds so, localized atom-like functions are a natural choice for a basis set, such as linear combinations of GTOs (see Sec. 2.1).
The embedded cluster model approach has been used for the calculations shown in Chapter 3 and 4.

2.6 Periodic supercell calculations

Considering solids, the electronic structure is usually described in terms of band structure. With this respect, a commonly adopted approach is the use of a unit cell with appropriate dimensions periodically repeated in the three-dimensional space to take into account the infinite nature of the crystalline solid. Thus, the Schrödinger equation is solved for the atoms in the unit cell, which undergoes periodic boundary conditions (PBC).[18] This model can also be used for the study of surfaces, combining the PCB with the slab approach, in which the unit cell is made up of a given number of

layers. Generally, some of them are in fixed positions, constrained to resemble the bulk structure, and above the layers a wide enough region of vacuum lays in order to ensure the non-interaction between neighbor cells. Localized phenomena, such as point defects and the adsorption of molecules can be modeled with the periodic approach considering a large enough cell called supercell, in order to avoid a non-realistic reply that would result in an extremely high concentration of defects or molecules that could interact with each other. This approach was used in this work to calculate ceria surfaces in Part II.

The periodic quantum-mechanical code used in this work is the Vienna Ab-initio Simulation Package (VASP).[19,20] This code is based on the DFT and so the wavefunction of the system is decribed in terms of Kohn-Sham orbitals.[5,6] While in the cluster calculations the LCAO-MO (Linear Combination of Atomic Orbitals – Molecular Orbitals) and a gaussian-type basis set are used to describe the molecular orbitals, in the periodic calculations a basis set that takes advantages of the periodic nature of the potential is chosen. The Bloch theorem, that describes the single electron wavefunction in the Kohn-Sham equation, states that the wavefunction can be expressed as a cell-periodic part modulated by a wave-like function:[21]

$$\psi_{nk}(r) = e^{ik\cdot r} u_{nk}(r) \qquad \textbf{Eq. 2.9}$$

In (Eq. 2.9) $u_{n,k}(r)$ is the periodic function, with *n* band index. The single electron wavefunction can thus be written as:

$$\psi_{nk}(r+R) = e^{ik\cdot R}\psi_{nk}(r) \qquad \textbf{Eq. 2.10}$$

where R is a translational vector. The importance of this theorem lays in the fact that each electronic wavefunction can be written as a sum of plane waves:

$$\psi_{nk}(r) = \sum_{G} c_{n,k+G} e^{i(k+G)\cdot r} \qquad \textbf{Eq. 2.11}$$

Considering **l** a lattice vector of the crystal and *m* an integer, **G** is the reciprocal lattice vector defined as $\mathbf{G} \cdot \mathbf{l} = 2\pi m$ for all **l**. From what exposed, it is possible to understand that in principle an infinite plane-wave basis set is necessary to expand the electronic wavefunction. Actually, the expansion can be truncated, including only the wavefunctions with a kinetic energy under a fixed threshold, in fact the coefficients $c_{n,k+G}$ are more important for the plane waves with small kinetic energy than for those with a higher one. In practice, only those plane waves $|G + k|$ for which

$$\frac{\hbar^2}{2m_e}|G+k|^2 < E_{cut} \qquad \textbf{Eq. 2.12}$$

are included. So, the use of a kinetic cut-off, combined with the Bloch theorem, allows to have a finite basis set for the description of the system. However, this leads to a computational error in the calculation of the total energy that can be reduced increasing the value of E_{cut} until the energy is converged. The electronic states are allowed for just a given set of *k* vectors in the reciprocal lattice. These vectors constitute a subspace of points (*k*-points) that can sample in a significative way the first Brillouin zone.[22] The VASP code uses the Monkhorst-Pack method[23] to generate a set of k-points to evaluate the electronic states. This is done in order to obtain an accurate approximation to the electronic potential and the

contribution to the total energy from a filled electronic band. This method uses a grid of k-points, whose density depends on band dispersion. Semiconductors and insulators are very well described by this approach using a very small number of k-points. However, to obtain a good description of metals a denser grid of k-points is necessary in order to precisely define the Fermi surface. Anyway, using big supercells the number of k-points can be reduced, because the relation between reciprocal and direct vectors is of inverse proportionality.

In the VASP code the implementation of the Fast Fourier Transform (FFT) is very efficient from a computational point of view. However, also in this case the number of required plane waves would exceed any practical limit for systems more complicated than hydrogen or lithium. Even when the cutoff energy is introduced, too many plane waves are needed to describe the core electrons. Considering this, pseudopotentials must be used instead of exact potentials, allowing a reduction in the number of electrons explicitly described and the possibility to use a lower E_{cut}. In a classical description of the system, the electron near the nucleus gains kinetic energy, because it is accelerated. The energy gain balances the potential energy loss due to the presence of the nucleus and the total energy is then kept constant. The increase of kinetic energy can be raplaced using an effective repulsive potential which cancels the electrostatic one. However, the real system can not be just classically described, then the deletion is not total because of the quantum-mechanical nature of the system. The remaining is the so-called pseudopotential.[24] Most of the physical properties of the solids are related not to the core electrons, almost unperturbed, but to the valence ones. In a quantum-mechanical description of the problem, as required by the Pauli principle, the wavefunction oscillates holding the orthogonality between the core and the valence

wavefunctions. The pseudopotential acts on the pseudo-eigenfunctions, which do not have nodes and converge quickly, instead of the real valence wavefunctions,[5] as it is schematically shown in Figure 2.3.

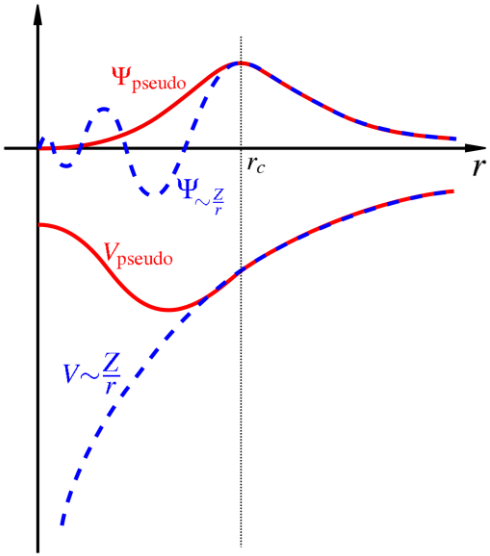

Figure 2.3: Schematic illustration of all-electron (dashed lines) and pseudoelectron (solid lines) potentials and their corresponding wavefunctions. At r_c the radius at which the values of all-electrons and pseudoelectrons match.

Unless this approximation might seem a bit crude, it is very accurate, in particular in systems where the electrons near the nucleus do not significatively contribute to the considered phenomena. There are several methods to build pseudopotentials, in this work projected augmented waves (PAW) method pseudopotentials[11,25] have been used.

In 1994 Blöchl proposed a method to obtain the electron-ion interaction, called Projector Augmented Wave (PAW). This method describes the wavefunction as an overlap of different terms. The first part is a plane wave, the pseudo-wavefunction, and the second one is an expansion on pseudo-orbitals and atomic orbitals for each atom. The plane wave shows the correct flexibility to describe the bonds and the external regions of the wavefunction, and the right behaviour of the nodal structure of the nuclei is garanteed by the expansion through atomic orbitals. The PAW method combines the advantages of both representation in a well-defined basis set to find the all-electron wavefunction, the energy functional and all the other needed physical quantities. This is usually considered an all-electron method, not in the sense that all the electrons are treated, but because the valence electronic wavefunctions are kept orthogonal to the core states.

The periodic supercell approach has been used in Part II .

2.7 Bibliography

[1] M. Born, R. Oppenheimer, *Ann. Phys*. 84 (**1928**) 457.
[2] N. W. Ashcroft, N. D. Mermin, Solid State Physics, Thompson/Brooks/Cole International Student Edition (**1976**).
[3] R. J. Buenker, S. D. Peyerimhoff, *Theoret. Chem. Acta* 35 (**1974**) 33.
[4] R. J. Buenker, S. D. Peyerimhoff, W. Butscher, *Mol. Phys*. 35 (**1978**) 771.
[5] P. Hohenberg, W. Kohn, *Phys. Rev. B* 136 (**1964**) 864.
[6] W. Kohn, L. J. Sham, *Phys. Rev. A* 140 (**1965**) 1133.
[7] A. D. Becke, *J. Chem. Phys*. 98 (**1993**) 5548.
[8] C. Lee, W. Yang, R. G. Parr, *Phys, Rev. B* 37 (**1998**) 785.
[9] V. I. Anisimov, J. Zaanen, O. K. Andersen, *Phys. Rev. B* 44 (**1991**) 943
[10] V. I. Anisimov, M. A. Korotin, J. Zaanen, O. K. Andersen, *Phys. Rev. Lett.* 68 (**1992**) 343.
[11] O. Bengone, M. Alouani, P. Blöchl, J. Hugel, *Phys. Rev. B* 62 (**2000**) 392.
[12] S. L. Dudarev, G. A. Botton, S. Y. Savrasov, C. J. Humphreys, A. P. Sutton, *Phys. Rev. B* 57 (**1998**) 1505.
[13] A. Rohrbach, J. Hafner, G. Kresse, *Phys. Rev. B* 69 (**2004**) 075413
[14] C. Loschen, J. Carrasco, K. M. Neyman, F. Illas, *Phys. Rev. B* 75 (**2007**) 035115.
[15] W. J. Stevens, H. Basch, M. J. Krauss, *J. Chem. Phys*. 81 (**1984**) 6026.
[16] P. V. Sushko, A. L. Shluger, A. Baetzold, C. R. A. Catlow, *J. Phys. Cond. Matt*. 12 (**2000**) 8257.
[17] P. V. Sushko, A. L. Shluger, C. R. A. Catlow, *Surf. Sci*. 450 (**2000**) 153.
[18] J. Hagen, L. D. Socaciu, M. Elijazyfer, U. Heiz, T. M. Bernhardt, L. Wste, *Phys. Chem. Chem. Phys*. 4 (**2002**) 1707.
[19] G. Kresse, J. Hafner, *Phys. Rev. B* 47 (**1993**) R558.
[20] G. Kresse, J. Furthmüller, *Phys. Rev. B* 54 (**1996**) 11169.
[21] N. Ashcroft, N. Mermin, *Solid State Physics*, International Thomson Publishing (Philadelphia **1976**)
[22] M. C. Payne, M. P. Teter, D. C. Allan, T. A. Arias, J. D. Joannopoulos, *Rev. Mod. Phys*. 64 (**1992**) 1047.
[23] H. Monkhorst, J. Pack. *Phys. Rev. B* 13 (**1976**) 5188.
[24] A. P. Sutton, *Electronic Structure of Materials*, Clarendon Press (Oxford **1993**).
[25] P. E. Blöchl, *Phys. Rev. B* 50 (**1994**) 17953.

PART I

Model system: electron transfer on MgO surfaces

Chapter 3

CO_2/K adsorbed on MgO powders

3.1 Summary

With a combined quantum chemical and experimental study we show the formation of CO_2^- radicals by contact of CO_2 molecules with a K precovered MgO surface, in order to study an example of activation of an adsorbed species by charge transfer from an activated oxide surface. Experimentally, after depositing K atoms on polycrystalline MgO samples, the system is exposed to CO_2. The typical EPR signal of the isolated K atoms disappears when the reaction with CO_2 takes place and the signal due to the formation of CO_2^- is observed. Our DFT cluster model calculations prove that there is a spontaneous electron transfer from the adsorbed K atom to the CO_2 molecule, with subsequent formation of $K^+CO_2^-$ surface complexes. These species have the same electronic characteristics and spin distribution of gas-phase $M^+CO_2^-$ (M = Li, Na, K) molecules, but are stabilized by the presence of the ionic surface. We analyze the most stable MgO sites where the adsorption of CO_2 occurs and we compare the computed EPR properties with the experimental values. The experimental results have been provided by the group of Prof. Giamello of the Università di Torino.

3.2 Computational details

The energetics, structure and stability of KCO_2 complexes formed at the surface of MgO have been investigated in the framework of the embedded cluster scheme implemented in the GUESS code[1] interfaced with the Gaussian03 code[2] (see Sec 2.5). In order to properly account for the formation of strong dipoles on the surface, resulting from the internal charge transfer in the $K^+CO_2^-$ units, we have used the shell-model approach. The quantum-mechanical region (QM), is surrounded by a region of about 300 classical ions whose polarizability is described by a shell-model (SM). Cations at the interface between the SM and the QM region are replaced by ions (hereafter indicated as Mg*) on which a semi-local effective pseudopotential (ECP) is centered, in order to reproduce the Pauli repulsion and avoid the non-physical polarization of QM interface anions. Region I, QM and SM, is then surrounded by a large array of point charges (PC) in order to reproduce the long-range electrostatic potential correctly.

All centers in QM region and Mg* interface atoms have been allowed to move during the optimization, while only shells, not cores, have been relaxed in the SM region. Therefore, the electronic polarization has been included in a large portion of the surface, while ionic polarization is restricted to a few tens of atoms. The total energy of the hybrid system is obtained as a sum of classical and QM contributions. The total energy and the electronic structure of the QM cluster are calculated at the DFT-B3LYP level (see Sec. 2.3).

The following QM clusters have been used to model morphological defects on the MgO surface:

- $Mg_{10}O_{10}Mg^*_{14}$ (edge)
- $Mg_{10}O_{10}Mg^*_{9}$ (corner)

- $Mg_{17}O_{17}Mg^{*}_{20}$ (cationic reverse corner)

The basis sets used are: 6-31G on Mg, 6-31G* on O, 6-311+G* on K and on the CO_2 molecule. CO_2 has a negative electron affinity, EA = –0.6 eV,[3] indicating that the extra electron is unbound. Thus, the radical CO_2^- is metastable because of the barrier associated to the geometry change from bent CO_2^- to linear CO_2. The computed EA is -0.37 eV using the 6-311+G* basis set and the B3LYP hybrid functional.

In order to verify the accuracy of the computational approach, we have calculated the Li-CO_2, Na-CO_2, and K-CO_2 gas-phase complexes using different basis sets (aug-cc-pVDZ, aug-cc-pVTZ, and aug-cc-pVQZ) and comparing wavefunction based methods such as Hartree-Fock (HF), unrestricted Moller-Plesset at second order (UMP2), and coupled cluster [CCSD(T)] (see Sec. 2.2) with hybrid DFT (B3LYP).

The hyperfine interactions of the electron spin with the nuclear spin of the ^{7}Li, ^{23}Na, ^{39}K, ^{13}C and ^{17}O nuclides have been computed. The hyperfine spin-hamiltonian, $H_{hfc} = \mathbf{S} \cdot \mathbf{A} \cdot \mathbf{I}$, is given in terms of the hyperfine matrix **A** which describes the coupling of the electron with the nuclear spin.[4] **A** can be represented as the sum of a isotropic (a_{iso}) and a dipolar part B (B is 3x3 traceless matrix).

To evaluate the deviations of the *g* values of MCO_2 complexes from the free electron value g_e, spin-orbit interaction can be considered self-consistently or treated as a perturbation. We chose the spin-orbit perturbation strategy in the scheme proposed by Neese,[5] and implemented in the Gaussian03 code.

3.3 Results and discussion

3.3.1 Experimental aspects

Evaporation of K atoms on the de-hydroxylated MgO surface leads to a blue colored sample characterized by the EPR spectrum shown in Figure 3.1a.

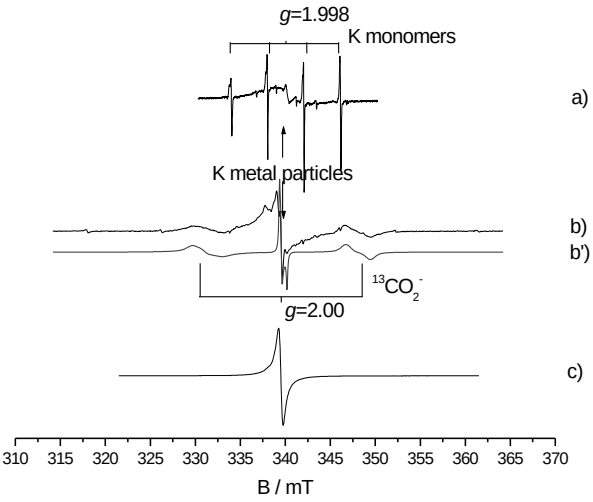

Figure 3.1: EPR spectra of (a) K atoms deposited on the MgO surface; (b) experimental and (b') simulated spectrum of the same sample after exposure to CO_2; (c) spectrum recorded after 24h ageing at room temperature. All spectra were recorded at 77K

The spectrum features a distinct four line hyperfine pattern due to isolated K atoms stabilized on the MgO surface. The spectrum has been analyzed in details in previous works and the reduction of the K hyperfine constant of about 50% with respect to the gas phase value was demonstrated to be due to polarization effects induced by the surface binding site.[6]

Addition of 0.5 mbar of $^{13}CO_2$ at room temperature leads to a bleaching of the sample and the spectrum reported in Figure 3.1b is observed. Reaction with CO_2 leads to the disappearing of the quartet K hyperfine pattern and a new broad signal emerges in the wings of the spectrum. The two lines are separated of about 170 G and are characteristic of the ^{13}C hyperfine coupling in the CO_2^- radical ion.
The experimental results can be summarized as follows: a) surface isolated K metal atoms react with CO_2 to form CO_2^- radical ions. b) the CO_2^- radicals are stabilized on the MgO matrix, probably far from the K atoms as no sign of hyperfine interaction could be detected in the spectra; c) the radicals are sufficiently mobile to react and give rise to diamagnetic species.

We performed DFT/B3LYP calculations in order to understand which situations are responsible for the experimental results.

3.3.2 Computational results

3.3.2.1 $LiCO_2$, $NaCO_2$, KCO_2 gas-phase complexes

The structure of MCO_2 complexes has been studied in details to evaluate the accuracy of the theoretical methods in reproducing observable properties, in particular the EPR constants. The most stable structure is, as reported in other studies,[7] the η^2-O,O mode, Figure 3.2.

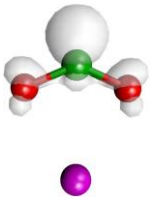

Figure 3.2: Structure of MCO_2 gas-phase complexes. The figure also shows the spin density.

Comparing the results obtained with various methods (B3LYP, UMP2, CCSD) and basis sets, some characteristics are common to all the situations, like the optimal geometry of MCO_2, where the CO_2 molecule is bent, forming an angle of about 130°, Figure 3.2. This is indicative of a charge transfer from the *n*s valence orbital of the alkali atom to the empty antibonding state of the CO_2 molecule. As expected, the distance between the alkali atom and the O ends of the bent CO_2 molecule increases with the atomic size. However, considering the stability of the system, the trend along the series is not regular. This general conclusion does not change also with more sophisticated approaches, like CCSD. In fact, the accurate calculations performed for $LiCO_2$ using flexible basis sets and the UMP2 method give a D_e = 0.52 eV, not too different from that obtained at the CCSD(T) level of theory with the 6-311+G* basis set (0.56 eV). The B3LYP, with a D_e = 0.72 eV slightly overestimates the stability of the molecule. However, the degree of activation of the CO_2 molecule, as determined by the OCO angle and the C-O distance, is incredibly similar in all treatments: α(OCO) is around 128° and r(C-O) is of about 1.25-1.26 Å. Also properties like the vibrational frequencies or the spin distribution are not too different in the different methods. In particular, the spin is largely localized on the C atom and only to a small extent on the Li atom, showing the occurrence of a full electron transfer. The complex can be classified as $Li^+CO_2^-$.

For $NaCO_2$ we found similar trends as for $LiCO_2$, however, most of the calculations show that the complex is metastable. However, also in this case the charge transfer appears.

For KCO_2, only calculations performed with the 6-311+G* basis set are available because the use of large AE basis set for K in connection with the CCSD method causes technical problems. While the complex is bound by 0.21 eV in B3LYP, it is unbound in UMP2 and nearly thermoneutral in CCSD. In general, the complex seems to

be about 0.1 eV more stable than the corresponding sodium complex. The level of activation for these two cases is similar although the results indicate a more pronounced charge transfer in the case of K.

In summary, while $LiCO_2$ is a stable complex, $NaCO_2$ and KCO_2 are metastable or very weakly bound molecules which can be experimentally observed only under special conditions like in rare-gas matrix and at very low temperature.

The performance of the various methods and basis sets in reproducing the hyperfine coupling constants and the g-tensor for the three MCO_2 free molecules are compared to the experimental data referred to matrix isolated molecules (not available for KCO_2).[8] $LiCO_2$ exhibits a large value of a_{iso}(C), 176.2 G in B3LYP, to be compared with the experimental value of 183.5 G. The other methods provide similar values, with HF giving the largest a_{iso}, sign that it gives a stronger localization of the unpaired electron on the C atom. The dipolar part for C is also in excellent agreement with the experiment, in particular for the B3LYP and the UMP2 calculations. Thus, with all the approaches we found a very similar structure of the hyperfine coupling with the O atoms of the CO_2 molecule. The hyperfine interaction with ^{7}Li is also well reproduced: a_{iso} is between 13 and 25 G, depending on the method, with the experimental value being 15.4 G; the components of the B tensor are very small, of the order of 1 G. These results show that the unpaired electron, to large extent, has been transferred to the CO_2 unit.

The situation for $NaCO_2$ is in general similar to that of $LiCO_2$, but with stronger variations depending on the method used. This can be due to the very weak Na-CO_2 interaction which results in slightly different geometrical parameters. These differences immediately reflect in the values of the hfcc's, in particular for the isotropic part. In fact, the dipolar part is always very well reproduced, in quantitative agreement with the experiment.

Finally, for KCO_2 HF gives the largest a_{iso}(C) = 174.8 G and the smallest a_{iso}(K) = 5.6 G; B3LYP the smallest a_{iso}(C) = 151.3 G and the largest a_{iso}(K) = 17.7 G; UMP2 is in between. The low coupling with the alkali metal is thus confirmed.
So, on the basis of the experimental data it is possible to state that the hyperfine interactions obtained at the B3LYP level are in good agreement with the experimental ones. Moreover, all the data point to the formation of a CO_2^- radical anion stabilized by the presence of a metal cation in the vicinity.

The agreement between theory and experiment is very satisfactory also for the g-values. In fact all the calculations indicate a similar structure for the g-tensor with g-values of 1.9970, ≈2.0015, ≈2.0035 for all complexes. In particular, for $LiCO_2$ we found g_1 = 1.9973, g_2 = 2.0017, g_3 = 2.0041, to be compared with the experimental values of 1.9967, 2.0008 and 2.0033, respectively. A similar good agreement is found for the other methods and for $NaCO_2$.

3.3.2.2 Interaction of CO_2 with K atoms adsorbed on the MgO surface

We studied the EPR, geometrical and energetic properties of KCO_2 species adsorbed on suitable MgO morphological defects. The most abundant line defects which are present on the surface of a polycrystalline MgO sample are extended defects like steps and edges where Mg and O atoms are four-coordinated (4c). Our calculations show, in line with what reported in a previous study,[6] that K is bound to a O_{4c} ion with D_e = 0.50 eV, and that the spin is entirely localized on the K atom which thus remains atomic like. No charge transfer occurs from the 4s orbital to the surface. This effect is not due to the alkali nature of the metal, because the same behavior has been shown for Au atoms[9] adsorbed on the MgO surface. This

is in contrast with what happens adsorbing an Ag atom on CeO_2, that show a reducible nature (see Chapter 7).

The computed reduction of the a_{iso}(K) from 83.9 G (free atom) to 56.4 G on the edge is the result of the polarization of the 4s electron away from the surface, an effect which is common to all adsorption sites even in absence of a charge transfer.[6] The dipolar part of the hyperfine constant is negligible (< 1 G), indicating the strongly isotropic nature of the unpaired electron. A residual spin density is found on the O_{4c} ion where K is bound, which results in a_{iso}(O) = 16.0 G.

When CO_2 interacts with the K atom on an edge site a KCO_2 gas-phase complex forms, Figure 3.3a and 3.3b.

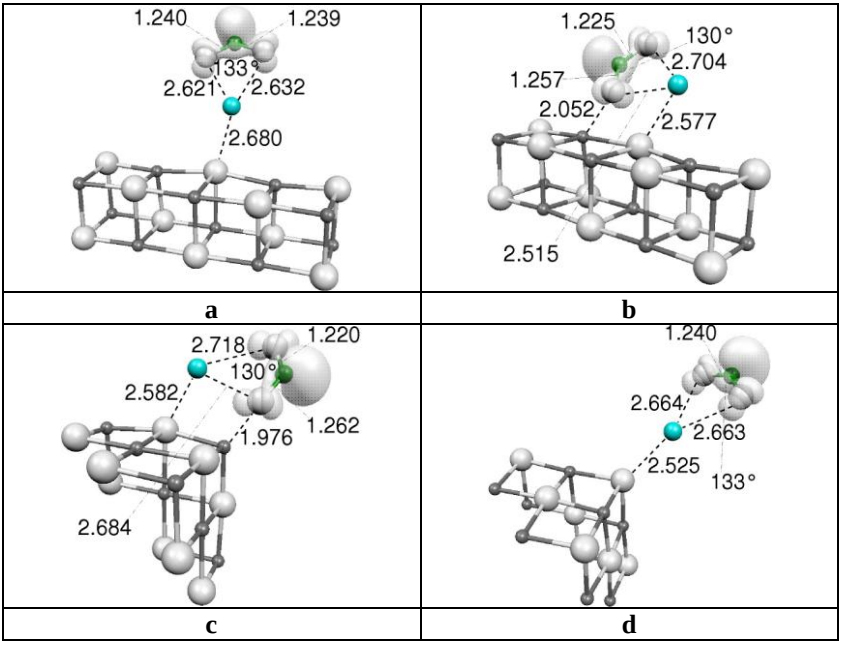

a **b**

c **d**

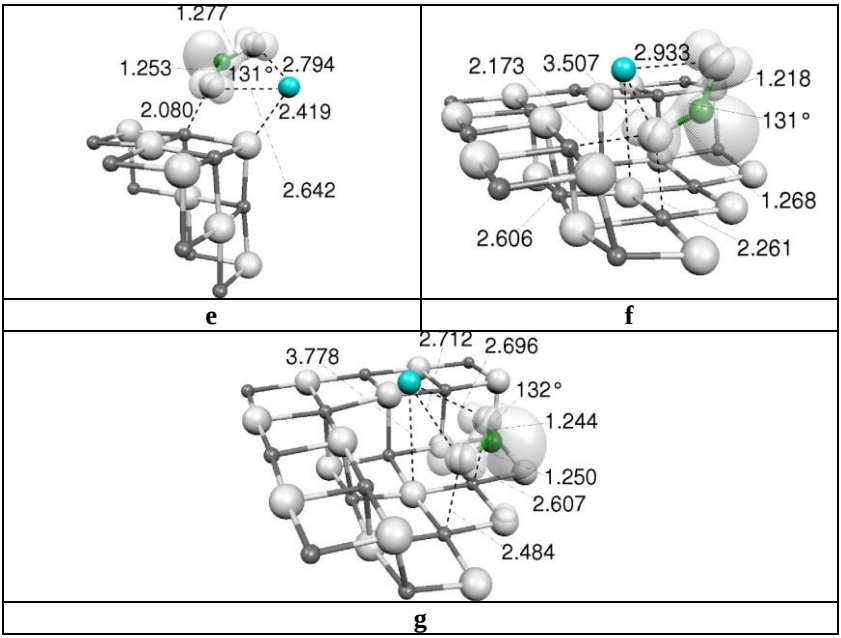

Figure 3.3: KCO_2 species formed at (a) edge (end-on), (b) edge (side-on), (c) cationic corner, (d) anionic corner (end-on), (e) anionic corner (side-on), (f) and (g) cationic reverse corner. White spheres: O; gray spheres: Mg; green sphere: C; blue sphere: K. The grey contour show the spin density distribution.

Two isomers are found, one less stable where the CO_2 unit does not interact with the MgO support (end-on configuration, Figure 3.3a) and one where the O atom of the CO_2 unit can interact with the surface, Figure 3.3b. This second situation is considerably more stable because of the electrostatic interaction between the O-end of the CO_2^- molecule and the exposed Mg_{4c} cation of the edge. The distortion induced in the KCO_2 complex by this additional interaction is small: the two C-O distances differ by 0.03 Å only. Both complexes are stable, in fact the end-on form is bound with respect to dissociation into MgO/K and CO_2 by 0.44 eV, while the

side-on form, the most stable one, has a binding of 0.93 eV. This shows that CO_2 reacts spontaneously with the MgO surface precovered with K atoms, in line with the experimental observation, and that KCO_2, nearly unbound in the gas phase, is stabilized. The degree of activation of the CO_2 molecule is similar in gas-phase and on the surface: the OCO angle is 133° for the end-on form and 130° for the side-on (Figure 3.3).

		D_e,eV	spin population				g_1	g_2	g_3
			K	C	O_a [(a)]	O_b [(a)]			
Edge	End-on	0.44	0.07	0.73	0.10	0.10	1.99658	2.00158	2.00166
Edge	Side-on	0.93	0.02	0.78	0.14	0.07	1.99645	2.00161	2.00230
Cationic corner	Side-on	1.40	0.02	0.79	0.15	0.06	1.99655	2.00164	2.00221
Anionic corner	End-on	0.48	0.07	0.74	0.10	0.10	1.99647	2.00151	2.00166
Anionic corner	Side-on	0.95	0.02	0.79	0.13	0.08	1.99644	2.00156	2.00236
Reverse corner	Side-on	1.62	0.01	0.79	0.16	0.06	1.99659	2.00147	2.00304
Reverse corner	Flat	1.18	–0.01	0.72	0.13	0.13	1.99642	2.00149	2.00309
MgO exp. [(b)]	-	-	-	-	-	-	1.996	2.000	2.002

Table 3.1: Binding energy, spin population and g-tensor for KCO_2 complexes formed on various MgO sites. (a) O_a is the atom of the CO_2 molecule less coordinated, pointing towards the vacuum. (b) The g-tensor in MgO/K/CO_2 complexes is not fully resolved but is very close to that measured for MgO(H^+)(CO_2^-) centers.[10,11]

In both cases the charge transfer from K to CO_2 is almost complete, as shown by the spin population analysis which indicates a tiny spin population on K, Table 3.1, and by the analysis of the hyperfine coupling constants, Table 3.2. In fact the a_{iso}(K) for the most stable

end-on form is 6.7 G only, while it was 56 G before CO_2 adsorption. The dipolar part on K is nearly zero, while the hfcc's with C and O atoms are rather similar to those determined for the gas-phase complex.

	a_{iso}	B_1	B_2	B_3
Edge – end-on				
^{39}**K**	11.8	-0.3	-0.2	0.5
^{17}**O**	-35.9	11.3	9.2	-20.4
^{13}**C**	144.0	-15.5	-13.2	28.7
^{17}**O**	-36.2	11.2	9.1	-20.3
Edge – side-on				
^{39}**K**	6.7	-0.2	-0.2	0.4
^{17}**O**	-33.1	10.8	9.2	-20.0
^{13}**C**	164.4	-16.8	-14.2	31.0
^{17}**O**	-30.7	13.1	10.4	-23.4
Cationic corner – side-on				
^{39}**K**	5.7	-0.2	-0.2	0.4
^{17}**O**	-41.4	10.0	8.3	-18.3
^{13}**C**	178.9	-17.3	-14.5	31.8
^{17}**O**	-30.5	13.3	10.4	-23.8
Anionic corner – end-on				
^{39}**K**	9.8	-0.3	-0.3	0.6
^{17}**O**	-35.8	11.4	9.3	-20.8
^{13}**C**	140.6	-15.4	-13.1	28.4
^{17}**O**	-35.8	11.4	9.3	-20.8
Anionic corner – side-on				
^{39}**K**	5.4	-0.2	-0.2	0.4
^{17}**O**	-34.7	11.1	9.5	-20.6
^{13}**C**	158.0	-16.4	-13.9	30.3
^{17}**O**	-31.6	12.8	10.2	-23.0
Cationic reverse corner – side-on				
^{39}**K**	3.3	-0.2	-0.2	0.4
^{17}**O**	-29.0	10.0	8.7	-18.7
^{13}**C**	160.9	-16.7	-14.2	30.9
^{17}**O**	-27.7	14.2	11.4	-25.6
Cationic reverse corner – flat				
^{39}**K**	2.8	-0.2	-0.1	0.3
^{17}**O**	-32.4	11.7	9.9	-21.6
^{13}**C**	167.7	-16.2	-14.0	30.1
^{17}**O**	-31.4	11.8	9.9	-21.7

Table 3.2: Hyperfine coupling constants (in G) for KCO_2 complexes formed on various sites of the MgO surface

These general features are found in all the other $MgO/K/CO_2$ complexes examined, and only the details of the structure and the stability of the complex differ to some extent.

If the K atom is situated in the vicinity of a cationic corner, terminating with a Mg_{3c} ion, Figure 3.3c, the situation is almost exactly that described above for an edge. The K atom in fact sits on the O_{4c} ion adjacent to the Mg_{3c}, and when CO_2 is added one finds a tilted end-on KCO_2 complex. This complex is very similar to that formed on an edge, Figure 3.3b, with the difference that one of the O atoms of the CO_2 unit is bound to an exposed Mg_{3c}. This has the following consequences: the adsorption energy is considerably higher, 1.40 eV, the asymmetry in the CO_2 unit is increased as shown by the C-O distances of 1.22 and 1.26 Å, the Mg_{3c}-O-CO distance is significantly reduced, 1.976 Å. This asymmetry in the bonding is reflected in the isotropic hyperfine constants of the O atoms of the CO_2 unit which differ now by about 10 G, Table 3.2. The $a_{iso}(K)$ is about 6 G, as on the edge site.

Also on an anionic corner, where the K atom is bound to an O_{3c} ion, the situation is almost exactly that found for the edge site. In fact, also in this case we have two isomers, the less stable end-on, Figure 3.3d, bound by 0.48 eV, and the more stable side-on, bound by 0.95 eV, Figure 3.3e. The structure of the KCO_2 complex as well as the EPR properties are virtually the same computed for the edge, Table 3.2.

The last morphological defect considered is the cationic reverse corner (CRC). This site is particularly important since both theory and experiment have shown that it is the most likely candidate for the K atomic species observed after evaporation of the alkali metal on polycrystalline MgO.[6] The properties of the adsorbed K

atom on the CRC are those described in ref. 6: the atom is bound by 1.16 eV, the spin is almost entirely on K with residuals on the neighboring Mg and O atoms, and the computed a_{iso}(K) is 30.3 G is strongly reduced with respect to the free atom and in line with what measured (40 G).[6] As expected, carbon dioxide reacts with the adsorbed K atom on a CRC forming a stable complex. Two isomers are found: one bound by 1.48 eV, and the other bound by 1.18 eV, Table 3.1 and Figure 3.3f and 3.3g, respectively. In the most stable isomer the molecule is bound end-on to one of the edges of the CRC, Figure 3.3f. Due to the asymmetric interaction, the two C-O and K-O distances are significantly different: r(C-O) are 1.268 and 1.218 Å, and r(K-O) 2.606 and 2.933 Å. The spin is largely localized on the C atom which has an a_{iso} of 160.9 G, a value that is quite similar to the experimental estimate of ≈170 G. Almost no residual spin is found on K which has an a_{iso} = 3.3 G. In the other isomer, the bent CO_2 molecule interacts with both O-ends with the Mg_{5c} ions of the basal MgO plane, Figure 3.3g, giving rise to a slightly distorted complex. Once again, the hfcc's for the two O atoms of the CO_2 unit are almost the same, Table 3.2.

Finally, the g-values (Table 3.1), are very similar for all the considered sites, indicating that it is hard to deduce the adsorption site responsible of the EPR signal from this property. Moreover, the values are also very similar to those of the gas-phase KCO_2 complex, showing that the electronic structure of the molecule is only weakly perturbed by the interaction with the oxide substrate.

3.4 Conclusions

The interaction of CO_2 with a polycrystalline MgO surface where K atoms have been preadsorbed has been investigated with a combined use of EPR spectroscopy and quantum-mechanical

calculations. The experiments show that the isolated K atoms on the MgO surface react with the CO_2 molecules to form CO_2^- radicals. The quantum chemical calculations were used to identify and characterize the sites where the process occurs more favorably.

We have also considered the series of MCO_2 gas-phase complexes (M = Li, Na, K) to validate the computational approach used in determining stability, structure, and EPR properties of these systems. We found that in all the cases the formed species can be described as $M^+CO_2^-$, with one electron transferred from the alkali metal to the CO_2 unit. However, in gas-phase only the Li complex exhibits an appreciable stability, being the $NaCO_2$ and KCO_2 molecules metastable or weakly stable.

Things are different when the interaction between K and CO_2 is mediated by the MgO surface. Here the K atoms are stabilized at specific sites (e.g. the cationic reverse corner), and the K 4s electron is strongly polarized away from the surface so that its ionization potential is considerably lowered.[6] Carbon dioxide interacts with these K atoms to form stable $K^+CO_2^-$ complexes. On a cationic reverse corner CO_2 is bound by ≈1.5 eV. In this conformation the isotropic hyperfine coupling constant with the C atom is 161 G, in good agreement with the measured one, ≈167 G. In the experiment, however, no superhyperfine coupling is observed with the K nucleus, while the calculations suggest a very small coupling of about 3 G. Two possible explanations can be proposed for this result: (1) the hyperfine with K is too small to be resolved in the EPR experiment or (2) the CO_2^- unit is able to diffuse and migrate on other sites under experimental conditions. In this second case, the experiment is examining different species (adsorbed CO_2^- radicals) than the calculations (K-CO_2^- complexes). An indication in favor of the second hypothesis is that the intensity of the CO_2^- signal in the EPR spectra decreases when the sample is kept at room temperature for

one day. At this temperature the thermal energy is probably sufficient to induce diffusion of the CO_2^- anions on the surface. Previous calculations[11] have shown that indeed CO_2^- radicals can diffuse along step edges of the MgO surface.

The result of this chapter have been reported in the following publication:

The reactivity of CO_2 with K atoms adsorbed on MgO powders. Preda G., Pacchioni G., Chiesa M. et al., *Phys. Chem. Chem. Phys.*, 11, (**2009**), 8156.

3.5 Bibliography

[1] P. V. Sushko, A. L. Shluger, C. R. A. Catlow, *Surf. Sci.* 450 (**2000**) 153.
[2] M. J. Frisch, et al., GAUSSIAN03, Revision A.7, Gaussian Inc., Pittsburgh, PA, (**2003**).
[3] R. N. Compton, P. W. Reinhardt, C. D. Cooper, *J. Chem. Phys.* 63 (**1975**) 3821.
[4] M. Brustolon, E. Giamello (Eds.) *Electron Paramagnetic Resonance*, John Wiley & Sons, Hoboken, (**2009**).
[5] F. Neese, *J. Chem. Phys.* 115 (**2001**) 11080.
[6] M. Chiesa, E. Giamello, C. Di Valentin, G. Pacchioni, Z. Sojka, S. Van Doorsiaer, *J. Am. Chem. Soc*. 127 (**2005**) 16935.
[7] H. Tachikawa, Y. Takatori, A. Ohtake, J. Kumagai, H. Yoshida, *J. Mol. Struct. (Theochem)*, 342 (**1995**) 1.
[8] R. Köppe, P. H. Kasai, *J. Phys. Chem.* 98 (**1994**) 11331.
[9] M. Yulikov, M. Sterrer, M. Heyde, H.-P. Rust, T. Risse, H. J. Freund, G. Pacchioni, A. Scagnelli, *Phys. Rev. Lett.* 96 **(2006**) 146804.
[10] M. Chiesa, E. Giamello, *Chem. Eur. J.* 13 (**2007**) 1261.
[11] G. Preda, G. Pacchioni, M. Chiesa, E. Giamello, *J. Phys. Chem. C*, 112 (**2008**) 19568.

Chapter 4

Formation of O_2^- species on Na/MgO powders

4.1 Summary

In this chapter the formation of O_2^- radical anions by contact of O_2 molecules with a Na pre-covered MgO surface is studied experimentally and theoretically. This system is a good model to validate the theoretical approach in reproducing the EPR properties of superoxide species, that is used in Chapter 6. In fact, here theoretical results can be compared with very well resolved EPR spectra provided by the group of Prof. Giamello of the Università di Torino.

Na atoms, deposited on polycrystalline MgO samples are brought into contact with O_2. The typical EPR signal of isolated Na atoms disappears when new paramagnetic species are observed, which are attributed to different surface stabilized O_2^- radicals. HYSCORE spectroscopy allows to determine the superhyperfine interaction tensor of $O_2^-Na^+$ species demonstrating the direct coordination of the O_2^- adsorbate to surface Na^+ cations. DFT calculations enable us to determine the structural details of the formed species. Comparison is set to the case of matrix isolated alkali superoxides, revealing important and unexpected contributions of the MgO matrix in determining the electronic structure of the surface stabilized Na^+-O_2^- complexes.

4.2 Computational details

The properties of NaO_2 complexes formed at the MgO surface have been studied by means of embedded cluster models and DFT calculations using the B3LYP hybrid functional, see Sec. 2.3. In order to properly account for the formation of strong dipoles on the surface, resulting from the internal charge transfer in the $Na^+O_2^-$ units, we take into account the electronic relaxation of the substrate in a wide region. This is based on the shell-model approach and the MgO surface is described by a nanocluster of about 5000 atoms, the same approach reported in Chapter 3. The same GUESS code[1] interfaced with the Gaussian03 code[2] is used for the calculations of this chapter too.
The following QM clusters have been considered to model edge, terrace, reverse corner and reverse edge sites, respectively:

- $Mg_{10}O_{10}Mg^*_{14}$ (edge)
- $Mg_{26}O_{14}Mg^*_{4}$ (terrace)
- $Mg_{17}O_{17}Mg^*_{22}$ (reverse corner)
- $Mg_{26}O_{26}Mg^*_{34}$ (reverse edge)

The basis sets used are 6-31G on Mg, 6-31G* on the O atoms of MgO, and for Na and the O_2 molecule we used 6-311+G* basis set (geometry optimization) and EPR-II basis set (computation of EPR parameters).
As well as in Chapter 3, the hyperfine interactions of the electron spin with the nuclear spin of the ^{23}Na and ^{17}O nuclides have been determined. The hyperfine spin-hamiltonian, $H_{hfc} = \mathbf{S} \cdot \mathbf{A} \cdot \mathbf{I}$, is given in terms of the hyperfine matrix **A** which describes the coupling of the electron with the nuclear spin.[3] **A** can be represented as the

sum of a isotropic (a_{iso}) and a dipolar part T (T is 3x3 traceless matrix).
To quantify the deviations of the g values of NaO_2 complexes from the free electron value g_e, spin-orbit interaction must be either accounted for self-consistently or treated as a perturbation. Here we use the spin-orbit perturbation strategy in the scheme proposed by Neese,[4] and implemented in the code Gaussian03.

4.3 Results and discussion

4.3.1 Experimental aspects

The interaction of alkali metal atoms with dehydrated MgO leads to deeply blue coloured solids. Figure 4.1a shows a representative EPR spectrum obtained by contacting an MgO sample with Na vapours.

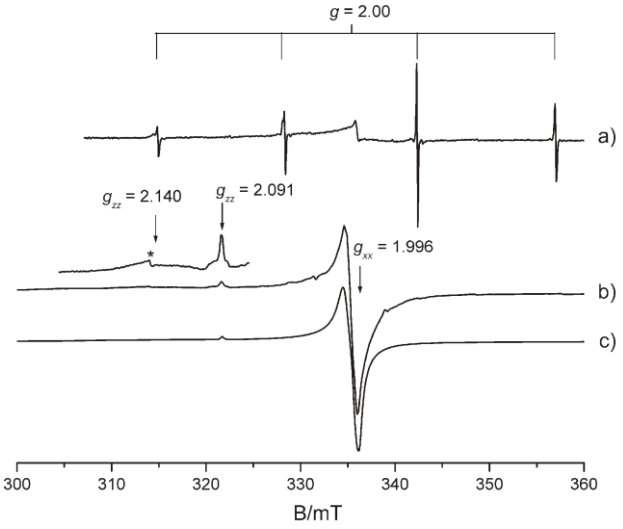

Figure 4.1: a) CW EPR spectra of Na atoms deposited on the Na surface; b) spectrum recorded upon reaction with 1.5 mbar of O_2; c) computer simulation.

The spectrum is dominated by a quartet of lines characteristic of isolated monomeric species. This arises from the hyperfine interaction of the unpaired electron wave function with the sodium nucleus, $I = 3/2$. The nature of this spectrum and the reduction of the Na hyperfine constant with respect to the gas phase value was demonstrated to be due to polarization effects exerted by the surface binding site.[5].

Addition of 1.5 mbar of O_2 at room temperature leads to a bleaching of the sample and the quartet Na hyperfine pattern spectrum is replaced by a new signal shown in Figure 4.1b. This new spectrum is characterized by an orthorhombic powder pattern, characteristic of surface adsorbed superoxide O_2^- species. More detailed analysis of the spectrum via computer simulation (Figure 4.1c) indicates that several species contribute to the spectrum, which can be interpreted as the superposition of different O_2^- ions adsorbed on various surface sites, mainly characterized by different g_{zz} factors (Table 4.1).

	g_{xx}	g_{yy}	g_{zz}	^{23}Na				^{1}H			
				a_{iso}	T_{xx}	T_{yy}	T_{zz}	a_{iso}	T_{xx}	T_{yy}	T_{zz}
O_2^- /HMgO	2.008	2.002	2.0910± 0.002					-5.0 ±0.5	-9.8 ±0.1	+19.6 ±0.1	-9.8 ±0.1
O_2^- /NaMgO	2.008	2.002	2.14± 0.04	-15.0 ±2	-0.1 ±0.5	+3.1 ±0.5	-3.0 ±0.5				
NaO_2 [(a)]	2.0075	2.0022	2.1106	-9.1	-1.5	+3.0	-1.5				

Table 4.1: Spin Hamiltonian parameters of the various O_2^- species deduced from the simulation of CW and HYSCORE spectra. (a) Data taken from ref. [6]

The g matrix is typical for a bound $^2\Pi_{3/2}$ state in which, the local C_{2v} crystal field gives rise to an orthorhombic g-tensor with $g_{zz} >> g_{yy} > g_{xx} \approx g_e$ (where the z direction lies along the internuclear O_2^- axis, while the x direction coincides with the cation-superoxide bond axis). The energy splitting between the π^* orbitals (Δ), is caused by the surface crystal field, which in turn directly depends on the charge of the cation onto which O_2^- is adsorbed. The g_{zz} component can thus be used to determine, in cases where more than one type of cations is present, the nature of the adsorption site.

The low field region (g_{zz}) of the spectrum is characterized by a sharp feature falling at g_{zz} = 2.091, which is easily assigned to "classic" superoxide ions on Mg^{2+}.[7] In particular it has been assigned to radicals stabilized by 5-coordinated cations at MgO (100) terraces and formed upon direct electron transfer from molecular adsorbates.[8,9]

Together with this feature a very broad band is observed in the experimental spectrum centred at lower field values at about $g_{zz} \cong 2.14$. This is typical of superoxide anions stabilized on monovalent cations and in line with g values observed for matrix isolated alkali metals superoxide.[6] The broad line-width which characterizes the spectrum is indicative of a relatively large distribution of values (strains) due to slightly different local environments probed by the adsorbed superoxide on different surface sites. Unresolved hyperfine interactions due to a small delocalization of the unpaired electron spin density on Na nuclei, will also contribute to broaden the spectral line width. This indicates that the superoxide species characterized by the g_{zz} = 2.14 component can be assigned to a surface O_2^--Na^+ adduct. The small hyperfine interactions can be resolved by means of ESEEM (Electron Spin Echo Envelope Modulation) experiments. In particular HYSCORE experiments allowed to determine the full ^{23}Na hyperfine coupling tensor (Table 4.2) .

HYSCORE is a two dimensional ESEEM spectroscopic technique where a mixing π pulse creates correlation of nuclear frequencies in one electron spin (m_S) manifold to nuclear frequencies in the other manifold, allowing to unravel weak hyperfine and nuclear quadrupole couplings.
The HYSCORE spectrum taken at observer position B_0 = 346.3 mT (corresponding to the dashed arrow in Figure 4.1b) is reported in Figure 4.2a.

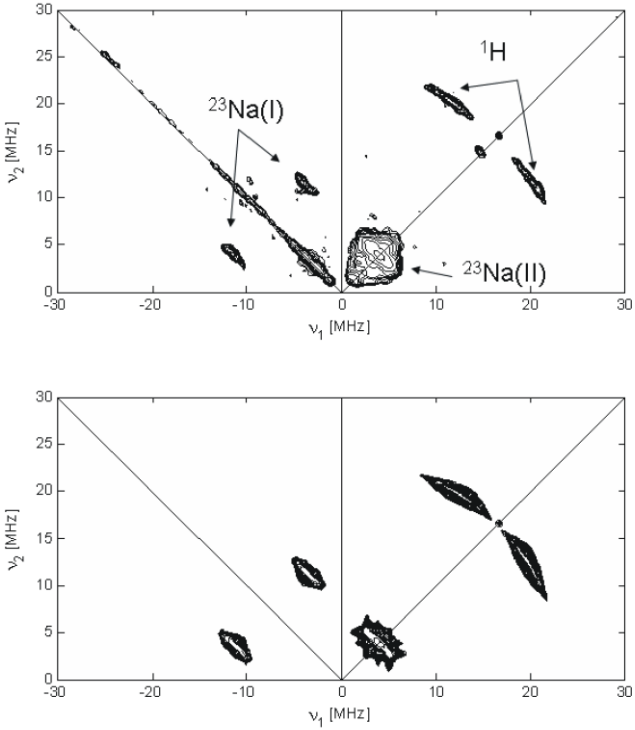

Figure 4.2: a) experimental and b) simulated HYSCORE spectra of O_2^- species on Na/MgO. Spectra recorded at 10K.

This magnetic field setting corresponds to the g_x/g_y position of the superoxide anion. Similar spectra were obtained at field positions spanning the g_x/g_y spectral region (i.e. 330-340 mT in Figure 4.1b).

Based on the experimental results we can propose a general model for the reaction of O_2 with Na adsorbed atoms on MgO. The result of Na evaporation on MgO is schematically resumed in Scheme 4.1a, where the three main paramagnetic species detected by CW-EPR, namely, Na adsorbed atoms, $(H^+)(e^-)$ centres and small sodium metal particles are indicated.

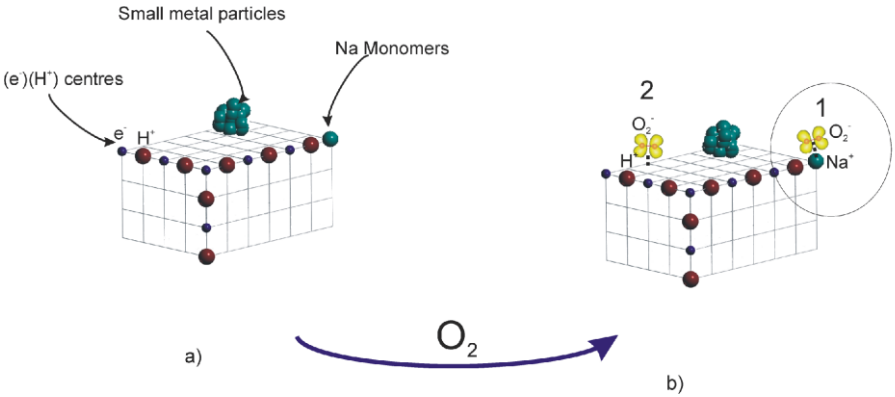

Scheme 4.1: Schematic representation of a) paramagnetic species formed upon sodium evaporation on MgO; b) the two main families of O_2^- formed upon reaction of O_2. In the circle is highlighted the dominant species.

Superoxide ions are formed by electron transfer at the expenses of the above mentioned species. A fraction of the radical ions is stabilized on the resulting Na^+ cations (labeled as 1 in Scheme 4.1b) leading to EPR spectra characterized by high g_{zz} factors and relatively large ^{23}Na hyperfine interactions. A second family of O_2^- radicals is stabilized on Mg^{2+} matrix sites in the proximity of a

surface OH^- group (labelled as 2 in Scheme 4.1b). This second family can arise by direct electron transfer from surface $(H^+)(e^-)$ centres or via a spillover mechanism involving small metal particles.

In the following we will concentrate on the first family of superoxide anion radicals to provide, by means of DFT calculations, a structural assignment for the NaO_2/MgO complexes described above.

4.3.2 Computational results

DFT calculations have been carried out on various models. In particular, we have considered three systems, in order to assess the quality of the computational results and to provide a solid basis for the assignment. Beside various kinds of NaO_2 complexes formed at different sites of the MgO surface, Figure 4.3 and Table 4.2, we have considered the free, gas-phase NaO_2 molecule as well as the properties of O_2^- superoxo species formed at the MgO surface, Figure 4.3 and Table 4.2.

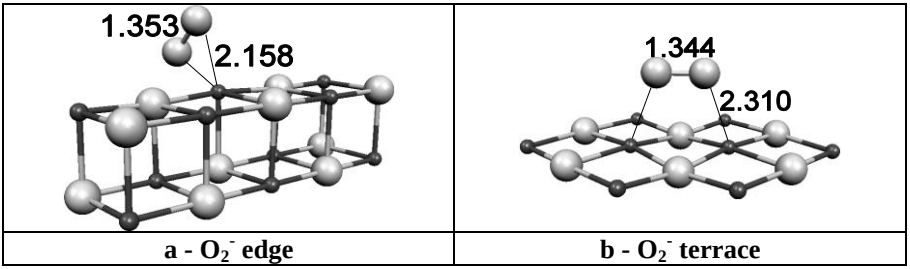

a - O_2^- edge	b - O_2^- terrace

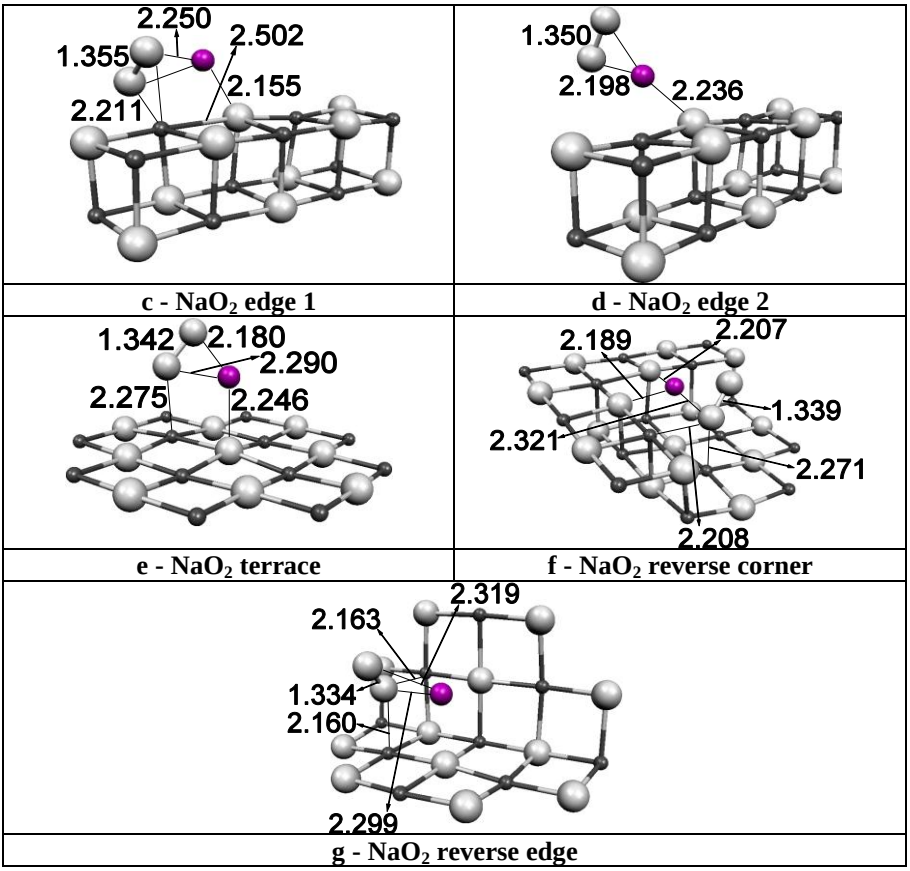

Figure 4.3: (a) and (b) O_2^- species formed at edge and terrace sites, respectively of the MgO surface; NaO_2 species formed at edge (c) and (d), terrace (e), reverse corner (f), reverse edge (g) sites of the MgO surface. White spheres: O; gray spheres: Mg; pink spheres: Na.

For each species the g matrix and the hyperfine coupling constants (both isotropic and dipolar parts) with ^{23}Na and ^{17}O have been calculated and compared with the experimental data.

We started our analysis from the free NaO_2 molecule, keeping in mind that the experiments refer to species isolated in rare gas matrices.[10] The experimental g tensor is characterized by one component, g_{xx} = 2.002, very close to the free electron value, a second component which is only moderately shifted, g_{yy} = 2.006, and a g_{zz} term at 2.110 which exhibits a large shift from the free electron. The calculations reproduce this structure, with the three components of the g tensor at 2.0023, 2.0098, and 2.0740, Table 4.2. However, in absolute terms the g_{zz} component is underestimated by Δg = 0.036. This difference, which is found also for other oxygen species, must be considered when we compare the results for more complex systems. The structure of the ^{23}Na hyperfine coupling constant is reproduced with good accuracy. In particular, the dominant a_{iso} term is well described in the calculations, Table 4.2, and in general the absolute error is of the order of 2 MHz.

				^{17}O (MHz)				^{23}Na (MHz)			
	g_{xx}	g_{yy}	g_{zz}	a_{iso}	T_{xx}	T_{yy}	T_{zz}	a_{iso}	T_{xx}	T_{yy}	T_{zz}
Experiment											
NaO_2 [1]	2.0075	2.0022	2.1106	-	-	-	-	-9.1	-1.5	+3.0	-1.5
O_2^-/MgO E [2]	2.0083	2.0016	2.0770	-56.5	+76.7	-157	+80.6	-	-	-	-
O_2^-/MgO T [3]	2.008	2.002	2.0910	-	-	-	-	-	-	-	-
NaO_2/MgO	2.00	2.00	2.14	-	-	-	-	-15.0	-0.1	+3.1	-3.0
Theory											
NaO_2 [6a]	2.0098	2.0023	2.0740	-29.7	82.3	-168.7	86.4	-11.5	-1.8	3.7	-1.9
O_2^-/MgO E Fig. 3a [4][6b]	2.0096	2.0021	2.0527	-37.9	80.2	-163.4	83.2	-	-	-	-
O_2^-/MgO T Fig. 3b [4][6b]	2.0092	2.0022	2.0639	-39.2	78.7	-160.3	81.8	-	-	-	-
NaO_2/MgO E1 Fig. 3c [6b]	2.0104	2.0021	2.0893	-39.0	79.4	-161.5	82.1	-20.0	-0.3	3.5	-3.2
NaO_2/MgO E2 Fig. 3d [6a]	2.0094	2.0021	2.0721	-38.1	79.6	-163.4	83.5	-8.7	-1.7	3.4	-1.7
NaO_2/MgO T Fig. 3e [5][6a]	2.0092	2.0021	2.0866	-37.2	74.2	-151.6	77.4	-10.7	-0.8	2.7	-1.9
				-37.9	83.7	-171.0	87.4				
NaO_2/MgO RC Fig. 3f [5][6b]	2.0094	2.0021	2.1030	-38.6	69.5	-141.8	72.2	-13.9	-0.2	2.2	-2.0
				-39.8	87.5	-177.6	90.1				
NaO_2/MgO RE Fig.3g [5][6b]	2.0096	2.0021	2.1650	-41.7	72.2	-146.7	74.4	-15.0	-0.4	3.0	-2.6
				-40.2	83.8	-170.7	86.9				

Table 4.2: Computed EPR parameters for O_2^- and NaO_2 complexes formed at the surface of MgO (hyperfine coupling constants in MHz). E = edge, T = terrace, RC = reverse corner, RE = reverse edge. (1) From Ref. 10. (2) From Ref. 11. (3) From Ref. 12. (4) The calculations have been performed without inclusion of the long range polarization (shell-model). 5) The two O atoms of the O_2^- molecule are non-equivalent. The first line refers to the O atom at direct contact with the MgO surface. 6) The reference coordinate system for the **g** and **T** tensors is the following: the z-axis is the internuclear O-O axis; the xz plane is the M(O-O) plane; the *y*-axis is perpendicular to the *xz* plane. The unpaired electron is in the π^*_y orbital. In the case where two interacting M atoms exist (Na or a surface Mg) the relevant M is specified: a) Na and b) Mg.

As a second term of comparison we considered O_2^- superoxo ions stabilized on the edge and terrace sites of the clean MgO surface, Figure 4.3a and 4.3b. In the experiment, the structure of the g matrix is similar as in NaO_2 with a small g_{yy} component slightly reduced compared to g_e, one component, g_{xx}, slightly increased, and a third term which is considerably shifted to higher values. This last term is particularly important because, as discussed previously, it is very sensitive to the site or to the charge of the cation where O_2^- is adsorbed. Typical experimental g_{zz} values for O_2^- adsorbed on MgO are 2.077 and 2.091,[11] and have been assigned to O_2^- adsorbed on edge or terrace sites, respectively.[8,9,12] Notice that both these values are smaller than the g_{zz} component in NaO_2 (2.110). In the present calculations, O_2^- adsorbed on an edge or a terrace site of MgO is characterized by g_{zz} = 2.0525 and g_{zz} = 2.0639, respectively, Table 4.2. As for the NaO_2 case, the absolute values are underestimated compared to the experiment. However, the difference between edge and terrace, Δg = 0.011, is similar as in the experiment, Δg = 0.014. Even more important, the g_{zz} values for O_2^-/MgO are smaller than those computed for NaO_2, in line with the experiment.

The hyperfine constants for ^{17}O in O_2^-/MgO are known experimentally, see Table 4.2. The calculations show that this property is not very dependent on the adsorption site, being essentially related to the spin distribution in the O_2^- unit. While the dipolar part of the tensor is reproduced quantitatively, with errors of less than 2%, the isotropic part is reproduced only qualitatively, with an error of about 30%, Table 4.2. Thus, we can conclude that in general the calculations provide a satisfactory description of the known systems containing the superoxo species, the NaO_2 molecular unit on one side and the O_2^-/MgO surface complexes on the other. The comparison with experiment provides a benchmark of the accuracy of the calculations. With this information we can now consider explicitly models of NaO_2 complexes formed at the MgO surface.

We have studied a large number of possible structures formed at various sites. We will only discuss those structures which are relevant in terms of stability or of consistency with the experimental data. A first consideration is related to the fact that the experiment is performed by dosing O_2 on a Na pre-covered MgO surface. In an initial stage, therefore, one can reasonably assume that the NaO_2 complexes will form at the surface sites where Na atoms are preferentially stabilized. This aspect has been investigated in detail in the past.[13] While a definitive conclusion on the preferred adsorption sites is not possible, there is evidence that among the most likely adsorption sites for Na are the edges, the reverse corners and the reverse edges. The corresponding stabilities of the Na atoms are 0.69 eV (edge), 0.59 eV (reverse edge), 0.79 eV (cationic reverse corner) and 1.49 eV (anionic reverse corner).[13] For this reason we start the discussion from NaO_2 formed on an edge site, Figure 4.3c. The Na atom is interacting with an O ion of the surface at a distance of about 2.2 Å. In this position the 3s valence electron is still

associated to the Na atom, the atom is thus "neutral", but is strongly polarized.[13] The O_2 molecule has been placed at bonding distance from this atom starting the geometry optimization from various orientations (mono-dentate, bidentate, parallel, linear, bent, etc.). In all cases a net charge transfer occurs spontaneously with formation of a $Na^+O_2^-$ complex. The energy gain is rather large, 2.31 eV in the most stable structure, Figure 4.3c and Table 4.3.

NaO_2/MgO: adsorption site	**E_a (O_2), eV [(a)]**	**E_a (NaO_2) [(b)]**
Edge 1 (Fig. 4.3c)	2.31	3.01
Edge2 (Fig. 4.3d)	1.92	2.62
Terrace (Fig. 4.3e)	2.19	1.12
Reverse corner (Fig. 4.3f)	3.01	2.69
Reverse edge (Fig. 4.3g)	2.74	3.53

Table 4.3: Adsorption energy, E_a, of O_2 molecules on Na/MgO and of NaO_2 molecules on MgO. (a) Defined as $E(NaO_2/MgO) - E(Na/MgO) - E(O_2)$. (b) Defined as $E(NaO_2/MgO) - E(MgO) - E(NaO_2)$.

Here the O_2 molecule is interacting simultaneously with the Na^+ and with a four-coordinated Mg^{2+} of the edge, then the O_2^- unit benefits from the electrostatic interaction with two cations. The O-O bond is perpendicular to the edge, the two O atoms are equivalent and the unpaired electron is localized in a π^* orbital lying in the Na(O-O) plane. In the next stable isomer the O_2 molecule is bound to Na but not to the surface, Figure 4.3d. This structure is 0.4 eV less stable than the ground state isomer, Table 4.3. In this second structure the O_2 molecule is free to rotate around the O-Na axis (the barrier for rotation is only 0.01 eV) and the π^* orbital hosting the unpaired electron is found to be perpendicular to the Na(O-O) plane as in the case of the NaO_2 free molecule.

We consider now the EPR properties of the most stable of the two isomers, Figure 4.3c and Table 4.2. The g-tensor has the

same structure already found for gas-phase NaO_2, with one term close to g_e, g_{yy} = 2.0021, a component slightly shifted, g_{xx} = 2.0104, and a third component which deviates strongly from g_e, g_{zz} = 2.0893. This latter term, in the calculations, is larger than the corresponding theoretical value of free NaO_2, g_{zz} = 2.0740, in full agreement with the experiment where $g_{zz}(NaO_2/MgO)$ is larger than $g_{zz}(NaO_2)$. This is an important result as it demonstrates that the purely ionic model whereby the g_{zz} factor is determined by the local crystal field of the adsorbing ion has to be handled with care. Based on these arguments in fact one would expect the case represented in Figure 4.3c to have a g_{zz} factor smaller than the case of Figure 4.3d, being the O_2^- adsorbed on a Mg^{2+} ion in the first case and on a Na^+ ion in the second. The calculations show that this trend is reversed indicating a non negligible role of covalency in the NaO_2/MgO system. Of course, the absolute values differ significantly, being the calculated g_{zz} for NaO_2/MgO (edge 1), g_{zz} = 2.0893, much smaller than in the experiment, $g_{zz} \cong 2.14$, Table 4.2. However, we have seen above that this is a general systematic error. Therefore, we can conclude that the g-matrix for a NaO_2 complex formed on an edge site of MgO is consistent with the experimental data.

Further support to this assignment comes from the analysis of the ^{23}Na hyperfine coupling constants. These are reproduced in an almost quantitative way for free NaO_2, Table 4.2. On the NaO_2/MgO (edge 1) species, a_{iso} is -20.0 MHz, compared to a_{iso} = -11.5 MHz in NaO_2, increased by about 70%; the dipolar part remains small and almost unchanged. In the experiment, going from matrix isolated NaO_2 to MgO supported NaO_2, a_{iso} goes from -8.9 to -15.6 MHz, with the same relative increase of the computational model. In this case, also the absolute values of the hyperfine constants are reproduced with acceptable errors and in particular the departure from axial symmetry of the T tensor is correctly reproduced. Notice

that if we consider the second stable isomer (Figure 4.3d) the agreement with experiment is much less satisfactory. First of all the g_{zz} value is nearly as in free NaO_2 and not larger, at variance with the experiment, Table 4.2. Second, $a_{iso}(^{23}Na)$ is smaller than in free NaO_2 and not larger and the T tensor displays axial symmetry, again in contradiction with the observations. This shows that the structure of the EPR spectrum is very sensitive to the exact orientation of the NaO_2 surface complex and that the isomer shown in Figure 4.3d is inconsistent both in terms of stability and of EPR properties. Similar complexes where O_2 interacts only with Na and not with the MgO surface, see Figure 4.3d, but formed at other sites like terraces or corners exhibit the same inconsistency, so that in the assignment one can rule out these structures.

As mentioned above, the computed hfcc's for ^{17}O in superoxo O_2^-/MgO species are not very informative on the nature of the adsorption site as they do not change substantially from site to site, Table 4.2. However, the hyperfine tensor orientation provides a clear indication of the π^* orbital hosting the unpaired electron. In some cases, as those in Figure 4.3d and Figure 4.3e, the electron is in the π^* orbital perpendicular to the Na(O-O) plane, in other cases (Figure 4.3c, and Figures 4.3f-4.3g) it is in the π^* orbital perpendicular to the Mg_s(O-O) plane, where Mg_s is the surface Mg ion interacting with the O_2^- species. These latter models are consistent with the experimental observation in terms of both EPR and energetic properties.

Based on the analysis of the full set of EPR parameters, g- and A-tensor, the NaO_2 species formed on an edge site of the MgO surface where O_2 is simultaneously bound to Na and to MgO, Figure 4.3c, symbolizes the structural characteristics of the species responsible for the large g shift and ^{23}Na hyperfine interaction observed in the EPR experiments.

In the rest of the discussion we will briefly present a few selected results for three other sites. As a first case we consider a NaO_2 complex formed at the MgO(100) terrace, Figure 4.3e. Notice that since Na atoms are not stabilized at these sites,[13] this situation can be found only assuming a diffusion process for the NaO_2 units. In the most stable isomer the O_2^- superoxide anion interacts with the Na atom and with a surface Mg^{2+} cation with a binding energy of 2.19 eV, Table 4.3, similar as the edge case. Overall, however, the NaO_2 unit is much more stable on the edge, where it is bound by 3.01 eV, while on the terrace the bonding is only 1.12 eV, Table 4.3. In this configuration, Figure 4.3e, the g-tensor is consistent with the experiment (g_{zz} (NaO_2/MgO) > g_{zz} (NaO_2), Table 4.2) but not the A tensor, in fact a_{iso} is smaller than in free NaO_2 while in the experiment is larger. So, not only the terrace complex, Figure 4.3e, is thermodynamically less favourable than the edge one, but its EPR parameters do not fit with the observation.

Much more interesting from this point of view are the other two cases considered, a Na atom stabilized at reverse corner and reverse edge sites, two of the most strongly binding sites on the MgO surface. On the reverse corner the Na atom interacts with three oxide anions and binds O_2 by 3.01 eV, Table 4.3. The O_2 molecule interacts with both Na and a Mg^{2+} cation of the step, Figure 4.3f, but, due to the local conformation, the two oxygens are non-equivalent. The NaO_2 unit is bound to this site by 2.69 eV, i.e. slightly less than on an edge site, Table 4.3. Among the cases considered the g-tensor exhibits the best agreement with the experiment. In fact, the g_{zz} component, 2.1030, is 0.029 higher than in free NaO_2 (g_{zz} = 2.0740); in the experiment, the difference is of 0.028, see Table 4.2. The $a_{iso}(^{23}Na)$ value, -13.9 MHz, is also higher than in the free molecule, -11.5 MHz, although here the relative change (+20%) is smaller than the measured one (+75%). On the reverse edge, Figure 4.3g, the Na

atom is bound to two O ions of the surface and the NaO_2 unit has similar characteristics as for the other irregular sites, i.e. is strongly bound, 3.53 eV (Table 4.3), and the two O atoms of the O_2^- molecule are no longer equivalent. In this conformation the O_2^- molecule exhibits the highest g_{zz} value computed so far, 2.1650, even higher than in NaO_2, Table 4.2. The coupling with ^{23}Na is similar to that computed for the edge and reverse corner cases, Table 4.2.

In conclusion, the NaO_2 complexes formed at reverse corner and reverse edge sites are also compatible with the experimental data, and it is likely that a family of sites is populated. This is in line with the broad g_{zz} feature centred at about 2.14 observed in the experimental CW-EPR spectrum, which can indeed be explained taking into account a distribution of slightly different surface adsorption sites.

4.4 Conclusions

In a combined EPR (CW-EPR and HYSCORE) and DFT study, the reactivity of O_2 with Na atoms adsorbed on the surface of polycrystalline MgO has been investigated. Direct electron transfer, surface to adsorbate, is observed leading to O_2^- radical anions stabilized at different surface sites. HYSCORE measurements allow to investigate the ligand hyperfine coupling between O_2^- electron spin and ^{23}Na and ^{1}H nuclei present at the MgO surface, proving that a fraction of the formed superoxide is indeed chemically bound to the surface Na^+ ions, while a second fraction is stabilized on the MgO matrix. Comparison with rare gas matrix trapped NaO_2 molecules shows that the MgO stabilized complex is characterized by larger a_{iso} and g_{zz} parameters. The differences between isolated molecular species and surface adsorbed species are rationalized with

the help of DFT calculations. These lend support to the analysis of the HYSCORE data allowing to clarify the structural and electronic characteristics of the NaO_2/MgO complex. In particular, the calculations show that the role of the matrix is instrumental in stabilizing the so formed superoxide, leading to a counterintuitive positive shift of the g_{zz} component. A family of sites is found to be compatible with the observed experimental results, which is characterized by a mutual interaction of the superoxide radical anion with Mg^{2+} matrix ions and surface Na^{+} species. Interestingly, in the case of the surface stabilized NaO_2 complex the unpaired electron is found to be located in a π^* orbital dwelling in the O_2-Na plane, while the reverse occurs for matrix trapped NaO_2 molecules.

Finally it can be concluded that HYSCORE spectroscopy in conjunction with DFT modelling is a powerful tool to explore the structure of superoxide species localized at solid surfaces, allowing to establish specific binding sites and geometrical and electronic structures of surface adsorbed species. In particular, the theoretical approach used to investigate such species is able to reproduce very well the experimental EPR properties.

The result of this chapter have been reported in the following publication:

Formation of superoxo species by interaction of O_2^- with Na atoms deposited on MgO powders: a combined continuous-wave EPR (CW-EPR), hyperfine sublevel correlation (HYSCORE) and DFT study.

Napoli F., Chiesa M., Giamello E., Preda G., Di Valentin C., Pacchioni G., *Chemistry-A European Journal*, 16, (**2010**), 677.

4.5 Bibliography

[1] P. V. Sushko, A. L. Shluger, C. R. A. Catlow, *Surf. Sci.*, 450 (**2000**) 153.
[2] M. J. Frisch, et al., GAUSSIAN03, Revision A.7, Gaussian Inc., Pittsburgh, PA, **2003**.
[3] M. Brustolon, E. Giamello (Eds.) *Electron Paramagnetic Resonance*, John Wiley & Sons, Hoboken, **2009**.
[4] F. Neese, *J. Chem. Phys.* 115 (**2001**) 11080.
[5] M. Chiesa, F. Napoli, E. Giamello, *J. Phys. Chem. C*, 111 (**2007**) 548**.**
[6] D. M. Lindsay, D. R. Herschbach, A. L. Kwiram *Chem. Phys. Lett.* 25 (**1974**) 175.
[7] E. Giamello, P. Ugliengo, E. Garrone, *J. Chem. Soc., Faraday Trans. 1* 85 (**1989**) 1373.
[8] E. Giamello, D. M. Murphy, E. Garrone, A. Zecchina, *Spectr. Acta* 49A (**1993**) 1323.
[9] M. C. Paganini, M. Chiesa, E. Giamello, S. Coluccia, G. Martra, D.M. Murphy, G. Pacchioni, *Surf. Sci.* 421 (**1999**) 246.
[10] D. M. Lindsay, D. R. Herschbach, A. L. Kwiram, Chem. Phys. Lett. 25 (1974) 175.
[11] M. Chiesa, E. Giamello, M. C. Paganini, Z. Sojka, D. M. Murphy, *J. Chem. Phys.*, 116 (**2002**) 4266.
[12] G. Pacchioni, A. M. Ferrari, E. Giamello, *Chem. Phys. Lett.* 255 (**1996**) 58.
[13] E. Finazzi, C. Di Valentin, G. Pacchioni, M. Chiesa, E. Giamello, H. J. Gao, J. C. Lian, T. Risse, H-J. Freund, Chem. Eur. J. 14 (**2008**)
4404.

PART II

Properties of ceria and silver precovered ceria surfaces

Chapter 5

Oxygen active species in Ag-modified CeO_2 catalyst for soot oxidation

5.1 Summary

In this chapter we analyze from a theoretical point of view, some aspects of the reactivity of Ag-modified CeO_2 surfaces used for soot combustion in particulate Diesel filters. O_2 molecules and small carbon clusters adsorbed and coadsorbed on the $CeO_2(111)$ stoichiometric and reduced surface have been considered. Carbonaceous species react with the ceria surface with formation of oxygenated carbon fragments and subsequent formation of reduced ceria but the mechanism which occurs to replenish the oxygen content of the oxide catalyst is still unclear. The formation of peroxo and superoxo species and the role of silver in modifying the properties of $CeO_2(111)$ is discussed. Ag atoms and Ag_5 clusters act as donor species, become oxidized and donate the valence electron to the oxide with formation of reduced Ce^{3+} ions. A charge transfer in the opposite direction occurs when Ag atoms are bound to O vacancies. In this second case we found that in the presence of gas-phase oxygen the formation of peroxo species can be mediated by small Ag particles. Peroxo is found in the vacancy, so the final result is that the cavity is refilled by ambient oxygen.

5.2 Computational details

Spin polarized DFT calculations have been carried out with the VASP program (see Sec. 2.6) using a plane wave basis set and the projector augmented wave (PAW) method to describe the interaction between the valence electrons and the atomic cores. The valence electron density is defined by the twelve ($5s^2 5p^6 6s^2 5d^1 4f^1$) electrons of each Ce atom, the six ($2s^2 2p^4$) electrons of each O atom, and the eleven ($5s^1 4d^{10}$) electrons of Ag. The plane-wave expansion includes all plane waves with kinetic energy smaller than a cutoff of 415 eV. The LDA+U or GGA+U approaches (see Sec. 2.4) were used. The LDA and GGA parts of these functionals are those of Vosko et al.[1] (VWN) and Perdew-Wang[2,3] (PW91), respectively, and we used the formalism of Dudarev et al..[4] Numerical integration in the reciprocal space was carried out using a 2 × 2 × 1 Monkhorst-Pack special *k*-points grid[5]. A Methfessel-Paxton smearing width σ = 0.2 eV was applied to help to converge the electronic density.[6]

Geometry optimization, magnetic moments and Bader charges[7,8] has been performed within the LDA+U with U_{eff} = 5 eV scheme because it provides a lattice parameter which is close to experiment.[9,10] Energies were calculated at the GGA+U level with U_{eff} = 3 eV[10] because this helps to properly describe localization in bulk Ce_2O_3 as well as in ceria nanoparticles containing both Ce^{3+} and Ce^{4+} atoms.

To model the O-terminated CeO_2(111) surface 2 x 2 (Ce_8O_{16}) or 3 x 3 ($Ce_{18}O_{36}$) supercells with 6 layers have been used keeping the three bottom layers fixed and relaxing the uppermost ones. The optimized lattice parameter a_0 is 5.40 Å, in excellent agreement with the experiment $a_0 \approx 5.41$ Å (see Sec. 1.1). The supercell includes a

vacuum of 12 Å which is large enough to avoid interactions between the slabs obtained after replication in the three space dimensions.

5.3 Results and discussion

5.3.1 CeO_2(111) and CeO_{2-x}(111)

The calculated electronic structure of a stoichiometric CeO_2(111) surface (Figure 5.1), as deduced from the corresponding density of states shows that the valence band, about 4 eV wide, is mainly formed by O 2p levels, and is separated by a gap of about 5.1 eV from the conduction band which originates from the Ce 5d orbitals. For comparison, the experimental band gap is 6 eV (see Sec. 1.1).

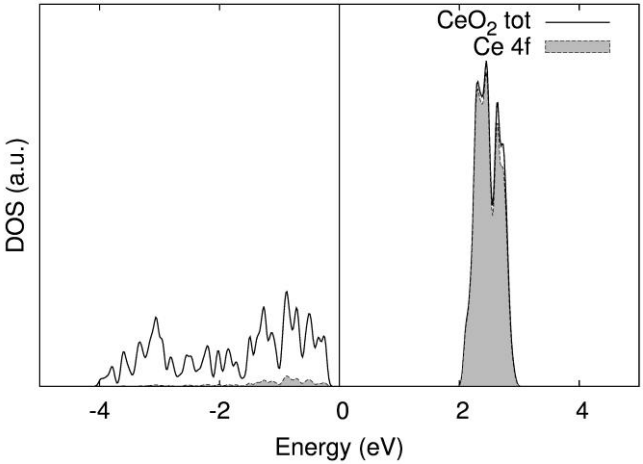

Figure 5.1: DOS of CeO_2(111) clean surface.

In CeO_2 all cerium-centered valence states are empty, but the very localized 4f states lie in the gap at 2.1 eV above the top of the valence band (3 eV the experiment).

The formation of an oxygen vacancy after the removal of a surface oxygen is a relevant process for the catalytic properties of CeO_2. According to our calculations, the vacancy formation energy, computed with respect to ½ O_2, is 3.54 eV (6.62 eV with respect to atomic O). This is in line with other values reported in the literature,[11] also considering the intrinsic difficulty to compute this quantity in reducible oxides.[12] This is an important quantity since it has been proposed that the soot oxidation occurs at the expense of lattice oxygens (see Sec. 1.3).

The removal of one oxygen atom corresponds to a reduction of the system and in fact two electrons are found in localized 4f states on two surface Ce ions which change their configuration from $Ce^{+4}(4f^0)$ to $Ce^{+3}(4f^1)$.[13] This change in atomic configuration is accompanied by the appearance in the energy gap of defect states associated to the localized 4f electrons at about 1.4 eV from the top of the valence band (Figure 5.2). This strong localization is also demonstrated, by a plot of the spin density of the system indicating the presence of an unpaired electron on two specific Ce atoms of the surface, nearest neighbor to the missing oxygen (Figure 5.2).

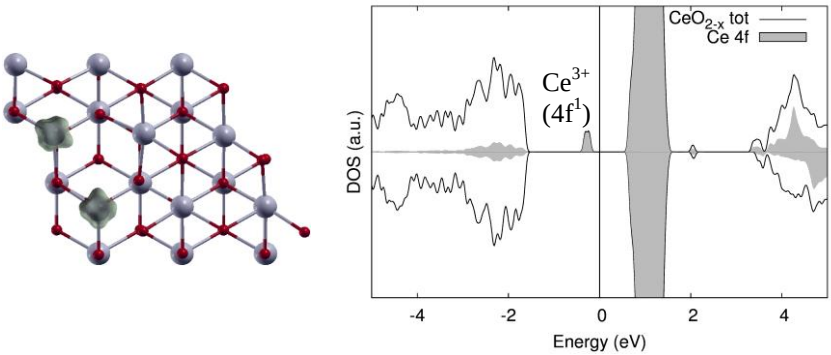

Figure 5.2: Structure of CeO_{2-x}(111). (a) Structure and spin distribution; (b) DOS curves.

All these features are consistent with other studies reported in literature.[9,14,15] The found electronic distribution is not the only one, in fact recent studies have shown that there is a distribution of Ce sites where the localization of the electrons can take place so that multiple structures exist with formally the same electronic configuration but with very similar total energies.[16,17] The existence of several states nearly degenerate in energy suggests a relatively easy electron mobility at finite temperatures, since electron transport in these materials occurs by hopping. The activation energy for polaron electron transport in the bulk is indeed quite low, about 0.4 eV.[18] This may be important in view of the mechanism which is at the basis of the formation of superoxo O_2^- and peroxo O_2^{2-} ions.

5.3.2 O_2 adsorption on CeO_2(111) and CeO_{2-x}(111)

The first step to consider in the catalytic oxidation of soot is the mechanism of interaction of gas-phase oxygen with the ceria surface. In fact, a key step in the proposed oxidation mechanism

consists in the regeneration of the stoichiometry of the ceria particle after lattice oxygens have been transferred to the carbon particles, according to the Mars-van Krevelen mechanism. However, in our calculations, and in agreement with previous studies, the oxygen molecule is just physisorbed on the stoichiometric CeO_2(111) regular surface.[19,20] The adsorption energy, <0.1 eV, is so low that it is possible only at very low temperatures.[21] The O-O distance is the same as in gas-phase, 1.22 Å, so the oxygen molecule is not activated. This means that oxygen can react only with defect sites at the ceria surface, like low-coordinated atoms at step edges, oxygen vacancies, or their aggregates.

Indeed, a completely different situation is found when the O_2 molecule is adsorbed on a O vacancy site. Here the interaction is strong, 3.15 eV, and the molecule is adsorbed with one O atom filling the vacancy and the other pointing out from the surface. The O-O distance is elongated to 1.418 Å, typical of a peroxo group. The O-O axis is tilted and forms an angle of about 50° from the surface normal. While the initial defective surface contains two Ce^{3+} ions (Figure 5.2), the adsorption of an O_2 molecule results in a complete magnetic quenching and the surface complex is diamagnetic. This result, combined with the long O-O bond and the analysis of the Bader charges (-0.71 and -0.53e), points toward the formation of a peroxo group. The energy required to dissociate the peroxo group and release a gas-phase O atom is 2.70 eV (if computed with respect to ½ O_2 the process is slightly exothermic, -0.40 eV). This energy is quite relevant in the context of oxidative processes taking place on the surface, because it is considerably smaller than the energy required to remove an oxygen from a regular site (6.62 eV). Peroxo groups are thus source of more reactive oxygens.

The formation of a peroxo species is in line with what reported by other authors,[19,20,22] and has also been confirmed

experimentally by Raman spectroscopy since typical bands in the 830-870 cm^{-1} region are found[21,23]. Experimentally, also the presence of paramagnetic superoxo O_2^- species has been reported. The proof of the formation of such species comes from EPR spectroscopy[24] but also from the analysis of Raman spectra since a typical band around 1120 cm^{-1} is observed.[21,23]

In principle, O_2^- species could form by O_2 adsorption on regular sites of a reduced CeO_{2-x} surface followed by an electron transfer from one Ce^{3+} $4f^1$ state to the $2\pi^*$ MOs of the adsorbed O_2 molecule. This is indeed the typical process occurring on other reduced oxides like TiO_2 [25,26]. However, computational attempts to adsorbe an O_2 molecule on a *regular site* of CeO_{2-x} resulted only in weak adsorption and no charge transfer. The unpaired electrons remain localized on the Ce^{3+} ions even when these are at the surface. This result suggests that in CeO_2 the 4f levels are deeper in energy then the O_2 $2\pi^*$ levels, so that a charge transfer can only occur when these species are in close contact. We also checked that this conclusion is not due to limitations or assumptions related to the computational approach adopted since, in particular, the 4f levels could be artificially stabilized by the choice of the U parameter. However, the same result has been obtained at the standard GGA-DFT level.

In a recent study Conesa has suggested that superoxo O_2^- species form when O_2 interacts directly with a "single electron" oxygen vacancy[22] obtained by replacing a tetravalent Ce^{4+} ion by a trivalent La^{3+} ion, thus leaving only one Ce^{3+} associated to an O vacancy. In this case only one electron can be transferred to adsorbed O_2 and a superoxo is then formed.

However, there is a more likely explanation for the formation of superoxo anions. In fact, in Chapter 6 we show that O_2^- species can form by direct interaction of molecular oxygen with low-coordinated

Ce ions, present at extended defects of the ceria surface (edge, steps, dislocations, etc.[14]) and on ceria nanoparticles since Ce^{3+} cations tend to be located at low coordinated sites of CeO_{2-x} reduced particles.[27]

In summary, the classical model of an oxygen vacancy at the surface of reduced ceria explains the formation of diamagnetic peroxo groups, while the presence of Ce^{3+} ions at low-coordinated sites can be considered responsible for the formation of superoxo radical species. In both cases the O_2 molecule is activated and easier to dissociate in O atoms which can replenish the oxygen content of the ceria catalyst involved in soot oxidation.

5.3.3 Reactivity of oxygen surface species towards carbon soot

Considering the oxidation of the carbon soot, two hypothesis can be formulated. In the first one the carbon particle interacts directly with a peroxo group with transfer of one O atom:

$$C_n + CeO_{2+x}\,(\text{peroxo}) \rightarrow C_nO_x + CeO_2 \qquad (5.1)$$

The other possibility is that one O atom of the peroxo group diffuses on the surface and reacts with the deposited carbon soot. This second mechanism, as proven theoretically, is possible only at elevated temperatures,[19] usually reached in diesel engines. Thus, at the normal temperature where diesel antiparticulate filters operate, the mobility of surface oxygens is expected to contribute to the oxidation process.

We have estimated the energy changes associated to reaction (5.1) taking an infinite graphene sheet as a simplified model of typical aromatic hydrocarbons present in carbon soot. This leads to

the formation of a graphene oxide where an O atom is bound to a graphene layer. The oxygen atom has been added in a bridge position over two C atoms and we found that the reaction is nearly thermoneutral, with a computed $\Delta E = +0.35$ eV, suggesting that the oxygen atoms of the peroxo group are potential candidates for the process.

If one compares the reactivity of the peroxo groups with that of the regular surface oxide anions of $CeO_2(111)$:

$$C_n + CeO_2 \rightarrow C_nO_x + CeO_{2-x}\,(\text{reduced}) \qquad (5.2)$$

the difference with reaction (5.1) is very clear: reaction (5.2) is endothermic by 4.25 eV, due to the much higher cost of removing an oxygen atom from a regular site of the CeO_2 surface. Of course, not only the thermodynamics but also the kinetics of the process will be strongly affected by the formation of peroxo groups, as the barrier for the reaction is expected to be considerably lower.

Unfortunately, these computational results are not fully compatible with the experimental evidence based on isotopic labeling experiments which show that it is the oxygen coming from the ceria lattice which is incorporated into the oxidized products.[28] Thus, the simplest idea that gas-phase O_2 reacts with defects like oxygen vacancies and generates "active" O species which are transferred to the organic substrate is not consistent with this specific result. This means that the gas-phase O_2 molecule must generate active oxygen species (e.g. via peroxo or superoxo formation) that further diffuse into the bulk or to other surface regions of the oxide in order to regenerate the original oxygen content. However, active oxygen species can directly originate from the interaction of supported carbon particles and the lattice oxygen.

To study the reactivity of ceria with adsorbed carbon species we have considered a C_4 cluster on the surface of $CeO_2(111)$. C_4 is considered in its rhombic ground state structure[29]. The cluster interacts parallel to the surface and a binding energy is 2.02 eV. The interaction leads to an outwards displacement of a surface O atom which forms a direct bond with one of the apical C atoms, Figure 5.3a.

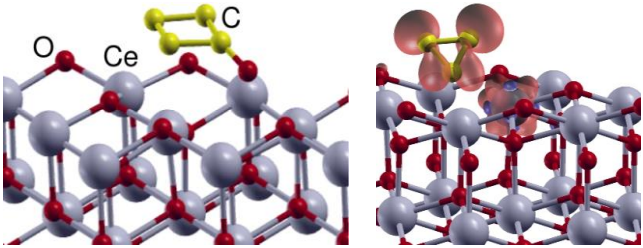

Figure 5.3: (a) Structure of a C_4 cluster adsorbed on the $CeO_2(111)$ surface. (b) Structure of a C_3 cluster adsorbed on the $CeO_{2-x}(111)$ surface resulting from the desorption of a CO molecule. The figure shows also the spin density.

The C-O distance, 1.27 Å, is typical of oxygenated hydrocarbon species. In the final structure, the O atom has been pulled out from the surface by about 0.7 Å, Figure 5.3a, then an O vacancy has been created. This process occurs spontaneously, with no energy barrier, and leads to an oxygenated carbon fragment. The desorption of the C_4O unit, which results in the formation of an O vacancy on the surface, costs 1.03 eV. The other possibility is that what desorbs is a CO molecule, leaving on the surface a C_3 unit bound to an O vacancy according to the reaction:

$$C_4 + CeO_2 \rightarrow C_3/CeO_{2-x}\,(\text{reduced}) + CO \qquad (5.3)$$

For the C_3 cluster adsorbed on an O vacancy of $CeO_2(111)$ we found two isomers almost isoenergetic, both with triangular shape and one of the apical C atoms pointing towards the vacancy, Figure 5.3b. The C_3/CeO_{2-x} complex and CO are only 0.7 eV less stable than the C_4 unit adsorbed on the non-defective surface. This means that in the presence of adsorbed hydrocarbon species, the formation of CO (or CO_2) by means of the surface O atoms of the ceria catalyst is an energetically accessible process.

5.3.4 O_2 adsorption on Ag/CeO_2 catalysts

In a recent paper Machida et al.[30] have reported that loading the ceria catalyst with Ag metal leads to an improved catalytic activity and a lower combustion temperature. This has been tentatively explained with the fact that metallic silver can promote the formation of superoxo species.[31,32] In fact, the EPR signal associated to this species increases slightly when CeO_2 is loaded with metallic silver[30]. In another study Aneggi et al.[33] have shown that Ag/CeO_2 samples contain Ag crystallites separated from the ceria particles by an Ag_2O phase. Also other authors have reported that ceria is able to maintain silver in a positive oxidation state.[34] Considering this, assuming that metallic silver is responsible for the promotion of O_2 to O_2^-, the interaction between ceria and silver is not ideal as it results in partial oxidation of silver.

An aspect which has not been considered in these studies is the possibility that diluted forms of silver (atom, clusters, nanoparticles) can form during the synthesis and either adsorbed on the surface of the oxide or incorporated into the bulk. Due to their small dimensions, these species would not be detectable with normal

electron microscopies. Therefore, nanosized Ag particles, Ag ions substituting for Ce, or even supported Ag atoms could act as promoters of the catalytic activity facilitating the oxygen adsorption and dissociation. With this respect, Metiu et al. have demonstrated that the presence of Ag ions replacing Ce in the surface of CeO_2(111) causes a considerable weakening of the Ce-O bond and a much lower formation energy of oxygen vacancies.[35] According to this model, if the Ag ions segregate towards the surface they facilitate oxidation mechanisms based on the Mars-van Krevelen mechanism since the activation barrier for oxygen transfer is considerably reduced.

Here we consider two other possibilities. We studied the interaction of an Ag atom and a Ag_5 cluster with the regular and defective surfaces of CeO_2(111) in order to gain insight into the role of the CeO_2/Ag interface in promoting the soot combustion activating oxygen molecules. The behavior of Ag and Ag_5 adsorbed on CeO_2(111) and CeO_{2-x}(111) surfaces is discussed in details in chapter 7. In summary, what we found is a general tendency of Ag atoms and clusters to reduce the stoichiometric and defective ceria surfaces transferring charge from the Ag 5s levels to the Ce ions of the oxide. An opposite effect occurs when the Ag atom is deposited on an O vacancy, with formation of Ag^-.

Considering the interaction of O_2 molecules with adsorbed Ag atoms and clusters, we start from the case of a single Ag atom adsorbed on the stoichiometric CeO_2(111) surface. As said before, in this case Ag carries a positive charge. O_2 binds to the Ag^+ species by 0.45 eV forming a bent complex (r(Ag-O) = 2.116 Å, α(AgOO) = 111°). This is a considerably stronger bond than that of O_2 on the regular surface (see Sec. 5.3.2). Thus, an effect of diluted Ag atoms adsorbed on the ceria surface could be increasing the sticking probability of the incoming O_2 molecules. However, there is no sign of activation of the O_2 molecule. The O-O bond distance, 1.251 Å, is

only slightly elongated compared to gas-phase O_2. The spin remains localized on the Ce^{3+} and no oxidation of the support occurs. Then, no sign of any particular promoting effect of Ag^+ ions adsorbed on the surface is observed.

We also considered another structure where the O_2 molecule interacts with the Ce^{3+} ion of the surface near the adsorbed Ag^+, in order to check possible bonding of O_2 at the interface between Ag_1 and CeO_2. The optimization leads to a weakly bound non-activated O_2 molecule, no interaction with the Ag^+ ion is observed and no charge transfer occurs towards O_2. Thus, there is no direct beneficial effect from the presence of the Ag^+ adsorbed species.

The next case considered is O_2 adsorption on a Ag atom bound to an oxygen vacancy. In this case the Ag adatom is negatively charged (see Chapter 7). We first placed the O_2 molecule on-top of the Ag atom, and reoptimized the structure. This results in a local minimum where the O_2 molecule is weakly bound to Ag, by 0.1 eV, forming a relatively long Ag-O bond, 2.239 Å, and an angle α(AgOO) = 119°. In this complex the O_2 molecule is non-activated (r(O-O) = 1.250 Å) and the negative charge remains on Ag (Figure 5.4).

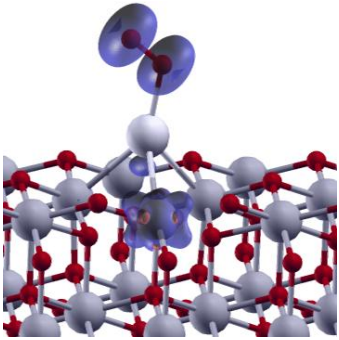

Figure 5.4: $O_2/Ag_1/CeO_{2-x}$ with O_2 interacting with the silver atom only.

However, a second more stable minimum exists where O_2 interacts with *both* Ag and the CeO_{2-x} surface, thus being an interface bonding. In this configuration, the O_2 molecule is strongly bound, by 2.06 eV, and induces a massive structural rearrangement, Figure 5.5.

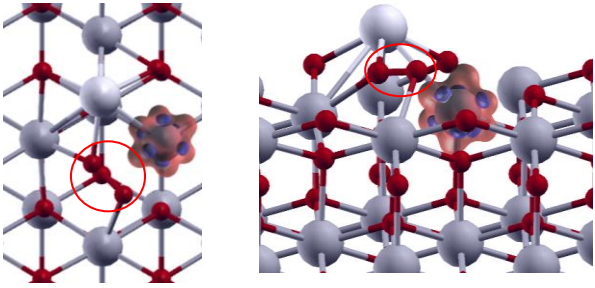

Figure 5.5: $O_2/Ag_1/CeO_{2-x}$ with Ag interacting at the interface position.

In fact, O_2 lies now parallel to the surface, and replaces the missing oxygen. This is not necessarily the lowest configuration, probably a barrier prevents the molecule from adsorbing with the molecular axis perpendicular to the surface, as for a typical peroxo species. The Ag atom is displaced from its original position, and shifted to a vicinal adsorption site where it is bound to three O atoms. Notice that this is the preferred position of Ag_1 on the regular surface. The O-O distance of the adsorbed O_2 molecule, 1.43 Å, is clearly indicative of the formation of a peroxo species, O_2^{2-}. Interestingly, the two extra electrons are not coming from the CeO_{2-x} substrate, in fact one Ce^{3+} ion is still present in the supercell, but from the Ag species which changes its oxidation state from -1 to +1. In other words, when the O_2 molecule interacts at the interface of Ag_1/CeO_{2-x} it takes the position of the Ag atom which is displaced to another adsorption site and a double charge transfer occurs from Ag to O_2 with formation of

peroxo and Ag^+ species. The final result is that the Ag atom assumes the same position and oxidation state that it has on the stoichiometric surface. With this respect, the key role is not that of silver, but rather that of the oxygen vacancy which is the real source of electrons to reduce the oxygen molecule.

The last case considered is that where the O_2 molecule interacts with the Ag_5/CeO_{2-x} complex. The question is weather the simultaneous presence of the Ag_5 cluster and a reduced ceria surface results in an easier electron transfer to O_2 and in the activation of the molecule. We started adsorbing O_2 on top of the Ag_5 cluster reoptimizing the structure. We found a minimum where the O_2 molecule is bound to the Ag cluster, Figure 5.6a, with the molecular axis almost normal to the surface.

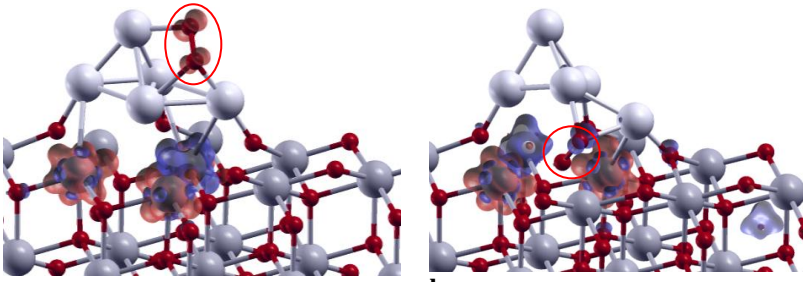

Figure 5.6: Structure of O_2 adsorbed on $Ag_5/CeO_{2-x}(111)$ surface complex. (a) Isomer where O_2 is above the Ag cluster and forms a superoxo species (less stable); (b) isomer where O_2 is below the Ag cluster and forms a peroxo group (more stable).

An electron transfer occurs from the Ag cluster, not from the support, to O_2 with consequent formation of a superoxo radical (r(O-O) = 1.386 Å; Bader charges –0.45 and –0.37e on the bottom and top O atoms, respectively, Figure 5.6a). This structure, however, is about

1.8 eV less stable than a second structure where the O_2 molecule is below the Ag_5 unit, in direct interaction with the ceria surface, Figure 5.6b. One of the O atoms fills the vacancy and the other is in direct contact with the Ag cluster, O_2 is thus at the interface. What is formed, however, is a peroxo group, as shown by the typical O-O distance of 1.46 Å and by the Bader charges, –0.71 and –0.60e on the bottom and top O atoms. We have not investigated the barrier which separates the two isomers found, but at the temperatures at which soot oxidation occurs there should be no problem in overcoming this barrier.

This means that a small Ag cluster stabilized at an O vacancy can promote formation of superoxo species, but not in a catalytic way since it is likely that the O_2 molecule will diffuse below the cluster and saturate the vacancy. Also considering the other results obtained for O_2 interacting with supported species, there is no unambiguous evidence that small silver clusters on ceria can have a special role in the activation of molecular oxygen.

5.4 Conclusions

In this chapter, some key aspects of the reactivity of Ag-modified CeO_2 surfaces used for soot combustion in particulate Diesel filters are analyzed. To this end we considered O_2 molecules and small carbon clusters adsorbed and coadsorbed on the CeO_2(111) stoichiometric and reduced surface. The results show that carbonaceous adsorbed species react with the ceria surface with formation of oxygenated carbon fragments and consequent formation of reduced ceria. The reaction is thermodynamically accessible as it involves only small energy costs. This result agrees with the experimental observation that the soot oxidation involves lattice and

not ambient oxygen. Less clear is the mechanism which occurs to replenish the oxygen content of the oxide catalyst. In fact, both peroxo and superoxo species can form on the surface (these latters most likely in correspondence of low-coordinated Ce ions) but it remains unclear how these species re-establish the oxygen content. Probably by migration of oxygen vacancies from the bulk to the surface, an aspect which has not been considered here.

Since experimental studies point towards a beneficial effect of catalysts based on both Ag and CeO_2 components, we have considered how small silver units, atoms or clusters, deposited on the surface of ceria can activate oxygen molecules. Considering a Ag atom on stoichiometric ceria, that is oxidized (Ag^+), we notice a stronger bonding to the Ag^+ ion of gas-phase O_2 molecules than on the clean CeO_2(111) surface. This result suggests that the sticking probability of oxygen should increase in the presence of adsorbed Ag ions, facilitating oxygen refilling. On the contrary, no beneficial effect is found for a Ag atom adsorbed on a O vacancy since the final result is that the O_2 molecule fills the vacancy with formation of a peroxo group. The Ag atom is displaced from its original position, showing that the affinity of the vacancy for oxygen is much larger than for Ag.

Finally, we have considered Ag_5 clusters deposited on the stoichiometric and reduced ceria surfaces. Considering the cluster adsorbed on an oxygen vacancy, O_2 adsorption results in the formation of a superoxo species, an effect which has not been observed with other models considered here. This could indicate that at the interface between the Ag phase and reduced ceria samples one can form more easily activated oxygen species. However, the superoxo molecule can migrate below the Ag cluster and bind directly to the O vacancy with formation of a peroxo group. With this respect, the final effect is not very different from what occurs

when O_2 binds directly to an O vacancy and the role of the silver particle is not particularly relevant, at least from a thermodynamic point of view.

The result of this chapter have been reported in the following publication:

Formation of oxygen active species in Ag-modified CeO_2 catalyst for soot oxidation: A DFT study.

Preda G., Pacchioni G., *Catalysis Today*, 177, (**2011**), 31.

5.5 Bibliography

[1] S. H. Vosko, L. Wilk, M. Nusair, *Can. J. Phys*. 58 (**1980**) 1200.
[2] J. P. Perdew, J. A. Chevary, S. H. Vosko, K. A. Jackson, M.R. Pederson, D. J. Singh, C. Fiolhais, *Phys. Rev. B* 46 (**1992**) 6671.
[3] J. P. Perdew, J. A. Chevary, S. H. Vosko, K. A. Jackson, M. R. Pederson, D. J. Singh, C. Fiolhais, *Phys. Rev. B* 48 (**1993**) 4978.
[4] S. L. Dudarev, G. A. Botton, S. Y. Savrasov, C. J. Humphreys, A. P. Sutton, *Phys. Rev. B* 57 (**1998**) 1505.
[5] H. J. Monkhorst, J. D. Pack, *Phys. Rev. B* 13 (**1976**) 5188.
[6] M. Methfessel, A. T. Paxton, *Phys. Rev. B* 40 (**1989**) 3616.
[7] R. F. W. Bader, *Atoms in Molecules*; Oxford University Press: Oxford, **1990**.
[8] G. Henkelman, A. Arnaldsson, and H. Jónsson, *Comput. Mater. Sci*. 36 (**2006**) 254-360; W. Tang, E. Sanville, G. Henkelman, J. *Phys.: Condens. Matter* 21 (**2009**) 084204.
[9] M. Nolan, S. Grigoleit, D.C. Sayle, S.C. Parker, G.W.Watson, *Surf. Sci*. 576 (**2005**) 217.
[10] C. Loschen, J. Carrasco, K.M. Neyman, F. Illas, *Phys. Rev. B* 75 (**2007**) 035115.
[11] M.V. Ganduglia-Pirovano, A. Hofmann, J. Sauer, *Surf. Sci. Rep*. 62 (**2007**) 219.
[12] G. Pacchioni, *J. Chem. Phys*. 128 (**2008**) 182505
[13] E. Wuilloud, B. Delley, W.-D. Schneider, Y. Baer, *Phys. Rev. Lett*. 53 (**1984**) 202.
[14] M.M. Branda, C. Loschen, K. Neyman, F. Illas, *J. Phys. Chem. C* 112 (**2008**) 17643.
[15] F. Esch, S. Fabris, L. Zhou, T. Montini, C. Africh, P. Fornasiero, G. Pomelli, R. Rosei, *Science* 309 (**2005**) 752.
[16] M. V. Ganduglia-Pirovano, J. L. F. Da Silva, J. Sauer, *Phys. Rev. Lett*. 102 (**2009**) 026101.
[17] H.-Y. Li, H.-F. Wang, X.-Q. Gong, Y.-L. Guo, G. Lu, P. Hu, *Phys. Rev. B* 79 (**2009**), 193401.
[18] H. L. Tuller, A. S. Nowick, *J. Phys. Chem. Solids* 38 (**1977**) 859.
[19] M. Huang, S. Fabris, *Phys. Rev. B* 75 (**2007**) 081404(R).
[20] H.-T. Chen, J.G. Chang, H.L. Chen, S.-P. Lu, *J. Comput. Chem*. 30 (**2009**) 2433.

[21] V.V. Pushkarev, V.I. Kovalchuk, J.L. d'Itri, *J. Phys. Chem. B* 108 (**2004**) 5341.
[22] J. C. Conesa, *Catal. Today* 143 (**2009**) 315.
[23] Y.M. Choi, H. Abernathy, H.-T. Chen, M.C. Lin, M. Liu, *Chem. Phys. Chem.* 7 (**2006**) 1957.
[24] J. Soria, A. Martinez-Arias, J. Conesa, *J. Chem. Soc. Faraday Trans*. 91 (**1995**) 1669.
[25] A. L. Linsebigler, G. Lu, J. T. Yates, *Chem. Rev*. 95 (**1995**) 735.
[26] T. Berger, M. Sterrer, O. Diwald, and E. Knözinger, D. Panayotov, T. L. Thompson, and J. T. Yates, *J. Phys. Chem. B* 109 (**2005**) 6061.
[27] C. Loschen, A. Migani, S.T. Bromley, F. Illas, K.M. Neyman, *Phys. Chem. Chem. Phys*. 10 (**2008**) 5730.
[28] A. Bueno-Lopez, K. Krishna, M. Makkee, J.A. Moulijn, *J. Catal*. 230 (**2005**) 237
[29] G. Pacchioni, J. Koutecky, *J. Chem. Phys*. 88 (**1988**) 1066.
[30] M. Machida, Y. Murata, K. Kishikawa, D. Zhang, K. Ikeue, *Chem. Mater*. 20 (**2008**) 4489.
[31] D. A. Outka, J. Stöhr, W. Jark, P. Stevens, J. Solomon, E. J. Madix, *Phys. Rev. B* 35 (**1987**) 4119.
[32] P. A. Gravil, D. M. Bird, J. A. White, *Phys. Rev. Lett*. 77 (**1996**) 3933.
[33] E. Aneggi, J. Llorca, C. de Leitenburg, G. Dolcetti, A. Trovatelli, *Appl. Catal. B: Environ*. 91 (**2009**) 489.
[34] L. L. Murriel, R. T. Carlin, *J. Catal*. 159 (**1996**) 479.
[35] V. Shapovalov, H. Metiu, *J. Catal*. 245 (**2007**) 205.

Chapter 6

O_2^- on ceria nanoparticles by interaction of molecular oxygen with Ce^{3+} sites

6.1 Summary

In this chapter we analyze the behavior of low coordinated Ce^{3+} centers towards the activation of oxygen molecules.
In literature is known that the exposure of ceria to molecular oxygen results in the formation of peroxo, O_2^{2-}, and superoxo, O_2^-, species. The formation of diamagnetic peroxo species is easily explained by the interaction of O_2 with oxygen vacancies at the ceria surface since these are two-electron donor centers. On the contrary, the formation of the paramagnetic superoxide O_2^- radical cannot be explained by the same model since this complex spontaneously converts into the more stable peroxo group, as seen in Chapter 5. Based on DFT calculations we show that superoxide O_2^- radicals form by direct interaction of O_2 with low-coordinated Ce^{3+} ions on reduced ceria nanoparticles and we propose an atomistic model of this system, which is fully consistent with the experimental observation. The results reported in these chapter have been obtained in collaboration with Dott. Annapaola Migani and Prof. Francesc Illas of the Universitat de Barcelona.

6.2 Computational details

The calculations for the smaller Ce_2O_3 cluster have been performed with two radically different computational approaches. We first used a typical quantum chemical approach based on localized basis functions (Gaussian type orbitals), an effective core potential (ECP) for the description of Ce, and the B3LYP hybrid exchange correlation functional. For these calculations we used the Gaussian03 code.[1] We used for the Ce atoms the ECP and basis set developed by the Stuttgart/Dresden group which includes only 28 electrons in the core and treats the remaining 30 electrons explicitly as valence electrons. The corresponding contracted basis set is [5s5p4d3f].[2-4] The (all-electron) basis set for oxygen is 6-31G* on the O atoms of the Ce_2O_3 cluster and 6-311+G* on O_2.

The same system has then been considered using a plane wave basis set, the projector augmented wave (PAW) method,[5] and both the HSE06 hybrid functional[6-8] and the GGA+U (with U_{eff} = 4eV) approach. For these calculations the VASP package was used. The GGA+U approach has been used also for the study of the $Ce_{24}O_{47}$ and $Ce_{40}O_{79}$ nanoparticles.

The hyperfine interactions of the electron spin with the nuclear spin of the ^{17}O nuclide have been determined.

For the VASP calculations, a supercell approach is used which includes a vacuum of ~1 nm in the three Cartesian directions. For these discrete systems only γ-point calculations are performed. The valence electron density is defined by the twelve ($5s^2 5p^6 6s^2 5d^1 4f^1$) electrons of each Ce atom and the six ($2s^2 2p^4$) electrons of each O atom and a cutoff of 415 eV was used for the kinetic energy of the plane waves entering into the basis set. Hybrid DFT calculations were performed using the HSE06 functional as implemented in VASP. The lowest-energy morphology of the pristine $Ce_{24}O_{48}$ and

$Ce_{40}O_{80}$ nanoparticles (parent clusters of O deficient $Ce_{24}O_{47}$ and $Ce_{40}O_{79}$ structures), are identified by global optimization by a basin-hopping approach using interatomic potentials.[9,10] This procedure ensures that the nanoparticle geometries employed correspond to, or should approach, the global energetic minima.

6.3 Results and discussion

6.3.1 Interaction of O_2 with the Ce_2O_3 model system

The small bipyramidal trigonal Ce_2O_3 cluster, Figure 6.1, provides an excellent system to test the response of various methods in describing the Ce^{3+}-O_2 interaction. In a recent study it has been shown that this small cluster is representative of cerium sesquioxide (bulk Ce_2O_3), provided that an appropriate basis set and exchange correlation functional is chosen.[11] The ground state of the Ce2O3 cluster is a triplet with two unpaired electrons each localized on a 4f level of the three-coordinated apical Ce ions, with a magnetic moment on each Ce of ~ 1 μ_B,. The Ce-O distances in this molecule predicted by the B3LYP functional are 2.140 Å, Figure 1.6.

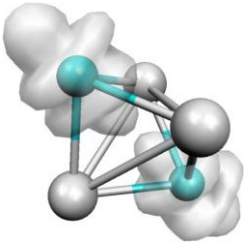

Figure 6.1: The Ce_2O_3 cluster with the spin density plot.

An O_2 molecule has been adsorbed in the vicinity of one of the two equivalent Ce^{3+} ions in two different conformations, side-on, η_2, i.e. with the O-O axis perpendicular to the Ce-Ce axis, (Figure 6.2a), and end-on, η_1, i.e. with one O atom of the O_2 molecule pointing directly towards Ce, (Figure 6.2c). Since the O_2 molecule has a $^3\Sigma_g^-$ ground state, the interaction with the triplet state of Ce_2O_3 can result in singlet, triplet or quintet state depending on whether there is total, partial or no spin pairing, respectively. The quintet state does not correspond to the formation of a chemical bond, is higher in energy and has not been considered. The singlet state leads to a double electron transfer and to the formaton of a stable diamagnetic peroxo species, as shown by the found O-O distance of 1.441 Å. However, this situation is 0.3 eV (B3LYP) higher in energy than the triplet ground state. When the triplet state is considered, all functionals and methods indicate the formation of the superoxide radical anion, O_2^- (one unpaired electron on O_2^- and one on a Ce^{3+} ion). The formation of a superoxo species is shown unambiguously by the spin density analysis and by the charge analysis (Mulliken or Bader), which show the presence of only one unpaired electron associated to the O_2 molecule, and by the O-O distance which is about 1.3 Å, a typical value for this species. The distances calculated for free O_2 and O_2^- with the considered methods are: 1.206 and 1.346 Å in B3LYP, 1.211 and 1.333 Å in HSE06, and 1.235 and 1.316 Å in GGA+U, respectively. Further proof of the formation of a superoxo species comes from the calculation of the IR and EPR spectra, as it will be discussed below.

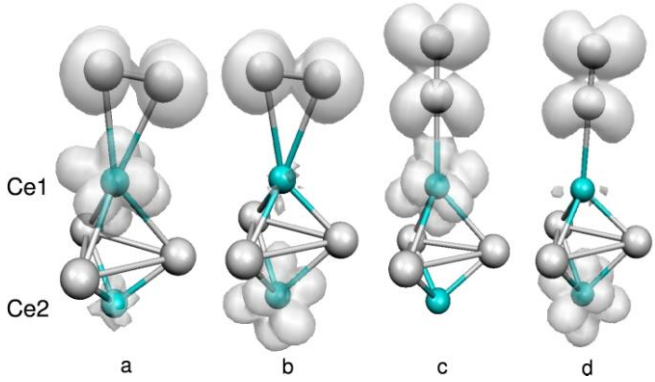

Figure 6.2: Structures of Ce_2O_3-O_2 complexes: (a) Side on, η_2 (Ce1); (b) Side on, η_2 (Ce2); (c) End on, η_1 (Ce1); (d) End on, η_1 (Ce2). For selected distances and angles see Table 6.1. Grey – spin-density iso-surface of 0.05e/Å^3.

The triplet configuration of the Ce_2O_3-O_2 complex can originate in principle from two mechanisms. One is the coupling between the 4f electron on Ce and one of the π_g^* electrons of O_2, leading to a covalent interaction. The other is a charge transfer of one of the two Ce^{3+} $4f^1$ electrons to the O_2 molecule with formation of a Ce^{4+}-O_2^- complex, establishing an ionic interaction. In both cases, the 4f electron that should be involved is that on the Ce ion nearest to the O_2 molecule, with formal change of its oxidation state from +3 to +4. However, what we found is that all the calculations, independently on the method used, show the existence of two electronic states which differ only by the position of the unpaired electron on the Ce_2O_3 unit (Table 6.1), both for side-on η_2, and end-on η_1 adsorption configurations. In one state the unpaired electron remains on the Ce ion nearest to O_2 (hereafter referred to as Ce1) while in the other state the unpaired electron is localized on the Ce ion on the opposite side of the cluster, Ce2 (Figure 6.1).

Table 6.1		Method	D_e eV	r(O-O) Å	ν(O-O) cm^{-1} (a)	r(Ce-O) Å	α(CeOO) °	Magnetic moment		
								Ce1	Ce2	O_2
								μ_B		
Ce_2O_3	Side-on η_2(Ce1)	B3LYP	1.39	1.331	1181	2.466	74.3	0.98	0.03	1.02
		HSE06	1.70	1.323	1258	2.420	74.1	0.95	0.03	0.84
		GGA+U	1.15	1.351	1145	2.454	74.0	0.91	0.10	0.80
	Side-on η_2(Ce2)	B3LYP	1.21	1.317	1189	2.477	74.5	–0.06	1.02	1.07
		HSE06	1.59	1.314	1278	2.420	74.2	–0.01	0.95	0.86
		GGA+U	1.49	1.336	1163	2.462	74.3	–0.06	0.98	0.85
	End-on η_1 (Ce1)	B3LYP	0.84	1.313	1221	2.267	179.9	1.06	0.00	0.96
		HSE06	1.01	1.310	1267	2.247	179.3	0.98	0.00	0.79
		GGA+U	0.46	1.329	1150	2.277	179.4	0.93	0.07	0.77
	End-on η_1 (Ce2)	B3LYP	0.78	1.291	1141	2.296	178.9	–0.15	1.03	1.11
		HSE06	0.91	1.299	1270	2.245	178.0	–0.01	0.96	0.83
		GGA+U	0.71	1.302	1191	2.343	177.9	–0.24	0.96	0.98
$Ce_{24}O_{47}$	Side-on η_2(Ce2)	GGA+U	1.13	1.335	1159	2.410	73.9	–0.06	0.96	0.85
$Ce_{40}O_{79}$	Side-on η_2(Ce2)	GGA+U	1.35	1.338	1157	2.431	74.0	–0.06	0.95	0.85

Table 6.1: Adsorption properties of superoxide radical anion (O_2^-) formed by interaction of O_2 with a Ce_2O_3 cluster, and $Ce_{24}O_{47}$, $Ce_{40}O_{79}$ nanoparticles. (a) Experimental Raman 1127-1135 cm^{-1}[12,13] and IR (1125 cm^{-1}[14]) values.

All methods clearly indicated that the side-on η_2 isomer is the most stable one, no matter where the spin is localized (Table 6.1). The hybrid functionals, B3LYP and HSE06, indicate this complex, Figure 6.2a, as the most stable one separated by a small energy difference, 0.1-0.2 eV, from the situation where the unpaired electron is on Ce2 (Figure 6.2b). The O_2 binding energies are somewhat different in the two approaches, 1.39 eV in B3LYP and 1.70 eV in HSE06, but both indicate a substantial stability of the superoxide anion. Also the GGA+U approach indicates η_2 as the preferred O_2 orientation, but the order of stability of the two electronic states is reversed: the case where the spin is on Ce2 is now the ground state with a binding energy of 1.49 eV, while the configuration with the spin on Ce1 is 0.34 eV higher in energy, Table 6.1. All other adsorption properties here reported, in particular bond distances, and spin distribution, are quite consistent in the three approaches (B3LYP, HSE06, GGA+U), see Table 6.1.

As said in Chapter 5, when an O vacancy is formed on the surface of CeO_2 there are several Ce ions where the two excess electrons can localize and that these configurations are all within a few tenth of an eV.[15,16] What is found here is to some extent a similar result. However here the charge transfer nature of the interaction between O_2 and reduced ceria is shown in a very clear way. In fact, in a covalent Ce-O_2 interaction the spin quenching would involve the coupling of Ce1 4f and O_2 unpaired electrons, leaving the other unpaired electron on the second Ce atom, Ce2. On the contrary, our results show that the O_2 molecule takes one of the two electrons of the Ce_2O_3 complex and remains stabilized near a Ce

cation, and moreover the total energy is similar when the configuration of this cation changes from $4f^0$ to $4f^1$. On purely electrostatic arguments one would expect that the Ce^{4+}-O_2^- interaction (unpaired electron on Ce2) should be stronger than the Ce^{3+}-O_2^- one (unpaired electron on Ce1). Apparently, the electrostatic potential on the two sites is not so different and other binding mechanisms occur, e.g. polarization, dispersion, etc.. With the GGA+U approach it was found that the electronic state where the spin is on Ce2 is more stable, Table 6.1. This result suggests that the Ce-O_2^- bonding has a larger covalent character with this method than with hybrid functionals, a result which is consistent with the fact that the use of the HF exchange favors electrostatic interactions.

The other structural isomer of the Ce_2O_3-O_2 complex is the end-on η_1 linear configuration, Figure 6.2c and d. All methods indicate that this isomer is less stable than the η_2 one, with energy differences of 0.4-0.8 eV, Table 6.1.

Finally, we have computed the observable IR and EPR properties of the O_2^- species for the different Ce_2O_3-O_2 complexes considere, Table 6.1 and Table 6.2.

Structure	a_{iso}	B_x	B_y	B_z
	G	G	G	G
Side-on, η_2 (Ce1)[(a)]	-4.9	29.3	-60.3	31.1
Side-on, η_2 (Ce2)[(a)]	-5.0	26.9	-59.6	32.6
End-on, η_1 (Ce1)[(b)]	-3.6	-35.3	17.8	17.5
	-6.1	-78.2	39.3	38.9
End-on, η_1 (Ce2) [(b)]	-5.0	-33.9	25.7	8.2
	-6.6	-71.9	43.2	28.7

Table 6.2: EPR properties (O hyperfine coupling constants) of a superoxide radical anion (O_2^-) formed by interaction of O_2 with a Ce_2O_3 cluster (B3LYP results). (a) The definition of the orientation is as follows: the z direction corresponds to the internuclear O_2 axis, and the x direction coincides with the Ce–superoxide bond axis, parallel to the Ce-O-Ce plane. (b) The z direction corresponds to the internuclear O_2 axis.

The calculation of the hyperfine coupling constants of the unpaired electron with the ^{17}O nucleus gives important informations on the symmetry of the complex and can be used to discriminate between the η_2 and η_1 isomers. The calculated vibrational properties of the Ce_2O_3-O_2 complex indicate a stretching frequency for the O-O bond of 1181 cm^{-1} for the η_2 (Ce1) complex in our B3LYP calculation. This value is in line with the ones reported for superoxide complexes formed on ceria surfaces or nanoparticles, Table 6.1. The values computed for the η_1 structures are 1221 cm^{-1} or 1141 cm^{-1}, depending whether the other unpaired electron is on Ce1 or Ce2, and are also consistent with the formation of a superoxide radical. The values calculated with the HSE06 and GGA+U approaches are in the same range, Table 6.1. This indicates that the classification suggested in literature[12] of η_1 (end-on) and η_2 (side-on) Ce-O_2 complexes to superoxo and peroxo species, respectively, is not really justified.
The computed hyperfine coupling constants, Table 6.2, are fully consistent with those of superoxide radicals. The A tensor has the

same structure and similar quantitative values of the O_2^- species formed at the surface of various oxides[17] and in particular at Na precovered MgO surfaces, described in details in Chapter 4.[18] The structure of the A tensor clearly reflects the symmetry of the complex. While η_2 (side-on) is consistent with the presence of two equivalent O nuclei, the η_1 (end-on) species contains two non equivalent O atoms, Table 6.2. Experimentally, using a $^{17}O_2$ species Soria et al.[14] identified a family of superoxo species formed on surface defects of CeO_2. One of the dominant species observed has an axial symmetry with $g_1 = g_2 = 2.011$ and $g_3 = 2.034$ and A_1 component of ~75 G (the A_2 and A_3 components are not resolved). The two oxygen atoms are magnetically equivalent. In our calculations $A_y = a_{iso} + B_y$ for the η_2 species is about -65 G. A more resolved EPR spectrum is then desirable to compare better the theoretical results with the experimental ones.

6.3.2 Interaction of O_2 with CeO_2 nanoparticles

Ceria nanoparticles of size ranging from 1-2 to about 10 nm play an essential role in catalytic processes. It is thus important to extend and to validate the results obtained on the small Ce_2O_3 model system to more realistic models. To this end two moderately large aggregates have been considered, $Ce_{24}O_{47}$ and $Ce_{40}O_{79}$, Figure 6.3. Here, because of the size of the systems, only plane wave calculations using the GGA+U approach were performed.

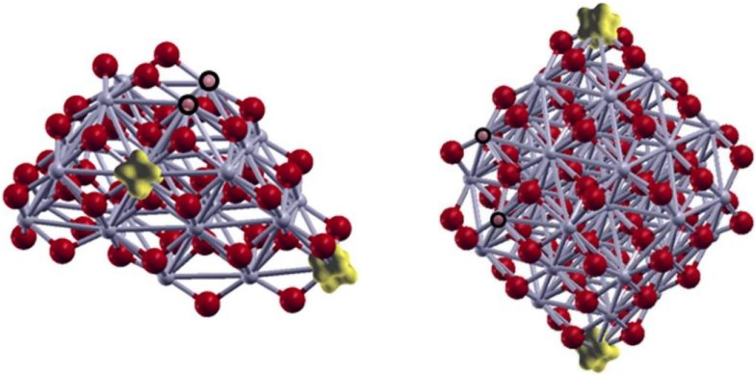

Figure 6.3: Structures of $Ce_{24}O_{47}$ and $Ce_{40}O_{79}$. Black circles: highlighted is the site where an oxygen vacancy has been created by removing a two-coordinated O atom. The spin density isosurface indicates the sites where unpaired electrons are localized.

The smallest $Ce_{24}O_{47}$ nanoparticle (about 1 nm in diameter) starts to exhibit the crystalline fluorite structure of bulk CeO_2, whereas $Ce_{40}O_{79}$ (size of about 1.5 nm) exhibits clearly a bulk-like atomic ordering with exposed O-terminated (111) and (100) facets, thus closely resembling experimentally identified structures of larger ceria nanoparticles.[19,20] It has been found that oxygen vacancies form more easily on the low coordinated sites of the particles and that this results in the formation of Ce^{3+} ions at low coordinated sites, see Figure 6.3. While in $Ce_{40}O_{79}$ the Ce^{3+} ions are located at apical Ce sites, in $Ce_{24}O_{47}$ the Ce^{3+} cations are at edge and apical sites.

O_2 has been adsorbed on an apical Ce^{3+} ion of each cluster and the structure has been fully reoptimized. The apical site has been chosen as it is the one that more likely affect the reactivity in the models employed, because it corresponds to the most exposed site and to the one that stabilizes better the extra electron, accordingly to the electrostatic potentials of the pristine agglomerates.[10] In both cases the formation of a superoxide anion is observed based on the

spin distribution and on the O-O distance, see Table 6.1. The molecule adopts the η_2 (side-on) configuration and the Ce^{3+} ion is localized far away from the Ce^{4+}-O_2^- complex, Figure 6.4.

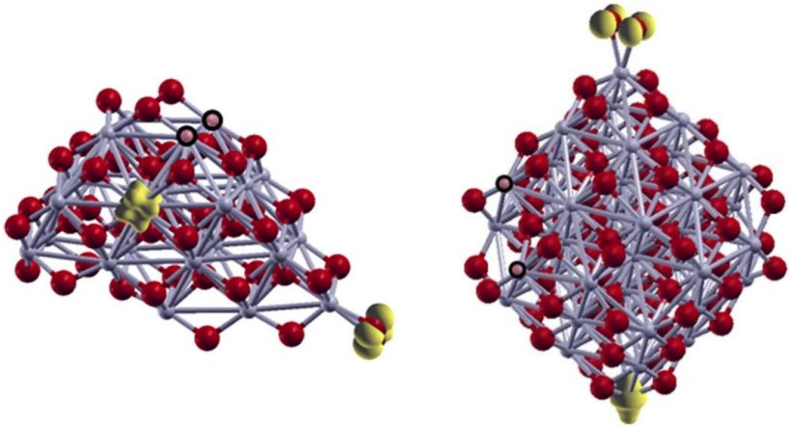

Figure 6.4: Structures of $Ce_{24}O_{47}$-O_2 and $Ce_{40}O_{79}$-O_2 side-on, η_2 complexes.

With this respect the situation is that found for the small Ce_2O_3 model, Ce2 solution. The O_2 binding energy, 1.13 eV on $Ce_{24}O_{47}$ and 1.35 eV on $Ce_{40}O_{79}$, is also similar to that found at the same level of theory on Ce_2O_3, 1.49 eV. This binding energy is fully consistent with the observation that superoxide species on ceria nanocrystallites are stable only up to 348 K (a disappearance of the characteristic Raman band at 1131 cm^{-1} occurs above this temperature).[21] In fact, using a Redhead equation and a frequency factor $\nu_1 = 10^{13}$ s^{-1} (β = 1),[22] this desorption temperature corresponds to a O_2 binding energy of about 1 eV. Also the computed vibrational frequency for the two structures, $Ce_{24}O_{47}$-O_2 and $Ce_{40}O_{79}$-O_2, 1159 and 1157 cm^{-1}, respectively, Table 6.1, are in line with the Raman and IR values for superoxide species.[12,13,14]

6.4 Conclusions

Understanding the formation of activated oxygen species is of fundamental importance for the detailed elucidation of the oxygen exchange mechanism in ceria and hence to better understand its catalytic properties. The formation of superoxide radical anions by adsorption of molecular oxygen on the surface of reduced ceria nanoparticles is usually observed together with the formation of diamagnetic peroxo species. The common model used to explain this reaction is that O_2 interacts with surface O vacancies leading to the formation of the two species. However, oxygen vacancies in reduced ceria, CeO_{2-x}, are two-electron centers since the removal of an O atom results in the formation of two Ce^{3+} ions, (Chapter 5). According to DFT calculations of extended ceria surfaces, O vacancies form preferentially on subsurface sites and the two excess electrons tend to localize on next-nearest neighbors Ce^{3+} ions.[15] As explained in Chapter 5, the fact that an oxygen vacancy is a two electron donor center has a direct consequence: O_2 adsorption on this site always leads to healing the defect and forming the diamagnetic O_2^{2-} peroxo center. Then, the surface oxygen vacancy model cannot explain the formation of superoxo O_2^- radicals.

In this study in collaboration with Dott. Annapaola Migani and the group of Prof. Illas, we have considered the electronic structure of reduced ceria nanoparticles of up to 1.5 nm size, which provide a more realistic representation of the nanostructures present in ceria-based catalysts. In reduced form, these nanoparticles show the presence of Ce^{3+} ions at low-coordinated positions quite far from the site where the O vacancy is formed. O_2 molecules interact strongly with the Ce^{3+} ion, in fact the binding energy are of more than 1 eV. The interaction leads to a charge transfer from Ce 4f states to the π_g^* MO of O_2, resulting in fully oxidized Ce^{4+} ion and O_2^-

superoxide species. The molecule binds preferentially in a side-one mode, with the end-on isomer clearly less favorable. The preference for the side-on bonding mode and the existence of nearly degenerate electronic configurations of the Ce ion where O_2^- is formed can be in +3 or in +4 oxidation state (presence or absence of a localized electron on the 4f states, respectively) is indicative of a pronounced charge-transfer or electrostatic nature of the interaction. Finally, the formation of superoxide species can be thus indicative of the presence of low-coordinated Ce^{3+} ions on the surface of the nanoparticle.

The result of this chapter have been reported in the following publication:

Formation of superoxide anions on ceria nanoparticles by interaction of molecular oxygen with Ce^{3+} sites.

Preda G., Migani A., Neyman K., Bromley S. T., Illas F., Pacchioni G., *J. Phys. Chem. C*, 115, (**2011**), 5817.

6.5 Bibliography

[1] M. J. Frisch, et al., GAUSSIAN03, Revision A.7, Gaussian Inc., Pittsburgh, PA, **2003**.
[2] X. Cao, M. Dolg, *J. Chem. Phys.* 115 (**2001**) 7348.
[3] X. Cao, M. Dolg, *J. Mol. Struct.: THEOCHEM* 581 (**2002)** 139.
[4] D. Feller, *J. Comput. Chem.* 17 (**1996**) 1996.
[5] P. E. Blöchl, *Phys. Rev. B* 50 (**1994**) 17953.
[6] J. Heyd, G. E. Scuseria, M. Ernzerhof, *J. Chem. Phys.* 118 (**2003**) 8207.
[7] J. Paier, M. Marsman, K. Hummer, G. Kresse, I. C. Gerber, J. G. Angyan, *J. Chem. Phys.* 125 (**2006**) 24990.
[8] J. Heyd, G. E. Scuseria, M. Ernzerhof, *J. Chem. Phys.* 124 (**2006**) 219906.
[9] A. Migani, G. N. Vayssilov, S. T. Bromley, F. Illas, K. M. Neyman, *Chem. Commun*. 46 (**2010**) 5936.
[10] A. Migani, G. N. Vayssilov, S. T. Bromley, F. Illas, K. M. Neyman, *J. Mater. Chem.* 20 (**2010**) 10535.
[11] J. Kullgren, C. W. M. Casteleton, C. Müller, D. Munoz Ramo, K. Hermansson, *J. Chem. Phys.* 132 (**2010**) 054110.
[12] V. V. Pushkarev, V. I. Kovalchuk, J. L. d'Itri, *J. Phys. Chem. B* 108 (**2004)** 5341.
[13] Y. M. Choi, H. Abernathy, H.-T. Chen, M. C. Lin, M. Liu, *ChemPhysChem* 7 (**2006**) 1957.
[14] J. Soria, A. Martinez-Arias, J. Conesa, *J. Chem. Soc. Faraday Trans.* 91 (**1995**) 1669.
[15] M. V. Ganduglia-Pirovano, J. L. F. Da Silva, J. Sauer, *Phys. Rev. Lett.* 102 (**2009**) 026101.
[16] H.-Y. Li, H.-F. Wang, X.-Q. Gong, Y.-L. Guo, Y. Guo, G. Lu, P. Hu, *Phys. Rev. B* 79 (**2009**) 193401.
[17] M. Che, A. J. Tench, *Advances in Catalysis*, Vol. 32, Elsevier, Amsterdam **1983**.
[18] F. Napoli, M. Chiesa, E. Giamello, G. Preda, C. Di Valentin, G. Pacchioni, *Chem. Europ. J.* 16 (**2010**) 6776.
[19] Z. L. Wang, X. D. Feng, *J. Phys. Chem. B* 107 (**2003**) 13563.
[20] A. S. Barnard, A. I. Kirkland, *Chem. Mater.* 20 (**2008**) 5460.
[21] Z. Wu, M. Li, J. Howe, H. M. Meyer III, S. H. Overbury, *Langmuir* 26 (**2010)** 16595.

[22] A. M. Dejong, J. W. Niemantsverdriet, *Surf. Sci*. 233 (**1990**) 355.

Chapter 7

Silver islands and nanoparticles on CeO_2(111)

7.1 Summary

As said in the introduction, in a recent study Machida et al.[1] have reported that loading the ceria catalyst with Ag metal leads to an improved catalytic activity and a lower combustion temperature. In this Chapter we analyze in details the behaviour of Ag nanoparticles deposited on stoichiometric and reduced thin CeO_2 films grown on Pt(111). The nucleation and growth of the Ag nanoparticles has been characterized experimentally and with our DFT calculations on Ag atoms, clusters, and extended layers deposited on slab models of the CeO_2(111) surface. Experimentally, the XPS spectra clearly show a reduction of the ceria support by Ag deposition (formation of Ce^{3+} ions). This is accompanied by a positive shift of the Ag 3d core levels, in which final state effects related to the finite size of the Ag deposits come into play. The DFT calculations confirm the view of a direct electron transfer from the Ag clusters and nanoparticles to the ceria support. Other possible origins of the reduction of the ceria substrate, like the occurrence of oxygen reverse spillover on the Ag nanoparticles, is ruled out based on energy considerations. The experimental results have been provided by Dott. Paola Luches and Prof. Sergio Valeri of the Università di Modena e Reggio Emilia.

7.2 Computational details

Spin polarized DFT calculations have been carried out to study the interaction between Ag atoms, clusters, and extended one or two monolayers (ML) and the $CeO_2(111)$ surface. The calculations have been performed with the VASP package using a plane wave basis set and the projector augmented wave (PAW) method to describe the interaction between the valence electrons and the atomic cores. The valence electron density is defined by the twelve electrons of each Ce atom, the six electrons of each O atom, and the eleven electrons of Ag, as in Chapter 5. Also the kinetic energy cutoff, the LDA+*U* or GGA+*U* approaches, the *k*-points grid and the Methfessel-Paxton smearing width are the same used for the calculations in Chapter 5.

Geometry optimization has been performed within the LDA+*U* exchange-correlation potential with U_{eff} = 5 eV that provides a lattice parameter close to experiment.[2] Magnetic moments and Bader charges[3,4,5] have been obtained at the same level of theory whereas energies were calculated at the GGA+U level with U_{eff} = 3 eV or 4 eV. This choice gives a proper description of the localization in bulk Ce_2O_3 as well as in ceria nanoparticles containing both Ce^{3+} and Ce^{4+} atoms.[6]

To model the O-terminated $CeO_2(111)$ surface 2 × 2 (Ce_8O_{16}), 3 × 3 ($Ce_{18}O_{36}$) or 4 × 4 ($Ce_{32}O_{64}$) supercells with 6 or 9 atomic layers (2ML or 3ML, respectively) have been used keeping the three bottom layers fixed and relaxing the other ones. The slab model was cut from the same bulk cubic (*Fm*3*m*) CaF_2-like structure considered in Chapter 5 using the same optimized LDA+U lattice parameter a_0 = 5.40 Å. The supercell includes a vacuum width of about 12 Å to avoid interaction between the slabs.

7.3 Results and discussion

7.3.1 Experimental aspects

Experimentally, the substrates used were cerium oxide ultrathin films grown on Pt(111), annealed at 1040 K in O_2 after the growth. For nominal CeO_2 thickness above 3 ML a large fraction of the Pt surface is covered by atomically flat cerium oxide terraces several tens of nm wide (Figure 7.1a), separated by single O-Ce-O steps (A in Figure 7.1b).

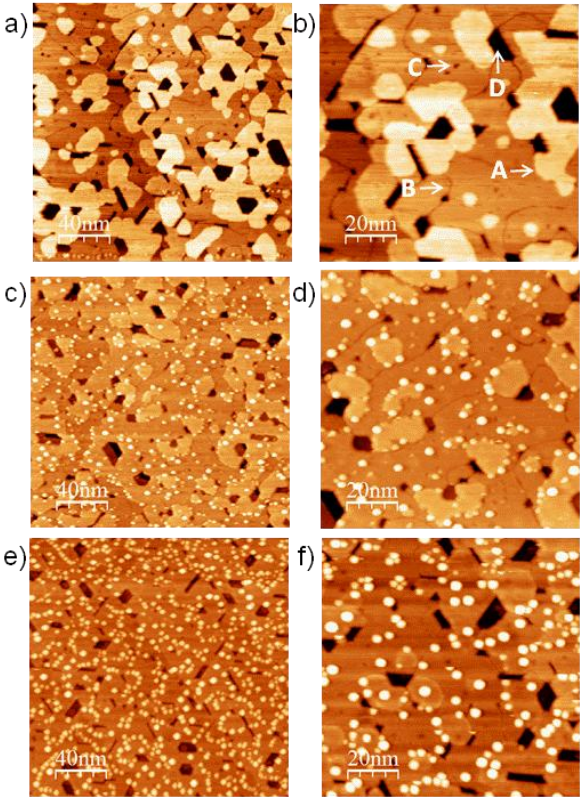

Figure 7.1: a) STM images of: a) a 3 ML CeO_2 film on Pt(111); b) a zoom of a) evidencing O-Ce-O steps (A), linear defects (B), bidimensional defects (C) and holes down to the Pt substrate (D); c) 0.07 Å Ag on a 3 ML CeO_2 film; d) zoom of c) revealing the tendency for Ag nanoparticles to decorate the steps between ceria terraces, inset: zoom showing hexagonal nanoparticles; e) and f) 0.2 Å Ag on a 3 ML CeO_2 film.

Linear defects are also present on the terraces (B in Figure 7.1b) and a number of defects with a few nm lateral size are present (C in Figure 7.1b). Most of the darker holes with lateral size of a few tens of nm (D in Figure 7.1b) extend down to the Pt surface. The ceria films grow epitaxially on Pt(111).[7] The Ce 3d XPS spectra of the bare films indicates a Ce^{3+} concentration below 1-2%.[7]

The deposition of 0.07 Å of Ag at RT leads to the formation of Ag nanoparticles on the ceria surface, as shown by the STM image in Figure 7.1c,d. Ag nanoparticles have the tendency to decorate ceria-ceria terrace step edges (Figure 7.1d). Some nanoparticles are found also on the terraces, possibly nucleating at some smaller scale surface defect. The Ag nanoparticle shape appears mainly hexagonal (inset of Figure 7.1d), suggesting a (111) orientation of the Ag nanoparticles surface. By increasing the amount of deposited Ag the nanoparticles increase mainly in lateral size and height (Figure 7.1e, f), while their density is only slightly increased.
The electronic properties of the Ag/CeO_2 system were investigated by XPS. Figure 7.2a shows the Ag 3d XPS lines for samples with different amount of Ag and for a 50 Å thick Ag film, the latter used as a reference for bulk Ag.

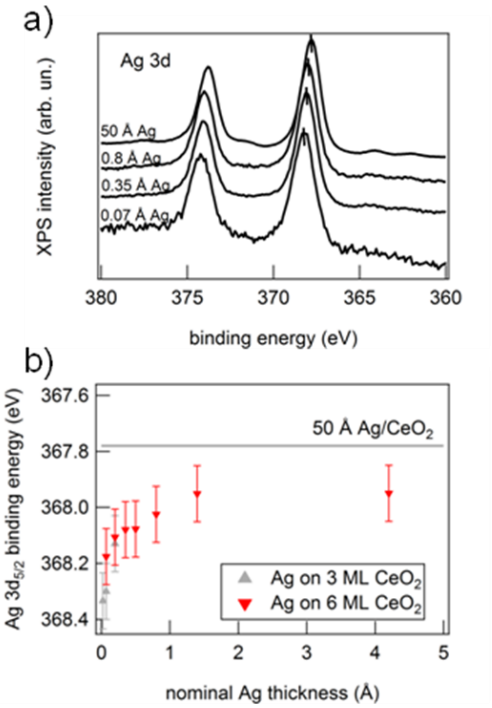

Figure 7.2: a) Ag 3d XPS spectra of samples with different amount of Ag and for a 50 Å Ag film deposited on a 3 ML CeO_2 film. b) Ag $3d_{5/2}$ binding energy as a function of Ag nominal thickness, the Ag $3d_{5/2}$ binding energy of a 50 Å Ag film is also shown as a solid line.

The signals have been normalized in area to the bulk Ag value. Figure 7.2b reports the BE of the Ag $3d_{5/2}$ peak as a function of Ag nominal coverage for Ag deposited on CeO_2. At the lowest Ag coverages the Ag $3d_{5/2}$ BE is shifted to higher values compared to the bulk by up to 0.5 eV. The Ag $3d_{5/2}$ BE decreases with increasing Ag deposited amount reaching almost the bulk value above 4 Å. The observed shift can be ascribed to the reduced coordination of Ag atoms in the nanoparticles compared to the bulk, but a charge

transfer from Ag nanoparticles to the ceria substrate can also induce a shift in the binding energy value. Then, in this system certainly dimensionality related effects hinder the possibility of measuring eventual shifts due to charge transfer.

The evolution of Ce 3d XPS spectra has been considered in order to have additional information on possible charge transfer effects. Figure 7.3a shows the spectrum of a 3 ML ceria film measured before and after the growth of 0.2 Å of Ag.

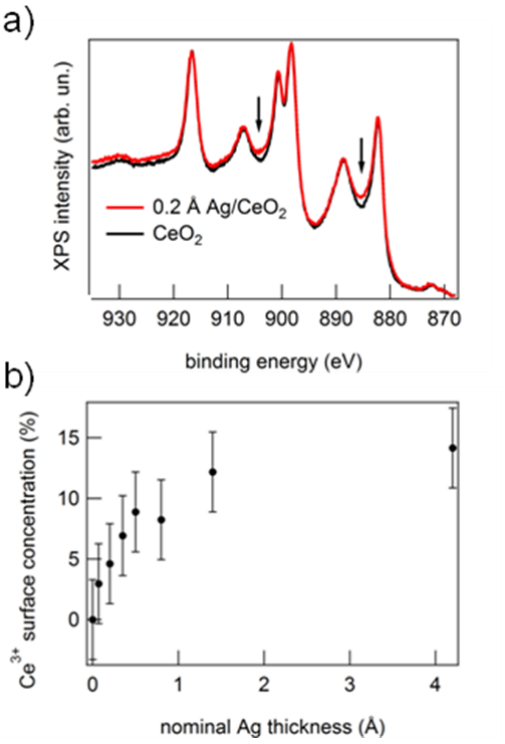

Figure 7.3: XPS spectra of a 3 ML CeO_2 film before (black curve) and after (red curve) the deposition of 0.2 Å Ag. The arrows indicate the regions in which Ce^{3+}-related peaks appear.

The change of the shape of the Ce 3d spectrum after Ag growth is consistent with the appearance of the most intense of Ce^{3+}-related doublet at 885 eV and it indicates that ceria is reduced by Ag growth. The observed ceria reduction can be due to an electron transfer from Ag or by other effects, such as O-reverse spillover or oxygen loss due to oxidation of carbonaceous species present in the background pressure. To have further information a fitting of the Ce 3d spectra after the deposition of different amounts of Ag was performed. As shown in Figure 7.3b the surface Ce^{3+} concentration increases as a function of the amount of deposited Ag up to 14% when all the ceria surface is covered by Ag. This behavior is qualitatively consistent with the hypothesis of a progressive charge transfer with increasing the fraction of CeO_2 surface in contact with Ag nanoparticles.

7.3.2 Theoretical results

7.3.2.1 Ag atoms on CeO_2(111) and CeO_{2-x}(111)

Deposition of Ag atoms on the CeO_2(111) surface can result in Ag species adsorbed on regular sites of the surface but, under special conditions, could also result in the substitution of Ce lattice ions. However, incorporation of Ag atoms in the ceria lattice requires very different preparation conditions than those used in the considered experiments. Here Ag vapor is deposited at room temperature on the CeO_2(111) thin films and it is likely that isolated atoms arrive on the surface.

In the interaction of an Ag atom with the regular surfaces of CeO_2(111) two stable adsorption sites have been identified theoretically: in one case, preferred (Figure 7.4), Ag is above an O atom of the third layer and is bound by 0.7 eV to three O atoms of the first atomic layer, in the other case Ag is directly on-top of an O

atom of the first atomic layer. Notice that the absolute value of the Ag adsorption energy should be taken with care since it can change significantly with the computational setup adopted.[8] In all sites Ag behaves as an electron donor with respect to CeO_2 with formation of an Ag^+ cation and a reduced Ce^{3+} ion:

$$Ag_1 + CeO_2 \rightarrow Ag_1^+/CeO_2^- (1\ Ce^{3+}) \qquad (7.1)$$

This is clearly shown by the value of the Bader charge on Ag, +0.54e, by the spin density maps which indicate that the 5s electron of Ag is no longer present while an unpaired electron is localized on the 4f states of one Ce ion (Figure 7.4a), and by the DOS plots which show the appearance of a singly occupied 4f state in the band gap of the material (Figure 7.4b). Thus, Ag atoms act as alkali metals and result in the formation of reduced Ce^{3+} ions.

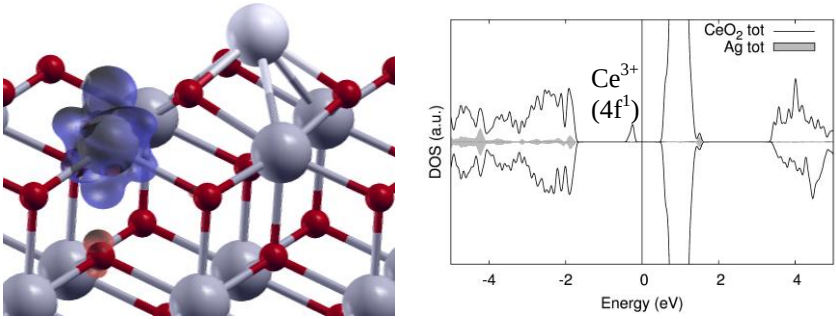

a **b**

Figure 7.4: Ag_1 deposited on the stoichiometric $CeO_2(111)$ surface. (a) Structure and spin distribution; (b) DOS curves.

Quite different is the interaction of Ag atoms with O vacancies. The removal of one oxygen atom corresponds to a reduction of the system and in fact two electrons are found in

localized 4f states on two surface $Ce^{+3}(4f^1)$ ions.[6,9,10,11,12,13,14] However, there is a distribution of Ce sites where the localization of the electrons can take place so that multiple structures exist with formally the same electronic configuration but with similar total energies.[15,16] An Ag atom binds rather strongly, by 1.4 eV, to an O vacancy at the $CeO_{2-x}(111)$ surface. The atom is directly on-top of an O atom of the third layer and in direct contact with three Ce atoms around the vacancy. Since two Ce^{3+} ions are associated to the vacancy and Ag has a $5s^1$ valence configuration, there is a maximum of three unpaired electrons. In the final structure, however, only one unpaired electron remains. This can be interpreted as due to an electron transfer from one Ce^{3+} ion to Ag_1 which formally becomes Ag^- ($5s^2$):

$$Ag_1 + CeO_{2-x}\,(2\,Ce^{3+}) \rightarrow Ag_1^-/CeO_{2-x}^{+}\,(1\,Ce^{3+}) \qquad (7.2)$$

The process can be seen also as due to the coupling of the Ce $4f^1$ with the Ag $5s^1$ electrons with formation of a covalent Ce-Ag bond. The Bader charge on Ag (-0.48 e) and the DOS curves which show the double occupancy of the Ag 5s level point more towards the first interpretation.

7.3.2.2 Ag clusters on $CeO_2(111)$ and $CeO_{2-x}(111)$

Gas-phase Ag_5 has a doublet ground state and when deposited to the $CeO_2(111)$ surface is bound by 1.96 eV (computed with respect to a bypiramidal trigonal gas-phase isomer). As for a single Ag atom, also for Ag_5 there is a net charge transfer towards the oxide. In the ground state (LDA+*U* and GGA+*U*=4), two electrons are transferred from Ag_5 to the oxide support, see Figure 7.5 (the Bader charge on Ag_5 is +0.84, the magnetic moments on two

Ce ions 0.87 and 0.76). In a second solution, 0.23 eV higher in energy, only one electron is transferred to a surface Ce ion which changes oxidation state from Ce^{4+} to Ce^{3+}. This second solution is nearly degenerate with the first one at the GGA+*U* (*U*=3 eV) level, indicating that while there is a clear tendency to transfer electrons from silver to ceria, the exact amount of charge transferred is method dependent. In general, the Ag atoms of the cluster at the boundary with ceria are slightly oxidized while the apical Ag atom (2^{nd} layer) keeps a metallic character.

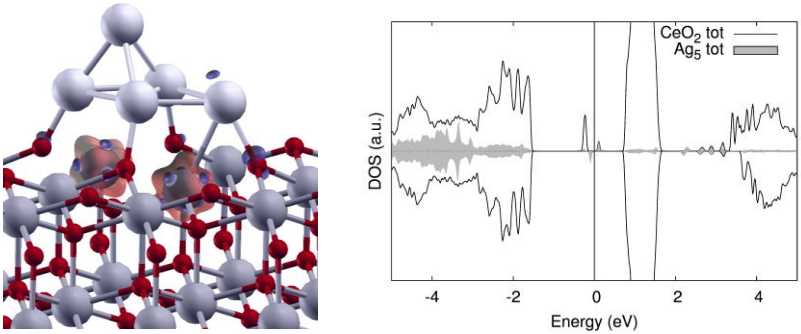

Figure 7.5: Ag_5 cluster deposited on the stoichiometric CeO_2(111) surface. (a) Structure and spin distribution; (b) DOS curves.

The oxidation of Ag_5 and the concomitant reduction of ceria could be biased by the presence of an unpaired electron on the cluster and by an easy ionization of this system. Furthermore, very small clusters have discrete energy levels whose energy depends on several factors like coordination number, shape of the cluster, etc. In other words, the occurrence of a charge transfer could be an artifact related to the special electronic structure of Ag_5. For this reason we have considered a larger Ag_{10} cluster with closed shell ground state. The cluster contains 7 Ag atoms in the first layer and 3 Ag atoms in the

second layer, Figure 7.6, and does not correspond to the most stable isomer of Ag_{10} while it is representative of a two-layer nanoparticle.

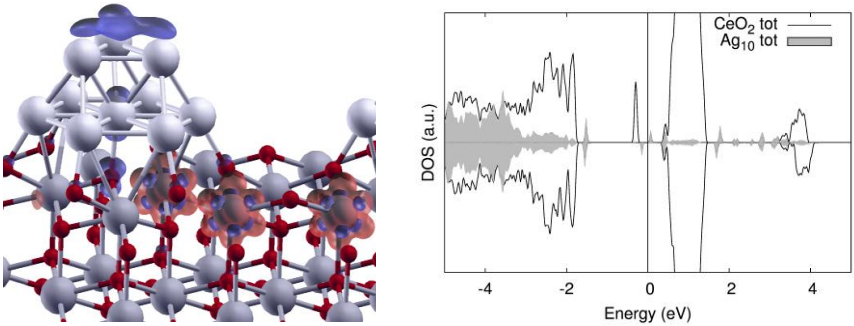

Figure 7.6: Ag_{10} cluster deposited on the stoichiometric $CeO_2(111)$ surface. (a) Structure and spin distribution; (b) DOS curves.

The Ag_{10} cluster has been adsorbed with the more extended face on $CeO_2(111)$ and the geometry has been fully reoptimized. The spin density analysis shows that after Ag_{10} deposition three Ce^{3+} are found on the ceria surface. Some spin density is also found on the top layer of the Ag cluster, Figure 7.6a. The formation of Ce^{3+} ions is confirmed by the DOS curves which show that the corresponding states are below the Fermi level, Figure 7.6b. So, not only the Ag_{10} cluster is oxidized by interaction with the ceria surface, but this involves more than a single electron (LDA+U and GGA+U=4 results). These results have been obtained with a 2ML thick CeO_2 support. We further checked that the charge transfer occurs also when the ceria support is modeled by a thicker 3ML slab but the LDA+U results confirm the occurrence of a multiple charge transfer. Also in this case, however, the extent and nature of the charge transfer changes when the GGA+U (U=3 eV) method is adopted: for

Ag_{10} on CeO_2(2ML) the charge transfer is still present, but the spin on the cerium oxide is delocalized over several Ce ions. In the following we discuss only LDA+U for geometry and properties and GGA+U (U=4 eV) results, keeping in mind that for smaller values of the U parameter the results may be partly different and probably physically less meaningful.

In summary, Ag atoms or Ag nanoclusters deposited on a stoichiometric CeO_2 surface are directly oxidized with reduction of the Ce ions of the support. However, the extent of the charge transfer and spin localization is a rather subtle question which depends on the level of accuracy of the theoretical treatment.

The next step has been to consider the same Ag_5 and Ag_{10} species adsorbed on an oxygen vacancy. When Ag_5 is adsorbed in the vicinity of an O vacancy on the CeO_{2-x}(111) surface the bonding is slightly larger than on the regular surface (E_{ad} = 2.21 eV versus 1.96 eV) and we found a total of three Ce^{3+} ions, Figure 7.7a.

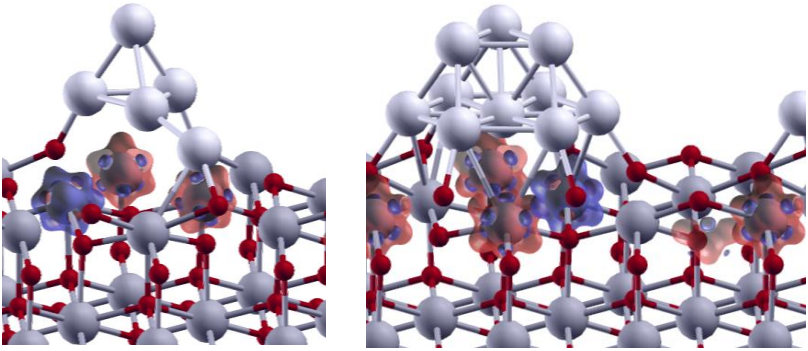

a **b**

Figure 7.7: (a) Ag_5 and (b) Ag_{10} clusters deposited on the reduced CeO_{2-x}(111) surface.

While two of these ions are related to the presence of the vacancy, the third one is due to an electron transfer from the Ag cluster. This is consistent with a positive Bader charge on the cluster (+0.4 e). Thus, even on a reduced surface there is a tendency of Ag_5 to be oxidized. This is further confirmed by the results obtained on Ag_{10} adsorbed on CeO_{2-x}(111), Figure 7.7b. Here we have a total of four Ce^{3+} ions, two of which are due to an electron transfer from the Ag cluster to the reduced ceria surface. A positive charge of +0.94e is present on the Ag cluster. Also in this case there is a moderate increase in adsorption energy going from Ag_{10} adsorbed on the regular surface, E_{ad} = 3.66 eV, to the same cluster adsorbed on reduced CeO_2, E_{ad} = 4.39 eV). This suggests that the mobility of Ag clusters should be smaller on the reduced ceria surface.

Then, on both stoichiometric and reduced ceria surfaces the Ag clusters act as electron donors and become oxidized at the expense of the ceria support. This process is spontaneous, and can involve more than one electron per cluster.

7.3.2.3 Extended Ag deposits (monolayer and bilayer)

So far we have considered the interaction between a finite system, Ag atoms or clusters, and the CeO_2(111) surface and we have observed that ceria is always reduced due to an electron transfer from the supported species. This effect could be related to the nanodimensionality of the adsorbate, and to the presence of orbitals at high energy which favor the electron transfer to the Ce 4f states. Large Ag nanoparticles, with diameter of a few nm, could behave quite differently due to the development of a metallic character (the work function in bulk Ag is 4.2 eV). For this reason we have considered a monolayer and a bilayer Ag film which has been adapted to the CeO_2(111) support. We have also considered two

different models of the CeO_2(111) surface, CeO_2(2ML) and CeO_2(3ML). The difference is that in the CeO_2(2ML) system all Ce atoms are surface atoms (either top or bottom atomic layers), while in CeO_2(3ML) the central layer is more "bulk-like". To simulate the Ag monolayer a 4 × 4 Ag(111) cell (16 Ag atoms) has been adapted to a 3 × 3 $Ce_{18}O_{36}$ supercell (CeO_2(2ML)); the two cells have nearly the same dimensions and the strain is about 1% (the Ag layer has been contracted to adapt to the ceria lattice constant).

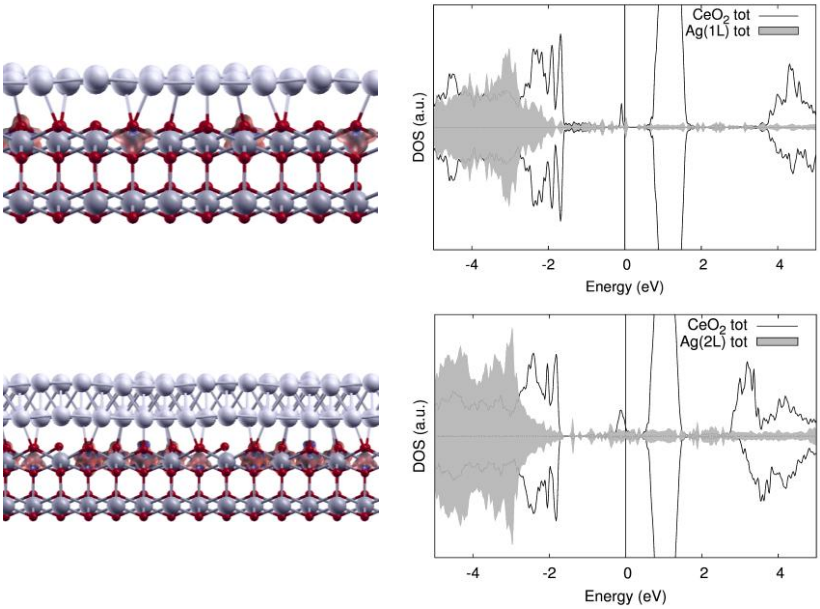

Figure 7.8: Structure and DOS of Ag films on CeO_2(111). Top: Ag(1ML)/CeO_2(111)(2ML); bottom: Ag(2ML)/CeO_2(111)(2ML)

When we consider 1ML Ag on CeO_2(2ML), Figure 7.8, we found clear evidence of a charge transfer. At both the LDA+U and GGA+U (U=4 eV) levels we found that one electron per unit cell is transferred from the Ag deposit to the oxide with formation of a

single Ce^{3+} ion. The Ag film has a non-negligible rumpling and the average distance between the top layer of Ce ions and the Ag film is of 2.44 Å. There is a partial spin polarization of the Ag layer (μ_{Ag} = 0.36) and an average charge on the Ag layer of +0.50e. Also for a 2ML Ag film grown on CeO_2(2ML), Figure 7.8, the tendency to reduce the oxide is confirmed: at both LDA+U and GGA+U (U=4 eV) levels we have clear evidence of four Ce^{4+} ions which are reduced to Ce^{3+}. The occurrence of a charge transfer is further confirmed by the Bader charges on the Ag layer at contact with CeO_2 which is +1.48e while the upper Ag layer is in zero oxidation state.

We further checked the results by using a 3ML CeO_2 support. For a single Ag layer the solution where no charge transfer occurs is preferred at all levels of treatment (LDA+U, GGA+U either with U = 3 or 4 eV). The charge transfer solution is about 0.3 eV higher in energy, but the spin on the ceria support is delocalized and not easy to quantify. When we consider 2ML of Ag on 3ML of CeO_2 we have indications of the occurrence of a multiple electron transfer. These results seem to indicate that, at variance with the Ag cluster models, for an extended Ag monolayer the tendency to reduce the ceria support is less pronounced and depends on the thickness of the ceria support used. As we mentioned before, the main difference between 2 and 3ML of ceria is that in the former case there is a large number of under-coordinated Ce ions. This suggests that the electron transfer from the Ag deposits is easier in the presence of low-coordinated sites, a situation which is common on small ceria nanoparticles or islands.

7.3.2.4 Oxygen spillover on silver

The DFT calculations indicate the reduction of the ceria support by deposition of Ag atoms and clusters via direct charge

transfer. While this fits with the experimental observations, the reduction of ceria by deposition of metal clusters could also be due to a reverse spillover of O atoms from the ceria surface to the metal cluster or nanoparticle, with formation of a reduced understoichiometric CeO_{2-x} support and of an oxygen covered Ag adsorbate. The process considered is thus:

$$Ag_n/CeO_2 \rightarrow Ag_nO/CeO_{2-x}\ (2\ Ce^{3+}) \qquad (7.3)$$

We first considered the small Ag_5 cluster. If the O atom is included inside the Ag_5 cage, in an interstitial position, the system is unstable and the O atom spontaneously moves towards the surface refilling the vacancy. On the contrary, if the O atom is bound to the top of the Ag_5 cluster we found a local minimum, Figure 7.9a, which is about 2.9 eV less stable than the reactants, i.e. $Ag_5/CeO_2(111)$.

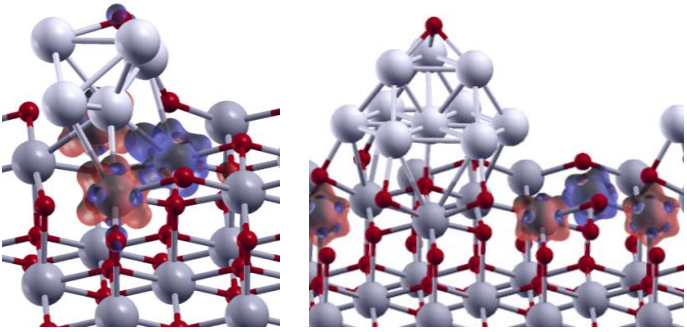

a **b**

Figure 7.9: Oxygen reverse spillover from the $CeO_2(111)$ regular surface to Ag_5 and Ag_{10} clusters. (a) Structure of Ag_5O/CeO_{2-x}; (b) Structure of $Ag_{10}O/CeO_{2-x}$.

The same process has been considered using the Ag_{10} supported cluster. In this case we did not consider an interstitial O

atom since the results for Ag_5 clearly show the preference for this species to diffuse to the vacancy and restore the original stoichiometry. Thus, the O atom has been moved from the Ag/CeO_2 interface to the top layer of the cluster where it is bound to Ag in a three-hollow position, Figure 7.9b. In this position the O atom is strongly bound to the supported Ag cluster, D_e = 3.01 eV, but this is far from compensating the cost of creating a vacancy and the entire system is 2.53 eV less stable than a Ag_{10} cluster adsorbed on a stoichiometric $CeO_2(111)$ surface.

These results indicate that the cost of moving one O atom from the ceria surface to the adsorbed Ag nanoparticle is much too high to consider the reverse spillover of oxygen as a plausible mechanism for ceria reduction.

7.4 Conclusions

The analysis of the XPS spectra of the deposited Ag nanoparticles on the thin ceria films grown on Pt(111) provides clear evidence for the reduction of the oxide by Ag deposition. This can be deduced from the lineshape of the Ce 3d states which show the characteristic change associated to the presence of Ce^{3+} ions for the deposition of Ag on stoichiometric $CeO_2(111)$ (Figure 7.3). This effect is accompanied by a positive shift of the Ag 3d core level binding energy by decreasing the size of the deposited nanoparticles. However, while there is no doubt about the fact that the ceria support is reduced upon silver deposition, the origin of this phenomenon is still under debate. In fact, core level binding energies of supported metal particles are affected by the size of the nanoparticles. In this respect, the simple analysis of the core level shifts of the metal nanoparticles can be misleading.[17] An attempt to disentangle the

initial and final state contributions to the Ag 3d core level shifts has been done using a delicate decomposition technique,[18,19,20] and it was concluded that the Ag nanoparticles on CeO_2(111) are metallic (zero oxidation state).

This conclusion contrasts with the results from our DFT calculations which show a clear tendency of the Ag nanoparticles to become oxidized by simple contact with the ceria surface. Of course, in the experiments and in literature[20] there is also clear evidence that the ceria support is reduced by Ag deposition. According to our DFT calculations this is the natural consequence of the charge transfer from Ag, while a different origin has to be invoqued if one assumes that the Ag particles remain in zero oxidation state. In order to rationalize the apparent reduction of ceria, in ref. 20 it has been suggested that spillover of lattice oxygen occurs at the Ag/CeO_2 boundary, and that oxygen diffuses on the surface of the Ag nanoparticles, thus leading to a CeO_{2-x}/Ag_nO_m system. This mechanism has been explicitly investigated in our DFT calculations, see reaction (7.3), and the results clearly show that oxygen reverse spillover from the CeO_2(111) surface to Ag is an energetically very unfavourable process. This is in line with the low affinity of Ag for O and with thermodynamic data. In fact, $\Delta H°(Ag_2O)$, −31.1 KJ/mol, is more than 30 times smaller than that of CeO_2 ($\Delta H°(CeO_2)$ = −1088.7 KJ/mol). This is also consistent with the relatively high cost to create an O vacancy on the CeO_2(111) surface, 3.54 eV if computed with respect to ½ O_2, 6.62 eV with respect to atomic O. This energy is hardly compensated by the formation of the bond between adsorbed O and the Ag particle.

A recent joint experimental-theoretical study on the oxygen reverse spillover on Pt clusters supported on ceria nanoparticles has shown that the process is greatly facilitated on small ceria crystallites because of the presence of low-coordinated O atoms and of a

substantial lowering of the formation energy of an O vacancy at these sites.[21] However, the experiments of ref. 20 as well as those reported here are dealing with large CeO_2(111) islands where the role of the border should be much less important than on ceria nanocrystals.

Finally, we notice that the observed increase of the concentration of Ce^{3+} ions with the amount of Ag deposited (Figure 7.3b) is a further support for the hypothesis of ceria reduction by electron transfer from Ag. The increase in Ce^{3+} concentration with the amount of Ag deposited is consistent with the observed increase of the ceria surface coverage. The O reverse spillover process, instead, is not expected to be more pronounced as the Ag particle size increases. Furthermore, the observed increase of Ce^{3+} concentration with annealing the Ag/CeO_2 system is comparable with the one of the bare CeO_2 surface, at variance with systems in which O reverse spillover was found to be dominant.[21] The energetical considerations coming from our theoretical calculations confirm the hypothesis that the reduction of ceria is not due to oxygen reverse spillover, but to charge transfer from silver.

The result of this chapter have been reported in the following publication:

Nature of Ag islands and nanoparticles on the CeO_2(111) surface. Luches P., Pagliuca F., Valeri S., Illas F., Preda G. Pacchioni G. *in press*

7.5 Bibliography

[1] M. Machida, Y. Murata, K. Kishikawa, D. Zhang, K. Ikeue, *Chem. Mater*. 20 (**2008**) 4489.
[2] C. Loschen, J. Carrasco, K. M. Neyman, F. Illas, *Phys. Rev. B* 75 (**2007)** 035115.
[3] Bader, R. F. W. *Atoms in Molecules*; Oxford University Press: Oxford, **1990**.
[4] G. Henkelman, A. Arnaldsson, H. Jónsson, Comput. *Mater. Sci*. 36 (**2006)** 254.
[5] W. Tang, E. Sanville, G. Henkelman, *J. Phys.: Condens. Matter* 21 (**2009)** 084204.
[6] C. Loschen, A. Migani, S. T. Bromley, F. Illas, K. M. Neyman, *Phys. Chem. Chem. Phys.* 10 (**2008)** 5730.
[7] P. Luches, F. Pagliuca, S. Valeri, *J. Phys. Chem C* 115 (**2011)** 10718.
[8] M. M. Branda, N. C. Hernandez, J. F. Sanz, F. Illas, *J. Phys. Chem. C* 114 (**2010)** 1934.
[9] N. V. Skorodumova, S. I. Simak, B. I. Lundqvist, I. A. Abrikosov, B. Johansson, *Phys. Rev. Lett*. 16 (**2002)** 166601.
[10] M. Nolan, S. Grigoleit, D. C. Sayle, S. C. Parker, G. W. Watson, *Surf. Sci*. 576 (**2005)** 217.
[11] P. J. Hay, R. L. Martin, J. Uddin, G. E. Scuseria, *J. Chem. Phys.* 125 (**2006)** 034712.
[12] D. Mei, N. Aaron Deskins, M. Dupuis, Q. Ge, *J. Phys. Chem. C* 111 (**2007)** 10514.
[13] M. M. Branda, C. Loschen, K. M. Neyman, F. Illas, *J. Phys. Chem. C* 112 (**2008)** 17643.
[14] M. B. Watkins, A. S. Foster, A. L. Shluger, *J. Phys. Chem. C* 111 (**2009)** 15337.
[15] M. V. Ganduglia-Pirovano, J. L. F. Da Silva, J. Sauer, *Phys. Rev. Lett*. 102 (**2009)** 026101.
[16] H.-Y. Li, H.-F. Wang, X.-Q. Gong, Y.-L. Guo, G. Lu, P. Hu, *Phys. Rev. B* 79 (**2009)** 193401.
[17] P. S. Bagus, F. Illas, G. Pacchioni, F. Parmigiani, *J. Elect. Spectr. Rel. Phenom*. 100 (**1999)** 215.
[18] C. D. Wagner, *Anal. Chem*. 44 (**1972)** 967.
[19] C. D. Wagner, L. H. Gale, R. H. Raymond, *Anal. Chem*. 51 (**1979)** 466.
[20] D. Kong, G. Wang, Y. Pan, S. Hu, J. Hou, H. Pan, C. T. Campbell, J. Zhu, *J. Phys. Chem. C* 115 (**2011)** 6715.

[21] G. N. Vayssilov, Y. Lykhach, A. Migani, T. Staudt, G. P. Petrova, N. Tsud, T. Skala, A. Bruix, F. Illas, K. C. Prince, V. Matolin, K. M. Neyman, J. Libuda, *Nature Materials* 10 (**2011)** 310.

Chapter 8

Conclusions

In this Ph.D. thesis the reactivity of clean and silver precovered ceria surfaces has been studied in the context of applications in catalysis of Diesel particulate soot abatement. In fact, ceria and in particular silver doped ceria show very good catalytic activity in decreasing the temperature of soot combustion. A key step in the mechanism of oxidation of the particulate, which is mainly amorphous carbon, is the activation of the oxygen molecule. In literature, experimental IR-Raman and EPR studies show the comparison of peroxo, O_2^{2-}, and superoxo, O_2^-, species when O_2 interacts with ceria.

With theoretical calculations we firstly investigated the interaction of O_2 with regular $CeO_2(111)$ and defective CeO_{2-x} (111) surfaces. While with the regular surface we found no interaction and no activation of the oxygen molecule, on the oxygen vacancy a peroxo strongly linked to the surface is observed. The formation of O_2^{2-} is due to a charge transfer from the two Ce^{3+} centers that are located on the surface when an O is removed. The formation of a superoxo, thus, is not found when such an interaction is considered. The hypothesis is then that the interaction of O_2 with isolated Ce^{3+} could generate O_2^- by charge transfer.

When O_2^- is studied, Electron Paramagnetic Resonance (EPR) properties can be evaluated. For superoxo formed on ceria the experimental spectra available in literature are not well resolved, so a comparison between calculated and experimental data is not trivial.

Then, a model system has been studied to validate the theoretical approach in reproducing EPR properties of superoxo. In fact, for O_2^- formed on Na precovered MgO surfaces, very well resolved EPR spectra are available. In this case we found that our theoretical approach can reproduce the EPR properties very well.

Subsequently, we studied the interaction of O_2 with ceria clusters and nanoparticles. At first, we considered the model system Ce_2O_3, that has two Ce^{3+} ions. This species has been modeled at different theoretical levels, and we always found the expected result, the formation of O_2^- by charge transfer from one low-coordinated Ce^{3+} center. The evidences of this are in the O-O bond length, in the IR frequency and in the EPR properties, that are in very good agreement with the experimental ones. This result has been confirmed also on bigger defective nanoparticles, where the oxygen vacancy leaves two Ce^{3+} centers that stabilize on low-coordinated sites. The presence of low-coordinated and, more important, isolated Ce^{3+} centers is thus responsible of the formation of superoxo ions on ceria.

The role of silver in improving the catalytic activity of ceria is proved in literature by a decrease of the soot combustion temperature. Moreover, in literature, experimental EPR studies show a slightly increase of the signal due to the presence of superoxo ions. Experimental STM and XPS data of Ag nanoparticles deposited on stoichiometric and reduced thin CeO_2 films grown on Pt(111) in UHV conditions show a reduction of ceria with comparison of Ce^{3+} centers. Theoretically, we studied the interaction of Ag atoms, Ag_5 and Ag_{10} clusters and mono and bi-layers of silver adsorbed on CeO_2(111) and CeO_{2-x}(111) surfaces. We found a general tendency of silver to reduce ceria by charge transfer, with subsequent oxidation of the metal. However, the experimental data could also fit

with an oxygen spillover mechanism. In this situation, oxygen atoms migrate from the surface to the metal particles, leaving a reduced support. Our calculations show that this mechanism is highly unfavourable from an energetic point of view. Therefore, both the experimental and the theoretical results agrees with a reduction of ceria due to a charge transfer from silver.

Publications

- "The reactivity of CO_2 with K atoms adsorbed on MgO powders."
  Preda G., Pacchioni G., Chiesa M. et al., *Phys. Chem. Chem. Phys*., 11 (**2009**) 8156.

- "Formation of superoxo species by interaction of O_2^- with Na atoms deposited on MgO powders: a combined continuous-wave EPR (CW-EPR), hyperfine sublevel correlation (HYSCORE) and DFT study."
  Napoli F., Chiesa M., Giamello E., Preda G., Di Valentin C., Pacchioni G., *Chemistry-A European Journal*, 16 (**2010**) 6776.

- "Formation of superoxide anions on ceria nanoparticles by interaction of molecular oxygen with Ce^{3+} sites."
  Preda G., Migani A., Neyman K. M., Bromley S. T., Illas F., Pacchioni G., *Journal of Physical Chemistry C*, 115 (**2011**) 5817.

- "Initial formation of positively charged gold on MgO(001) thin films: identification by experiment and structural assignment by theory."
  Brown M. A., Ringleb F., Fujimori Y., Sterrer M., Freund H.-J., Preda G., Pacchioni G., *Journal of Physical Chemistry C*, 115 (**2011**) 10114.

- "Formation of oxygen active species in Ag-modified CeO_2 catalyst for soot oxidation: A DFT study."
  Preda G., Pacchioni G., *Catalysis Today*, 177 (**2011**) 31.

- "Nature of Ag islands and nanoparticles on the CeO_2 (111) surface."
  Luches P., Pagliuca F., Valeri S., Illas F., Preda G. Pacchioni G., *in press*

Acknowledgements

- My family
- My research group, in particular Prof. Pacchioni
- Pirelli and CORIMAV: fellowship
- Fondazione Cariplo: fundings
- Prof. Francesc Illas (Universitat de Barcelona): period abroad at the Universitat de Barcelona, works in collaborations
- Dott. Annapaola Migani (Universidad del País Vasco): calculations on ceria nanoparticles
- Dott. Paola Luches, Prof. Sergio Valeri (Università di Modena e Reggio Emilia): STM and XPS experiments on ceria
- Prof. Mario Chiesa, Prof. Elio Giamello: EPR experiments on magnesiun oxide